LBNL-38980
UC-404

Ernest Orlando Lawrence Berkeley National Laboratory

Heat Capacity of Quantum Adsorbates: Hydrogen and Helium on Evaporated Gold Film

J.T. Birmingham
Materials Sciences Division

June 1996
Ph.D. Thesis

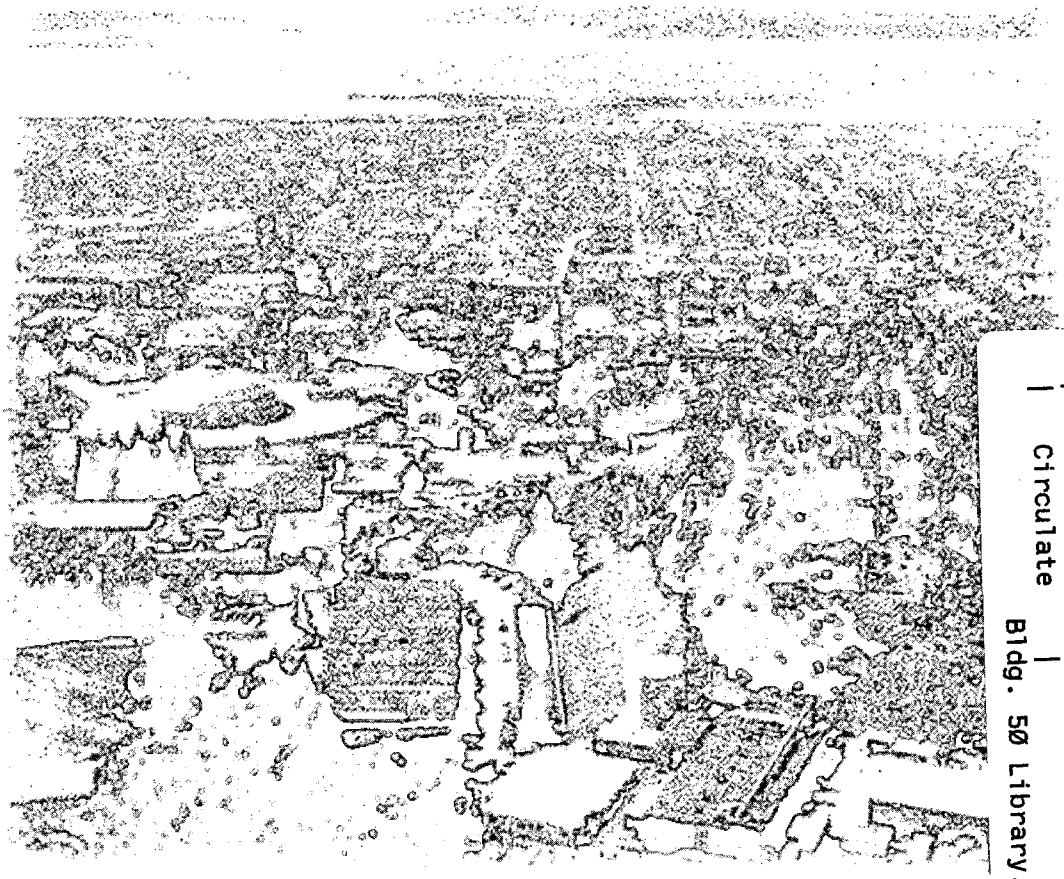

REFERENCE COPY
Does Not
Circulate
Bldg. 50 Library.
Copy 1
LBNL-38980

DISCLAIMER

This document was prepared as an account of work sponsored by the United States Government. While this document is believed to contain correct information, neither the United States Government nor any agency thereof, nor the Regents of the University of California, nor any of their employees, makes any warranty, express or implied, or assumes any legal responsibility for the accuracy, completeness, or usefulness of any information, apparatus, product, or process disclosed, or represents that its use would not infringe privately owned rights. Reference herein to any specific commercial product, process, or service by its trade name, trademark, manufacturer, or otherwise, does not necessarily constitute or imply its endorsement, recommendation, or favoring by the United States Government or any agency thereof, or the Regents of the University of California. The views and opinions of authors expressed herein do not necessarily state or reflect those of the United States Government or any agency thereof or the Regents of the University of California.

LBNL-38980
UC-404

Heat Capacity of Quantum Adsorbates: Hydrogen and Helium on Evaporated Gold Films

John Thomas Birmingham
Ph.D. Thesis

Department of Physics
University of California, Berkeley

and

Materials Sciences Division
Ernest Orlando Lawrence Berkeley National Laboratory
University of California
Berkeley, CA 94720

June 1996

This work was supported by the Director, Office of Energy Research, Office of Basic Energy Sciences, Materials Sciences Division, of the U.S. Department of Energy under Contract No. DE-AC03-76SF00098.

LBNL-38980

Heat Capacity of Quantum Adsorbates: Hydrogen and Helium on Evaporated Gold Films

by

John Thomas Birmingham

A.B. (Princeton University) 1989
M.A. (University of California at Berkeley) 1991

A dissertation submitted in partial satisfaction of the

requirements for the degree of

Doctor of Philosopy

in

Physics

in the

GRADUATE DIVISION

of the

UNIVERSITY of CALIFORNIA at BERKELEY

June 1996

Committee in charge:

Professor P. L. Richards, Chair
Professor D. Rokhsar
Professor G. Somorjai

Heat Capacity of Quantum Adsorbates: Hydrogen and Helium on Evaporated Gold Films

Copyright © 1996

by

John Thomas Birmingham

The U.S. Department of Energy has the right to use this document
for any purpose whatsoever including the right to reproduce
all or any part thereof

Abstract

Heat Capacity of Quantum Adsorbates:
Hydrogen and Helium Adsorbed on Evaporated Gold Films

by

John Thomas Birmingham

Doctor of Philosopy in Physics

University of California at Berkeley

Prof. Paul L. Richards, Chair

We have constructed an apparatus to make specific heat measurements of quantum gases adsorbed on metallic films at temperatures between 0.3 and 4 K. The detector is constructed from a commercial quartz single crystal which is simultaneously operated as an AC calorimeter and a microbalance, so that the heat capacity and coverage of the adsorbate can be directly measured. The system has been designed to minimize the possibility of contamination of either the metallic film or the adsorbate.

We have used this apparatus to study quench-condensed hydrogen films between 4 and 923 layers thick with J=1 concentrations between 0.28 and 0.75 deposited on an evaporated gold surface. We have observed that the orientational ordering of the J=1 molecules depends on the substrate temperature during deposition of the hydrogen film. The ordering peak becomes less prominent when the film becomes thinner than the equivalent of twenty layers. Unlike in the bulk there is no hysteresis in the ordering transition. We have inferred that the density of the films condensed at the lowest temperatures is 25% higher than in bulk H_2 crystals and have observed that the structure of those films is affected by annealing at 3.4 K.

We have measured the J=1 to J=0 conversion rate to be comparable to that of the bulk for thick films; however, we found evidence that the gold surface catalyzes conversion in the first two to four layers. We have measured desorption rates and deduced a sublimation energy for quench-condensed H_2.

We have also used this apparatus to study films of ^{4}He less than one layer thick adsorbed on an evaporated gold surface. We show that the phase diagram of the system is similar to that for ^{4}He/graphite although not as rich in structure, and the phase boundaries occur at different coverages and temperatures. At coverages below about half a layer and at sufficiently high temperatures, the ^{4}He behaves like a two-dimensional noninteracting Bose gas. At lower temperatures and higher coverages, we have observed liquidlike and solidlike behavior.

In the Appendix we show measurements of the far-infrared absorptivity of the high-T_c superconductor $La_{1.87}Sr_{0.13}CuO_4$. When the radiation was polarized parallel to the c-axis, we observed an absorptivity onset at 41 cm^{-1} which is identified as a plasma edge. This is 1-2 cm^{-1} higher than the frequency measured with reflectance at 10 K on the same sample, indicating that more carriers participate in the superconducting condensate at the lower temperature. Below the plasma edge, the absorptivity falls as frequency squared. We have measured the superconducting plasma frequency to be 235 ± 15 cm^{-1} and have derived the complex dielectric function $\tilde{\varepsilon}(\omega)$ and conductivity $\tilde{\sigma}(\omega)$ from a Kramers-Kronig transformation of the data.

Dedicated to my parents

Table of Contents

List of Figures vi

List of Tables viii

Preface ix

1. Introduction 1
   1.1 The Importance of the Substrate 3
   1.2 Physisorption 3
   1.3 Previous Heat Capacity Studies--Mainly Graphite Substrates 4
   1.4 Metal Substrates 6
   1.5 Motivation for Experiments 8
   References 9

2. Apparatus and Experimental Procedures 11
   2.1 Introduction 11
   2.2 Calorimeter/Microbalance 12
      2.2.1 Calorimeter Construction and Operation 12
      2.2.2 Calorimetry Electronics 18
      2.2.3 Microweighing 22
   2.3 Cryogenic System 29
   2.4 Evaporation of the Gold Film 31
   2.5 Condensation of the Adsorbate 33
      2.5.1 External Room Temperature UHV Plumbing 33
      2.5.2 Cooled Effusion Line and Cell 35
   References 37

3. Heat Capacity of Quench-Condensed Hydrogen Films 39
   3.1 Introduction 39
      3.1.1 Ordering in Solid Hydrogen 39
      3.1.2 Ortho-Para Conversion 40
      3.1.3 Quench-Condensed Hydrogen 41
      3.1.4 Our Experiment 42
   3.2 Experimental Procedures 43
      3.2.1 Calorimeter/Microbalance 43
      3.2.2 Comment on AC Technique 43
      3.2.3 Preparation of the H_2 Film 44
   3.3 Results for Thick Films 45
      3.3.1 The Specific Heat C(T) 45
      3.3.2 Effect of Annealing on C(T) of T_{cond}=1.5 K Film 51
      3.3.3 J=1 to J=0 Conversion Rate 55
      3.3.4 Dependence of Thermal Properties and T_c on X 56

3.3.5 Thermal Hysteresis 63
3.4 Model and Discussion 66
3.5 Results for Thinner Films 67
3.5.1 Experimental Complication--Stress Sensitivity 68
3.5.2 Results 71
3.5.3 Discussion 74
3.6 Summary 77
References 80

4. Heat Capacity of Helium Monolayers Adsorbed on Evaporated Gold . 83
4.1 Introduction 83
4.1.1 ^{4}He/Graphite and ^{3}He/Graphite 83
4.1.2 ^{4}He/Evaporated Silver 86
4.1.3 2D Noninteracting Bose Gas 87
4.2 Experimental Procedures 91
4.2.1 Calorimeter/Microbalance 91
4.2.2 Preparation of the Substrate and Helium Film 91
4.3 Heat Capacity Measurements of ^{4}He Monolayers 92
4.3.1 Films Condensed at 3.0 K 92
4.3.2 Films Condensed at 2.4 K 100
4.3.3 C(T) of Films with T_{cond} = 2.4 K 102
4.4 Discussion 113
4.5 Summary 116
References 118

Appendix: Measurement of Optical Absorptivity of $La_{1.87}Sr_{0.13}CuO_4$ Below the Superconducting Plasma Edge 120
A.1 Introduction 120
A.2 Experimental Technique 122
A.3 Absorptivity Measurements 125
A.4 Kramers-Kronig Analysis 131
A.5 Discussion 135
A.6 Summary 143
References 145

List of Figures

2.1 Calorimeter/Microbalance 13
2.2 Thermistor calibrations 15
2.3 Thermal circuit of calorimeter 16
2.4 Calorimetry electronics 19
2.5 Measurement of calorimeter frequency response 20
2.6 Equivalent circuit of quartz substrate 24
2.7 Shear mode oscillation of quartz 26
2.8 Microbalance electronics 28
2.9 Cryogenic apparatus 30
2.10 Room temperature gas handling system 34

3.1 C(T) for H_2 quench-condensed at several temperatures 46
3.2 Reduced entropy s(T) for several condensation temperatures 50
3.3 Effect of annealing on C(T) 53
3.4 Ortho-para conversion experiment 57
3.5 Time evolution of C(T) 58
3.6 Scans 9, 10, 11 of Figure 3.5 61
3.7 Reduced entropy of scans 9, 10, 11 62
3.8 T_c vs. X 64
3.9 Hysteresis experiment 65
3.10 Microbalance stress effect 70
3.11 Coverage dependence of C(T) 72
3.12 C(T) for two large coverages 73

4.1 Proposed phase diagram for ^{4}He/graphite 84
4.2 C(T) for ^{4}He/evaporated silver 88
4.3 C(T) for ^{4}He/SiO 93
4.4 Adsorption of ^{4}He on evaporated gold at 3.0 K 94
4.5 Desorption of ^{4}He from evaporated gold at 3.0 K 97
4.6 Heat capacity vs. coverage at 3.0 K 99
4.7 Heat capacity vs. coverage at 2.4 K 101
4.8 C(T) for six ^{4}He coverages 103
4.9 Comparison of C(T) with 2D Bose gas calculation 105
4.10 C(T) vs. T^2 106
4.11 Model density of states for ^{4}He/disordered surface 108
4.12 C(T) fit to Equation 4.8 110
4.13 C(T) fit to Equation 4.9 112
4.14 Phase diagram for ^{4}He/evaporated gold 114

A.1 Apparatus for absorptivity measurement 123
A.2 c-axis absorptivity of $La_{1.87}Sr_{0.13}CuO_4$ between 100 and 520 cm^{-1} 126
A.3 c-axis absorptivity between 6 and 130 cm^{-1} 127

A.4 c-axis absorptivity below 40 cm^{-1} 129
A.5 Comparison of a-axis and c-axis absorptivity 130
A.6 Ratio of a-axis to c-axis absorptivity 132
A.7 Measured and calculated $\varepsilon_1(\omega)$ 136
A.8 Measured and calculated $\sigma_1(\omega)$ 137
A.9 Measurements of superconducting plasma frequency 139
A.10 Evidence of gap symmetry in $\sigma_1(\omega)$ 141

List of Tables

3.1 Thin Film Conversion Data 75
3.2 Coverage Dependence of Ordering Peak 76

4.1 Fit Coefficients for Equation 4.8 109
4.2 Fit Coefficients for Equation 4.9 111

A.1 Drude-Lorentz Fitting Parameters 142

Preface

Several physical systems will be discussed in this thesis. The physics and phenomena observed are very different in each of the experiments described: heat capacity measurements of quench-condensed hydrogen films, heat capacity measurements of helium monolayers adsorbed on gold, and measurements of the optical properties of the high temperature superconductor $La_{1.87}Sr_{0.13}CuO_4$. The link between these projects is the detector technique, which is only slightly modified for each of these experiments.

When I began research in the Richards group, I was intrigued by the heat capacity measurements of ^{4}He monolayers on evaporated films made by Tom Kenny, who had only recently graduated. Tom had obtained some exciting results suggesting that a layer of ^{4}He adsorbed on gold behaved like a noninteracting two-dimensional (2D) Bose gas. The measurements were made in a conventional UHV chamber with a liquid helium (LHe) cooled cold finger. Although the minimum pumped LHe bath temperature was 1.3 K, measurements were limited to temperatures above 1.6 K because of radiative heating of the calorimeter. To test the Bose gas model at lower temperatures, I set out to build an apparatus to extend the measurements down to 0.3 K. I sent a design for a ^{3}He sorption refrigerator down to the machine shop for fabrication, charged the refrigerator, and began testing calorimeters at 0.3 K in an Infrared Labs dewar. Concurrently, Bob Phelps was measuring the heat capacity of thin quench-condensed H_2 films in the same apparatus Tom used and studying how a bulk phase transition depended on the film thickness. I assisted Bob in these measurements and

became more involved in the project when the manuscript was submitted for publication. I remember being slightly amused by Bob's assertion in the paper that future efforts would extend the investigation to lower temperatures. At that point it seemed to me that Bob had done an exhaustive investigation and that there was nothing more to be learned about quench-condensed hydrogen films.

When I began trying to condense helium films on my calorimeter, I realized that our design had a flaw. Opening the shutter to allow the gas into the dewar exposed the detector to so much 300 K radiation that the detector heated to a temperature high enough that weakly-binding helium would not stick. We decided to build an entirely new apparatus to correct this problem and address some of the shortcomings of the earlier system. The design of the new apparatus and a discussion of the techniques used in the heat capacity measurements are covered in Chapter 2 of this thesis.

I obtained the first helium data just in time for the March meeting in 1994. At that meeting people were very excited about the wetting properties of helium on various weak-binding substrates. There were questions about how helium would behave on a hydrogen substrate, so not long after, I condensed a thick film of hydrogen on my calorimeter and then sprayed some helium on to top. I soon realized that I didn't understand the behavior of the hydrogen very well, and that "future efforts" were indeed appropriate. We began a very fruitful and enjoyable collaboration with Prof. Horst Meyer at Duke and obtained some interesting results which extended Bob's measurements and impacted the recent discussion of surface diffusion in hydrogen films. The hydrogen work is discussed in Chapter 3.

In the fall of 1994 I was given the opportunity to learn about far-infrared spectroscopy, which is a strength of the Richards group. I thought it would be a shame to graduate without learning about this topic, and so I became involved in a number of collaborations investigating the optical properties of novel materials. Working closely with Sabrina Grannan, I have studied polymerized and doped fullerenes in collaboration with groups at Berkeley and IBM and the high-temperature superconductor $La_{1.87}Sr_{0.13}CuO_4$ in collaboration with researchers from the Max Planck Institute in Stuttgart. This last experiment is discussed in the Appendix.

The detector used in these infrared experiments is very similar in both construction and purpose to my calorimeter, and the experience gained during this foray into spectroscopy assisted me when I finally returned to the question I initially intended to answer. Heat capacity measurements of ^4He monolayers adsorbed on evaporated gold films are discussed in Chapter 4.

Acknowledgments

Many people have assisted me in reaching this point, and I am truly grateful to each of them.

First and foremost, I would like to thank my advisor, Prof. Paul L. Richards, for the privilege of learning under his supervision. His integrity and dedication to science and his students will continue to inspire me both inside and outside the laboratory.

I have had the good fortune to work with a remarkable group of labmates, for whom I have much affection. Bob Phelps was an excellent mentor, and I must constantly thank him for insisting I write everything in my lab notebook. I learned a great deal of physics just from quietly listening to the conversations of Carl Mears and Simon Verghese. Michael Nahum taught me a few simple rules for living, and they are good ones. David Miller has been a generous friend, and I particularly want to thank him for introducing me to spectroscopy. I very much enjoyed reading plays and discussing politics and philosophy with Andre Clapp. I could always count on Warren Holmes for a kind word, a bad pun, and an intriguing idea for a new experiment. I also want to thank Warren for reading part of this thesis. Stacy Tanaka has known me longer than anyone else in the group, and yet she will still go with me for coffee twice a day. Thanks to Marc Fischer, Jamie Bock, Thor Wilbanks, Jason Feldman and the other starwatchers for helpful answers to ill-formed questions.

It would be hard to think of a better collaborator than my labmate Sabrina Grannan. Our spectroscopy experiments reinvigorated my graduate career, and I only regret that we didn't begin working together earlier. Jens Kircher was another collaborator who was great fun in any setting. My

collaboration with Horst Meyer on the hydrogen work was one of the high points of graduate school, and I am most appreciative of his encouragement and enthusiasm. I also want to thank Don Bethune, Alex Zettl, and Jim Hone for the opportunity to work with them. Bertha Zambrano patiently answered the same administrative questions year after year. None of these experiments would have possible without the efforts of George Weber, Andy Brocato, and Marco Ambrosini, who built my apparatus.

I didn't spend every hour at the lab, although sometimes it seemed like I did. The companionship and support of good friends enriched my life tremendously. Thanks in particular to Oscar Dubon, Ryan Johnson, Anne Takizawa, Kanwal Singh, and Azlina Azhar. Shin Mee Chang has been my best friend and so much more during the whole stretch, and she motivated me to finally move on to a new stage of my life.

None of this could have been possible without the love and nurturing of my family. I want to thank my brothers Jim and Mark for their faith in me and for helping me keep my sense of humor through even the toughest times. Most of all I want to thank my parents for putting me in the position both to have and to appreciate this experience.

1. Introduction

Studies of molecules physisorbed to weak-binding surfaces provide us with insight into the nature of critical behavior in low-dimensional systems, as well as practical information relevant to adhesion and lubrication. The heat capacity is one of the most useful and easily visualized probes of physisorbed systems because of its close relationship to the entropy. Peaks in the heat capacity can signify the crossing of phase boundaries. In the regions between peaks, the temperature dependence of the heat capacity can be used to identify the phase.

Ordering behavior in two dimensions is inherently different than in three dimensions, with some interesting consequences. Fluctuations prohibit genuine long-range order in two dimensions at non-zero temperatures in a system where the order parameter has a continuously varying phase.[1] However, such a two-dimensional (2D) system can enter a phase of topological,[2] if not truly infinite, long-range order. Examples include the superfluid transition in thin ^{4}He films[3] and the continuous melting of monolayers of noble gases adsorbed to graphite,[4] which has been described within the framework of the theories of Kosterlitz, Thouless, Halperin, Nelson, and Young,[2,5,6] Unlike in bulk three-dimensional systems, defects are thought to play a very important role in two-dimensional phase transitions, and so the structure, quality, and cleanliness of a substrate could have a large effect on the adsorbate behavior. Some of these issues are addressed in the study of ^{4}He monolayers and submonolayers adsorbed on evaporated gold films presented in Chapter 4.

In films that can be grown from monolayer to multilayer thickness, the transition from two-dimensional to three-dimensional ordering can be investigated. In solid multilayers, for instance, one would expect to see a crossover from a two-dimensional T^2 Debye contribution to the heat capacity to a three-dimensional T^3 contribution when the film becomes thicker than the wavelength of the dominant phonon mode, which is of order $V_s h/k_B T$, where V_s is the average velocity of sound. In physisorption systems at low temperatures, however, uniform, or Frank-van der Merwe growth, only occurs in a few cases. If the substrate-adsorbate interaction is very weak compared to the cohesive energy of the bulk adsorbate, growth of the bulk phase will be favored over uniform growth, and if the substrate-adsorbate interaction is very strong, the first few adsorbed layers will be compressed, causing a lattice mismatch which will again favor bulk growth at higher coverages. On a weak-binding surface like gold, bulk-like, or Stranski-Krastnov, growth is observed in multilayers beyond a certain thickness below some wetting temperature T_w.[7] A film ten or so layers thick could have a large surface-to-volume ratio and a range of coordination numbers. Hence one might see a very complicated ordering behavior, different from both the ideal two- and three-dimensional predictions. Even in very thick films, the substrate can play a role in the adsorbate critical behavior, since disorder, vacancies, grain boundaries, and free surfaces can result from the adsorbate-substrate interaction and the dynamics of the film preparation. The work on thicker quench-condensed H_2 films in Chapter 3 addresses some of these issues.

Each of the chapters that follow is relatively self-contained. Background information and previous experiments will be described in

each. In the remainder of this chapter we will discuss the general importance of the substrate in physisorption experiments. We give a brief physical description of the physisorption potential and review previous heat capacity measurements of physisorbed noble gases. We focus on graphite, which has been chosen for many experiments because of its smooth physisorption potential. Detailed discussions of physisorbed H_2 and ^4He will be delayed until Chapters 3 and 4, respectively. Finally we will discuss the advantages of metal substrates and our choice of an evaporated gold substrate.

1.1 The Importance of the Substrate

Since we are more interested in learning about the intrinsic properties of two-dimensional ^4He films and disordered H_2 than about adsorbate-substrate interactions, we would like to ignore the substrate altogether. Hence, we would like a substrate which simply holds the adatom to the surface, but doesn't impede motion in the plane of the substrate. Real surfaces of course are not ideal, and the magnitude and corrugation of the substrate-adsorbate potential must be considered. Whether a surface acts "ideal" will depend on the temperature and density of the adsorbate, the energies which characterize the adsorbate-adsorbate interaction, and the depth and corrugation of the physisorption potential.

1.2 Physisorption

Physisorption refers to the very weak binding of a noble gas atom or saturated molecule like H_2 to a surface. The well depth can vary from 0.043 meV for a ^3He atom adsorbed to a ^4He surface to about 160 meV for

Xe/graphite.[8] The simplest model for the physisorption potential assumes that it depends only on the distance z from the absorbate surface and neglects the variation in the lateral direction due to the fixed substrate ions:

$$V(z) = A\, e^{-Kz} - C_3\, z^{-3} \quad . \tag{1.1}$$

The first term is repulsive and results from the overlap of the charges of the adsorbate and substrate, which forces their rearrangement and increases the kinetic energy compared to infinite separation. The parameter K is essentially the decay length for the surface charge density. The second term can be interpreted as the attraction between an atomic dipolar fluctuation in the adatom and its image dipole. The gas-surface dispersion coefficient C_3 is closely related to the polarizability of the adatom.[9] The shape of the physisorption well can be determined from scattering experiments which probe the bound state resonances,[10,11] and from measurements of the isoteric heat[12] and the desorption rate.[13]

1.3 Previous Heat Capacity Studies--Mainly Graphite Substrates

The most common substrate for physisorption studies of monolayers has been graphite, which has achieved great popularity because of its outstanding homogeneity[14] and large surface area, consisting mostly of basal plane surfaces. It was originally calculated[15] that the high density of carbon atoms in the basal plane would result in only slight corrugation in the binding energy. This seemed to be borne out by the first of observation of an ideal classical two-dimensional gas, with heat capacity k_B/atom, in the ^{4}He/graphite system. The existence of this phase was attributed to the

homogeneity of the physisorption potential.[16] Even with ^{4}He, however, the corrugation of the graphite substrate has a very important role in the adsorbate behavior at temperatures below 2.5 K and coverages above 1/3 of a layer, as evidenced by the existence of regions in the phase diagram where the adsorbate forms a solid commensurate with the underlying hexagonal lattice.[17] At other submonolayer coverages the adsorbate forms a liquid or an incommensurate solid.[17] This system and ^{3}He/graphite will be discussed in further detail in Chapter 4. Heat capacity measurements have shown para-H_2/graphite to have a phase diagram similar to that of ^{4}He/graphite but with the boundaries between the various phases shifted to 4× higher temperatures because of the stronger adsorbate-adsorbate interactions.[18] Investigations of other noble gases physisorbed on graphite have focused on the search for a continuous melting transition.[4] Controversy remains because of the difficulty in distinguishing between a continuous phase transition and a broadened first-order transition. Heat capacity measurements have argued both for continuous melting, in the case of ethylene monolayers and submonolayers,[19] and against, in the case of argon submonolayers[20] and complete xenon monolayers.[21] These conclusions are in conflict with x-ray diffraction and compressibility measurements.[4] What is clear is that the behaviors seen are related to the degree of commensurability between the bulk solid adsorbate and the graphite lattice and the corrugation of the physisorption potential.[4]

Other substrates have been investigated for physisorption studies. Magnesium oxide smoke is prepared by burning magnesium in air and baking the ashes under vacuum at 900 °C. It has uniform surfaces with square symmetry, but the physisorption potential for ^{4}He is even more

corrugated than on graphite. Mylar and mica have also been used but those surfaces are difficult to characterize and clean. It has been found that the ^{4}He/graphite potential can be weakened by plating the graphite with an incommensurate monolayer of a noble gas;[22] however, this can result in commensuration effects comparable to those on graphite.

1.4 Metal Substrates

An alternative to graphite is a metallic substrate. The electronic wave function extends further out from the surface of a transition metal than from graphite, resulting in a physisorption potential which is a factor of two or three smaller than on graphite. The potential on alkali metals (Li, Na, K, Rb, and Cs) is reduced by yet another factor of three or so. Cheng and Cole have predicted that weak binding results in delocalization of the ^{4}He atoms in the direction normal to the surface and consequently a diminishing of the ^{4}He-^{4}He interaction.[23] They propose the formation of a weakly interacting Bose gas at T=0 on the the alkali metals.

In addition to being weaker, the physisorption potentials of metal surfaces are thought to have much less corrugation. The corrugation on insulating substrates results from the localization of the charges close to the surface. Diffraction studies[24,25] with ^{4}He suggest that the corrugation is an order of magnitude smaller on metal surfaces, because of the screening effect of the delocalized conduction electrons.[26] Kern has questioned the applicability of these estimates for heavier adsorbed gases like Xe, because diffracted atoms probe the corrugation of the repulsive part of the potential, while adsorbed atoms see the corrugation of the attractive part.[27] However,

there seems to be general consensus that the corrugation for ^{4}He on metal surfaces should be considerably smaller than that on graphite.[28]

One concern about metal films, especially evaporated ones, is the homogeneity of the surface. Grain boundaries, step edges, and other special binding sites could result in preferential binding of the adsorbate. Despite these effects, uniformity of adsorption potential comparable to that of Grafoil, a type of exfoliated graphite, have been obtained for evaporated films. Domains of (111) oriented crystallites which are 200 Å across have been reported for polycrystalline Ag and Au.[7]

These arguments motivated the heat capacity investigation by Kenny and Richards of ^{4}He adsorbed to evaporated silver films.[29] The physisorption potential seemed to be quite smooth as evidenced by the existence of the adsorbate as a classical 2D gas at high temperature and the absence of any phase transition into a condensed state at temperatures above 1.8 K. After the report of the Bose gas, questions arose concerning possible contamination of the evaporated Ag surface. Kenny reported that at 3 K, the maximum coverage that would stick to the silver substrate was more than a monolayer. Because the binding energy of ^{4}He to silver is so low (52-62 K),[30,31] it might be expected[32] that only a small fraction (<0.1%) of a ^{4}He layer would stick to the silver at 3 K, when surrounded by a cryogenic ($<10^{-9}$ torr) vacuum. To address this concern, we designed a new apparatus which will be described in Chapter 2 which reduces the threat of contamination. In addition, we switched from evaporated Ag to evaporated Au because tests[33] have shown that gold is considerably less reactive than the relatively inert silver, and hence even more difficult to contaminate. The binding energy for noble gases on gold is comparable to that on silver, and thus we expect to

be able to condense at least one layer of ^4He within the accessible temperature range. The extremely small binding energies of the alkali metals prohibit us from using them in our studies.

1.5 Motivation for Experiments

The interplay between adsorbate-adsorbate and adsorbate-substrate interactions is still not fully understood, even in simple systems. Noble gases physisorbed to metal surfaces are very attractive experimental systems to study because of the relative simplicity of the adsorbate-substrate interaction and the availability of theoretical models for comparison. In the narrowest sense, we were motivated to make the heat capacity experiments described in this thesis to address the unanswered questions prompted by previous investigations[29,34] of ^4He and H_2. In a broader sense, however, we hope that these specific experiments will contribute to a better general understanding of physisorbed submonolayers, monolayers, and multilayers.

References

1. H. Wagner, Z. Phys. **206**, 465 (1967).

2. J.M. Kosterlitz and D.J. Thouless, J. Phys. **C6**, 1181 (1973).

3. L.M. Steele, C.J. Yeager and D. Finotello, Phys. Rev. Lett. **71**, 3673 (1993).

4. K.J. Strandburg, Rev. Mod. Phys. **60**, 161 (1988) and references therein.

5. D.R. Nelson and B.I. Halperin, Phys. Rev. **B19**, 2457 (1979).

6. A.P. Young, Phys. Rev. **B19**, 1855 (1979).

7. A.D. Migone, J. Krim, J.G. Dash and J. Suzanne, Phys. Rev. B **31**, 7643 (1985).

8. G. Vidali, G. Ihm, H. Kim and M.W. Cole, Surface Science Reports **12**, 133 (1990) and references therein.

9. E.M. Lifschitz, Sovi. Phys.-JETP **2**, 73 (1956).

10. F.O. Goodman and H.Y. Wachman, Dynamics of Gas-Surface Scattering, (Academic Press, New York, 1976).

11. J.A. Barker and D.J. Auerbach, Surf. Sci. Rep. **4**, 1 (1985).

12. A. Thomy, X. Duval and T. Regnier, Surf. Sci. Rep. **1**, 1 (1981).

13. H.J. Kreuzer and Z.W. Gortel, Physisorption Kinetics, (Springer, Berlin, 1985).

14. J.G. Dash, Films on Solid Surfaces, (Academic Press, New York, 1975) p. 49.

15. E. Giamello, C. Pisani, F. Ricca and C. Roetti, Surf. Sci. **49**, 401 (1975).

16. M. Bretz, J.G. Dash, D.C. Bickernell, E.O. McLean and O.E. Vilches, Phys. Rev. A **8**, 1589 (1973).

17. D.S. Greywall and P.A. Busch, Phys. Rev. Lett. **67**, 3535 (1991).

18. M. Bretz and T.T. Chung, J. Low Temp. Phys. **17**, 479 (1974).

19. H.K. Kim, Q.M. Zhang and M.H.W. Chan, Phys. Rev. Lett. **56**, 1579 (1986).

20. A.D. Migone, Z.R. Li and M.H.W. Chan, Phys. Rev. Lett. **53**, 810 (1984).

21. A.J. Jin, M.R. Bjurstrom and M.H.W. Chan, Phys. Rev. Lett. **62**, 1372 (1989).

22. C. Schwartz and M.W. Cole, Phys. Rev. B **34**, 1250 (1986).

23. E. Cheng and M.W. Cole, Phys. Rev. B **42**, 3960 (1990).

24. G. Boato, P. Cantini and R. Tatarek, J. Phys. F **6**, L237 (1976).

25. J.M. Horne and D.R. Miller, Surf. Sci. **66**, 365 (1977).

26. J. Unguris, L.W. Bruch, E.R. Moog and M.B. Webb, Surf. Sci. **109**, 522 (1981).

27. K. Kern, Vacuum **41**, 389 (1990).

28. L.W. Bruch, private communication.

29. T.W. Kenny and P.L. Richards, Phys. Rev. Lett. **64**, 2386 (1990).

30. A. Luntz, L. Mattera, M. Rocca, F. Tommasini and U. Valbusa, Surf. Sci. **120**, L447 (1982).

31. D. Eichenauer, U. Harten and J.P. Toennies, J. Chem. Phys. **86**, 3693 (1987).

32. P. Taborek, Phys. Rev. Lett. **65**, 2612 (1990).

33. E.B. Graper, J. Vac. Sci. Technol. A **9**, 591 (1991).

34. R.B. Phelps, J.T. Birmingham and P.L. Richards, J. Low Temp.

2. Apparatus and Experimental Procedures

2.1 Introduction

The apparatus used in the experiments described in Chapters 3 and 4 was designed to extend and improve upon measurements[1,2] performed in the older system discussed previously.[3] Three major changes were made. First, the minimum accessible temperature was reduced from 1.5 K to 0.28 K by incorporating a ^{3}He sorption refrigerator based on the design by Duband *et al.*[4] Second, the calorimeter was made of a thin piezoelectric quartz plate, rather than sapphire, and was operated as a microbalance to provide a direct measure of the adsorbate coverage. Third, the risk of contamination of either the evaporated gold film or the adsorbate was reduced by a design in which most surfaces in the new system are in good thermal contact with the liquid ^{4}He bath, even during gold evaporation.

This chapter is organized as follows: In Section 2.2 we discuss the two techniques used, AC calorimetry and quartz microweighing. The construction, operation, and performance of the calorimeter/microbalance are also covered there, as well as the electronics used in the two techniques. In Section 2.3 we describe the cryogenic system. In Section 2.4 we discuss how the gold film is evaporated *in situ*. The room temperature gas handling system and the condensation of the hydrogen and helium films are described in Section 2.5. Most of the experimental procedures are the same for the hydrogen and helium experiments. Procedures particular to one or the other experiment will be noted and described more fully in the appropriate later chapter.

2.2 Calorimeter/Microbalance

We have constructed a detector which serves as both an AC calorimeter and a microbalance, so that we can simultaneously measure the heat capacity and the coverage of an adsorbed film and from those quantities deduce the specific heat, or heat capacity per particle.

2.2.1 Calorimeter Construction and Operation

The quartz calorimeter used in this work was adapted from the sapphire calorimeter used by Kenny[1,3] and later by Phelps[2] in the experiments mentioned in the Preface and Chapter 1. The earlier device in turn was inspired by composite bolometers[5] used as sensitive detectors of far-infrared radiation, primarily for astrophysical observation. In a far-infrared bolometer, a small heat capacity C is coupled to a bath at temperature T_0 via a weak thermal link G. Optical power is absorbed by the bolometer, and the temperature rise ΔT is detected by a thermometer. In an AC calorimeter, AC electrical power is dissipated in the device, and the heat capacity is computed from the amplitude of the temperature fluctuations.

Our device is constructed from a quartz single crystal and is shown in Figure 2.1. The switch from sapphire to quartz was made to incorporate the microbalance, which will be discussed later in the section. After ultrasonic cleaning in sequential baths of tricholorethane, acetone, and methanol, the crystal is suspended under tension by three 125 μm diameter nylon fibers. Four single crystal neutron-transmutation-doped Ge thermistors,[6] two nichrome resistive heaters on Si substrates,[7] and a chromel/alumel thermocouple are epoxied[8] to the back side of the substrate. They are attached far from the acoustically active region of the quartz, which is

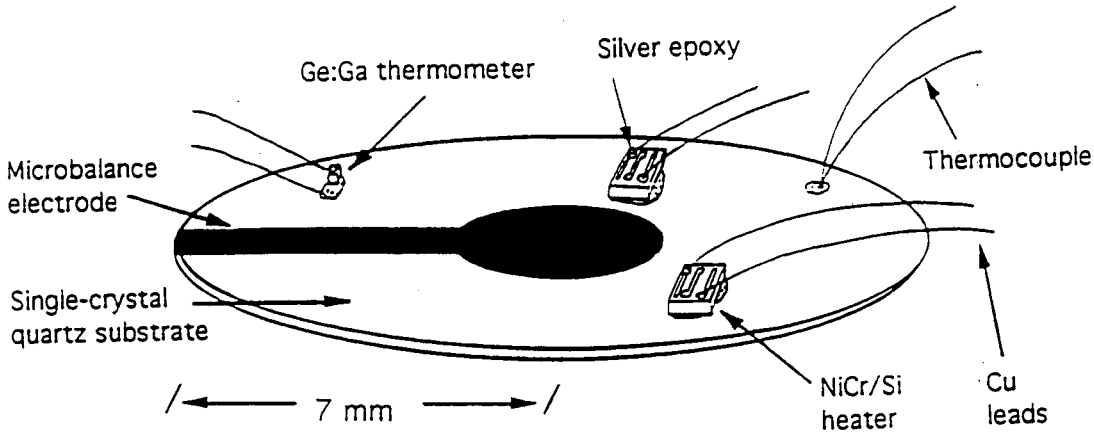

Figure 2.1 Back (upper) side of quartz calorimeter/microbalance. The heaters and thermometers used for calorimetry are epoxied far from the acoustically active region. On the front (lower) side, not shown, a gold film has been evaporated as described in the text.

defined by gold electrodes previously evaporated on both sides of the substrate, so as not to degrade the performance of the microbalance. The Ge thermistors are cut in the shape of 250 μm cubes and have been calibrated against a commercial thermometer[9] for $0.3 < T < 4.2$ K, and their resistances are well described by an expression for variable range hopping in the presence of a Coulomb gap:

$$R(T) = R_0 \exp((T_0/T)^{1/2})\exp(-eEL/k_BT) \quad , \tag{2.1}$$

where e is the charge of an electron, E is the electric field and L is the characteristic length for hopping. The low temperature thermistor material, known as NTD-6, has $T_0 \approx 40$ K and is useful for the range $0.3 < T < 1.6$ K; the high temperature resistor (NTD-5) with $T_0 \approx 100$ K is useful for $T > 1.4$ K. We apply maximum voltages of 10 mV and 40 mV, equivalent to fields of 40 V/m and 160 V/m across the low and high temperature thermistors, respectively. Calibration curves for the two thermometers in Figure 2.2 show that at these field strengths, $eEL/k_BT \ll 1$, and the second factor in Equation 2.1 is very nearly unity. In this case, Equation 2.1 reduces to

$$R(T) = R_0 \exp((T_0/T)^{1/2}) \ . \tag{2.2}$$

The thermal response of the calorimeter can be well described by the one-dimensional circuit shown in Figure 2.3. The heat capacity C is dominated by the Debye contribution of the quartz. The weak thermal link G between the calorimeter and the cold stage of the ^{3}He refrigerator is provided by four 25 μm diameter copper or gold wires, each approximately

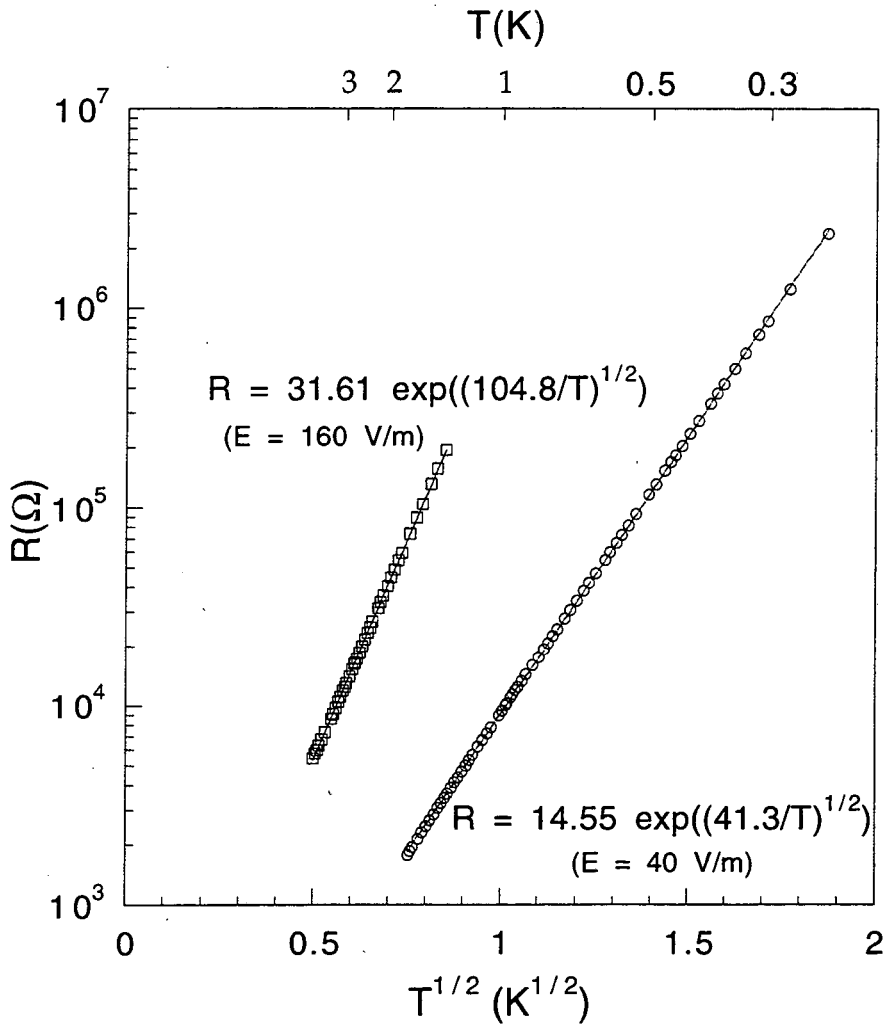

Figure 2.2 Typical calibration curves for the high (squares) and low (circles) temperature thermometers.

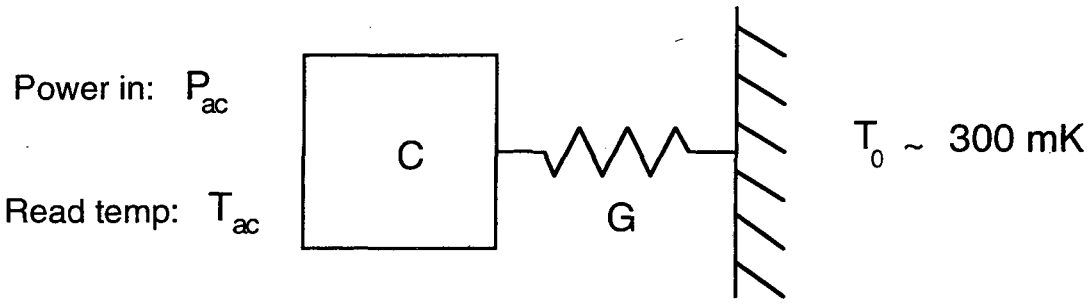

Figure 2.3 Equivalent thermal circuit of the calorimeter. The heat capacity C is dominated by the quartz substrate; the thermal conductance G is provided by four 0.001" diameter gold or copper wires.

one centimeter in length. One of the two heaters is used to regulate the average substrate temperature. The other is AC biased at frequency $\omega/2$ to produce ~1 mK temperature oscillations of frequency ω. From the one-dimensional heat equation, we find

$$T_{ac} = \frac{P_{ac}}{|G + i\omega C|} \quad , \tag{2.3}$$

where P_{ac} is the AC power of frequency ω and T_{ac} is the magnitude of the temperature fluctuation.[10] The thermal time constant τ of the calorimeter is equal to C/G. When the frequency of oscillation is much faster than $1/\tau$, Equation 2.3 reduces to

$$C = P_{ac}/(\omega T_{ac}) \ , \tag{2.4}$$

which is independent of the thermal conductance G.

The heat capacity of the adsorbate is measured by subtracting the heat capacity of the bare calorimeter from that of the adsorbate-covered calorimeter. The minimum change in heat capacity that we can measure is ~10^{-12} J/K at 0.4 K and ~10^{-10} J/K at 2.0 K. The resolution decreases rapidly with increasing temperature, because the adsorbate-covered device heat capacity is dominated by the Debye contribution from the quartz above ~1.5 K. The switch from sapphire is not without a price, as the Debye temperature of quartz[11] is 552 K compared with 1035 K for sapphire.[12]

2.2.2 Calorimetry Electronics

The measurement system is shown in Figure 2.4. Two thermistor chips of each type are attached to the calorimeter. The resistance of one of the chips is measured by a resistance bridge[13] and fed into a PID control unit,[14] which adjusts the power dissipated in one of the two heaters to regulate the mean calorimeter temperature. To measure the temperature oscillation generated by the second AC heater, we pass a DC current through the other thermistor and measure the voltage oscillation V_{ac} with a lock-in amplifier.[15]

In the case of a current bias, which maximizes the signal-to-noise ratio, the heat capacity can be expressed as

$$C = \frac{V_{dc}\alpha V_H^2}{2R_H\omega V_{ac}} \quad , \tag{2.5}$$

where $\alpha \equiv |(1/R)(dR/dT)|$, V_{dc} is the DC bias across the thermistor, and V_H is the heater voltage dissipated in resistance R_H. To confirm that we are in the frequency regime specified by Equation 2.4 we plot $V_{ac} \times$ frequency versus frequency and look for the region where the curve is flat as shown in Figure 2.5. Typically, we chop P_{ac} somewhere between 200 and 500 Hz. Above 1 kHz electrical RC roll-offs become important when the resistance is of order 100 kΩ or more.

There is a disadvantage of the current bias mode, however. The signal V_{ac} decreases very rapidly with increasing temperature because $C \propto T^3$, $\alpha \propto T^{-3/2}$, and $V_{dc} \propto \exp((T_0/T)^{1/2})$. Either the lock-in range must be constantly changed, introducing phase and offset errors, or P_{ac} must be constantly adjusted to keep the signal at an adequate level. We have

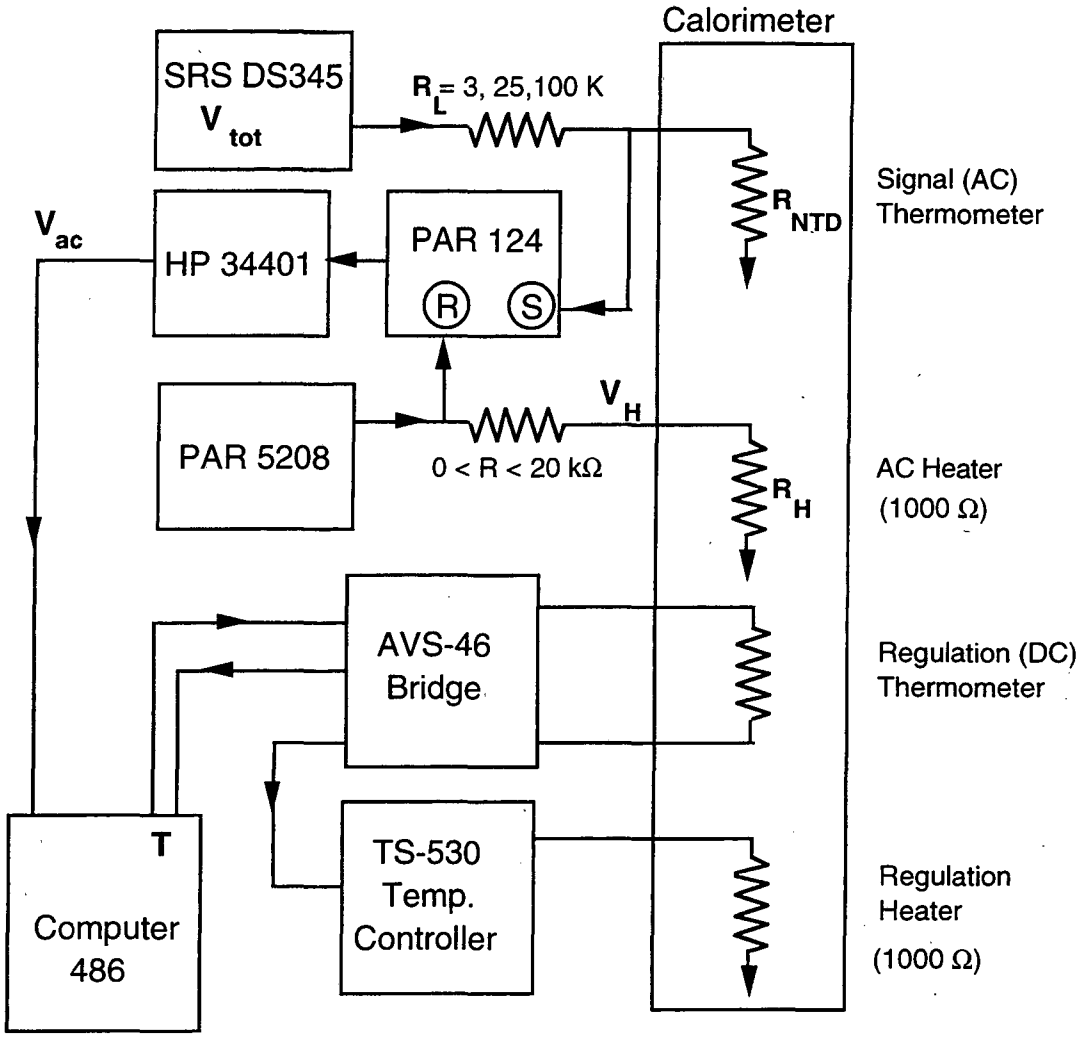

Figure 2.4 The electronics scheme for calorimetry. A DC bias $\mathbf{V_{tot}}$ generated by the SRS DS345 frequency synthesizer is applied to the load resistor $\mathbf{R_L}$ and the cold thermistor $\mathbf{R_{NTD}}$ in series. The amplitude of an AC voltage $\mathbf{V_H}$ generated by the PAR 5208 is adjusted by a load resistor $0<R<20$ kΩ and applied to the cold heater R_H. The voltage oscillation $\mathbf{V_{ac}}$ across R_{NTD} is measured using the PAR 124 lock-in amplifier in the 2f mode, where the signal frequency (S) is twice the reference (R). A computer controls the temperature **T** via a bridge/controller combination and reads the value of $\mathbf{V_{ac}}$. The quantities V_{tot} and V_H and thermistor calibrations are manually entered into the program, which calculates the heat capacity from Equation 2.6.

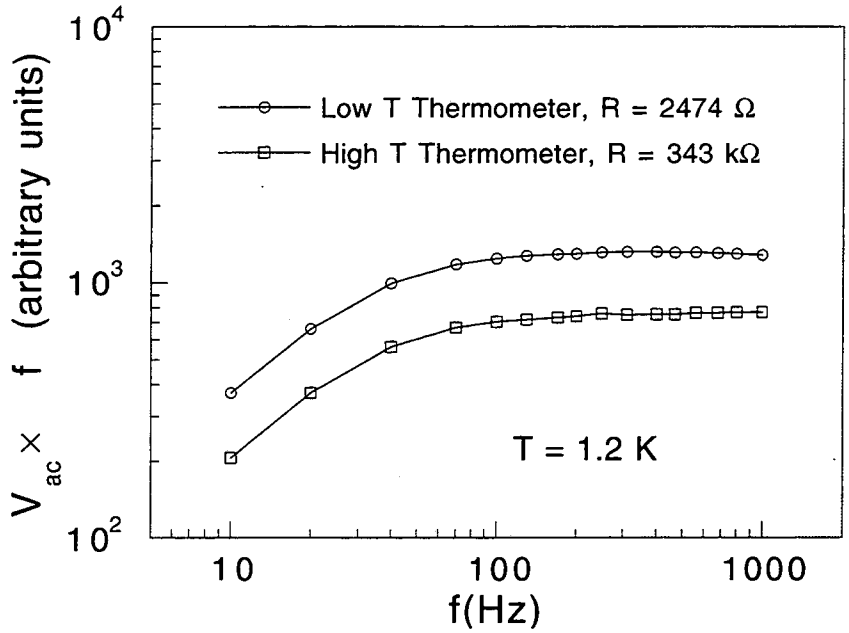

Figure 2.5 Plot of $V_{ac} \times$ frequency versus frequency for both thermistors for T=1.2 K. Equation 2.4 is valid over the region where the curve is flat.

therefore chosen to operate in a mode in between current and voltage bias, sacrificing signal-to-noise for the sake of dynamic range. We apply a DC bias V_{tot} (for "total" bias) to the calorimeter thermistor R_{NTD} in series with a load resistor R_L which has been chosen to have resistance about equal to that of the NTD thermometer when the calorimeter is in the middle of the temperature scan. Equation 2.5 is then replaced by

$$C = \frac{R_{NTD} R_L}{(R_{NTD}+R_L)^2} \frac{V_{tot} \alpha V_H^2}{2 R_H \omega V_{ac}} \quad . \tag{2.6}$$

At low temperatures, $R_L \ll R_{NTD}$, $V_{tot} \approx V_{NTD}$, and the signal is reduced by a factor (R_L/R_{NTD}); at high temperatures, $R_L \gg R_{NTD}$, and Equation 2.6 reduces to Equation 2.5. For temperatures between 0.3 and 0.6 K where the NTD thermistor resistance typically varies from 600 kΩ to 20 kΩ, we choose the load resistance to be 100 kΩ. Between 0.6 and 1.6 K the resistance decreases from 20 kΩ to 1500 Ω, and we use R_L = 3 kΩ. The high temperature thermistor varies from roughly 200 kΩ at 1.4 K to 6 kΩ at 3 K, and we use R_L = 25 kΩ.

In an ideal calorimeter, the signal-to-noise ratio is limited by fluctuations in the thermal conductance and Johnson noise in the thermistor.[3] However, in our system, noise in the lock-in preamplifier ($5\ nV/\sqrt{Hz}$) and noise introduced by imperfect temperature regulation (100 μK stability) are predominant. The combination of all these sources of noise results in a signal-to-noise ratio of several thousand over the entire temperature range for one second of integration time when the signal V_{ac} is of order 20 μV. When we make measurements of the same bare calorimeter several hours apart, we find that 1/f amplifier drift is an issue. To address

this problem, we measure the bare calorimeter before and after measuring the adsorbate-covered device, and from the differences in the bare scans, we make a linear estimate of the drift rate. The obvious best strategy, however, is to make all measurements as quickly as reasonably possible, especially when the adsorbate is only a fraction of a layer thick, with contribution to the heat capacity of less than 0.2% of the total. Our initial investigations in both the hydrogen and helium projects were used to determine the amplitude and width of heat capacity features and hence to decide what minimum signal-to-noise and temperature resolution were needed to resolve them.

2.2.3 Microweighing

Quartz is a piezoelectric material: an applied voltage results in a strain and vice versa. This property has been utilized to produce very high performance filter and oscillator circuits.[16] It has long been known that the frequency of a radio transmitter incorporating a quartz crystal could be lowered by marking the crystal with a pencil and thereby adding mass to the oscillating crystal face. Sauerbrey extended this idea in 1959 to use quartz crystal oscillators for weighing very small quantities of deposited material.[17] In our experiment, we look for frequency shifts as small as a few hundredths of a Hz which result from the condensation of a fraction of an adsorbed monolayer of hydrogen or helium to the crystal face.

The piezoelectric and elastic properties of a quartz crystal are axis-dependent. The most common crystal orientation used for microweighing is the AT-cut, in which the face of the crystal is perpendicular to one of the principal crystal axis, and which has been cut to have mimimum temperature sensitivity when operated in oscillator circuits near room

temperature. The resonance in quartz results from the relationships between strain and voltage, determined by the piezoelectric constants, and between stress and strain, determined by the elastic constants. Using a simple one-dimensional treatment[16] one can show that the electrical response of a quartz crystal plate to an applied AC voltage is identical to that of a geometrical capacitance in parallel with an LRC circuit, as shown in Figure 2.6, with circuit elements

$$C_0 = \varepsilon_0 \frac{A}{t} \quad ; \quad R_m = \frac{t^3 r}{8A\varepsilon^2} \quad ; \quad L_m = \frac{t^3 \rho}{8A\varepsilon^2} \quad ; \quad C_m = \frac{8A\varepsilon^2}{\pi^2 tc} \quad . \tag{2.7}$$

where

A	=	Area of plate	r	=	Damping coefficient
t	=	Thickness of plate	ε	=	Piezoelectric stress constant
c	=	Elastic constant	ε_0	=	Susceptibility of free space
d	=	Strain constant	ρ	=	Density of quartz
k	=	Dielectric constant			

The subscript "m" is used to emphasize that the circuit elements describe the motion of the crystal and do not have values typical of standard electrical components. For a 6 MHz AT-cut crystal, approximate values for the circuit parameters are

$$C_0 = 1\,\text{pF} \quad ; \quad R_m = 50\,\Omega \quad ; \quad L_m = 0.2\,\text{H} \quad ; \quad C_m = 4 \times 10^{-15}\,\text{F} \quad .$$

The LRC circuit has a series resonance at $\omega_r = 1/\sqrt{L_m C_m}$ and a parallel resonance at $\omega_p = \sqrt{\frac{1}{L_m C_m} + \frac{1}{L_m C_0}} \approx \omega_r \left(1 + \frac{C_m}{2C_0}\right)$. From the expressions for L_m

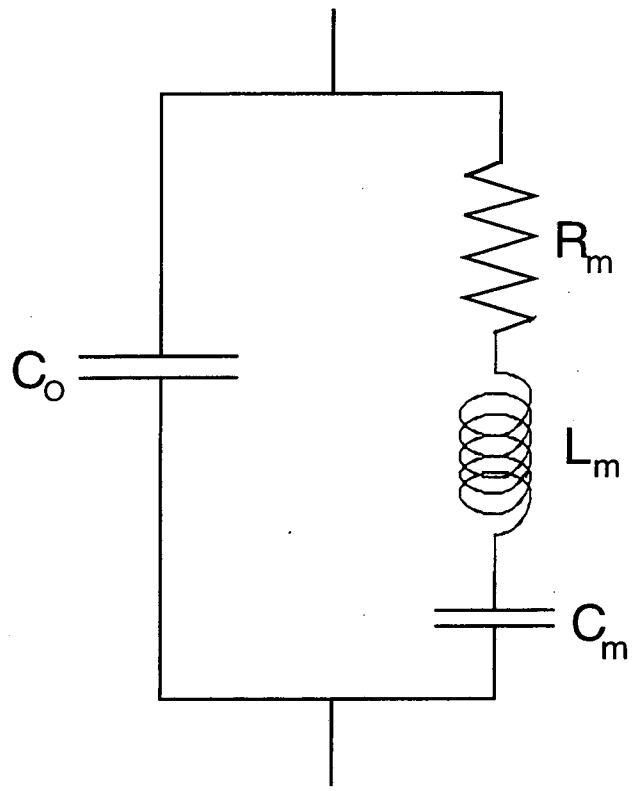

Figure 2.6 The equivalent circuit for the quartz substrate.

and C_m, one sees that the series resonant frequency is inversely proportional to the thickness of the plate. The mode corresponding to this resonance is a shear mode, where the motion is perpendicular to the normal to the face of the plate as shown in Figure 2.7. The wavelength of the fundamental resonance is equal to twice the crystal thickness, and the resonant frequency f_0 can be related to the thickness via a cut-dependent constant K:

$$f_0 = K/t \quad . \tag{2.8}$$

For AT-cut crystals, K = 1670 mHz; for the SC-cut crystals used in the hydrogen experiment, K = 1813 mHz.

If a film with mass density $\Delta m/A$ is attached to the acoustically active region of the quartz substrate, which is defined by the overlap of the electrodes evaporated on each side of the substrate, the resonant frequency shifts downward by an amount proportional to the mass

$$\frac{\Delta f}{f_0} = -K_n \frac{(\Delta m/A)}{\rho\, t} \quad . \tag{2.9}$$

The constant K_n, which describes non-ideal behavior, is within 2% of unity.[18] Equation 2.9 is valid for mass coverages of up to 1700 μg.[17-19]

There can also be a frequency shift of the resonance without any mass actually adhering to the substrate. Away from 300 K, the resonant frequency depends on temperature, because of the temperature dependence of the various constants which determine the equivalent circuit elements. If the substrate is in a gaseous environment, the crystal can be subject to a hydrostatic pressure, which shifts the resonance upwards,[18] and to viscous

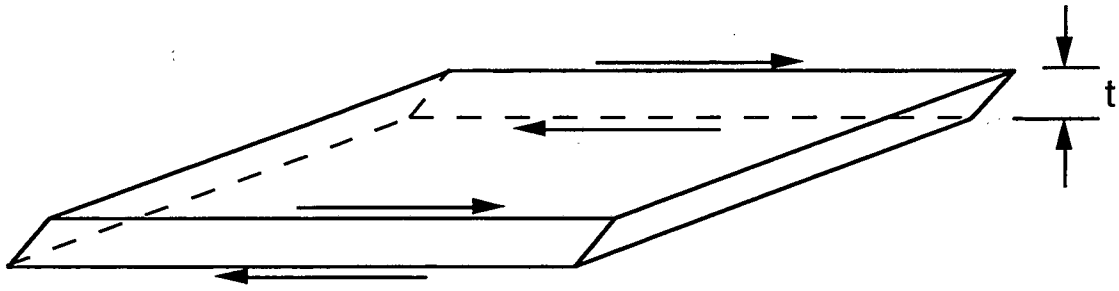

Figure 2.7 Thickness shear mode of oscillation

forces, which increase the effective inertia of the crystal and hence decrease the resonant frequency.[20] In our experiment, we regulate the temperature of the substrate with better than 100 μK stability, and so the shift associated with temperature changes should be insignificant compared with that resulting from mass adsorption.[21] Because the walls of our vacuum chamber are at ~1.3 K, there is no vapor but rather a cryogenic vacuum above the adsorbed film, and so there is no correction required for the pressure or viscosity effects.

An additional complication which does affect our interpretation of the resonance shift in thin hydrogen films is a frequency shift resulting from a surface stress on one of the crystal faces. This effect results from the dependence of the resonant frequency on the thickness, mass density, and elastic properties of the substrate, all of which are modified by the stress. This effect is discussed further in Section 3.5.

To measure the frequency shift of the microbalance resonance, we have used it as a component in the circuit shown in Figure 2.8. A DC biased commerical oscillator circuit[22] excites a ~6 MHz resonance. The RF signal is downshifted to kHz frequencies by mixing it with a sinusoidal reference signal of nearly the same frequency generated by a digital frequency synthesizer.[23] The low frequency mixer[24] output signal is counted by an HP 34401A multimeter.[25] Using this technique, we can determine resonance shifts of ~0.03 Hz, corresponding to roughly 1/20th of a ^{4}He monolayer or 1/10 of a H_2 monolayer. To avoid parasitic capacitances that reduce the Q of the circuit, we use teflon-coated copper wires which are located in the stainless steel apparatus support tubes to form coaxial lines. Careful attachments of the thermometers, heaters, and wires required for

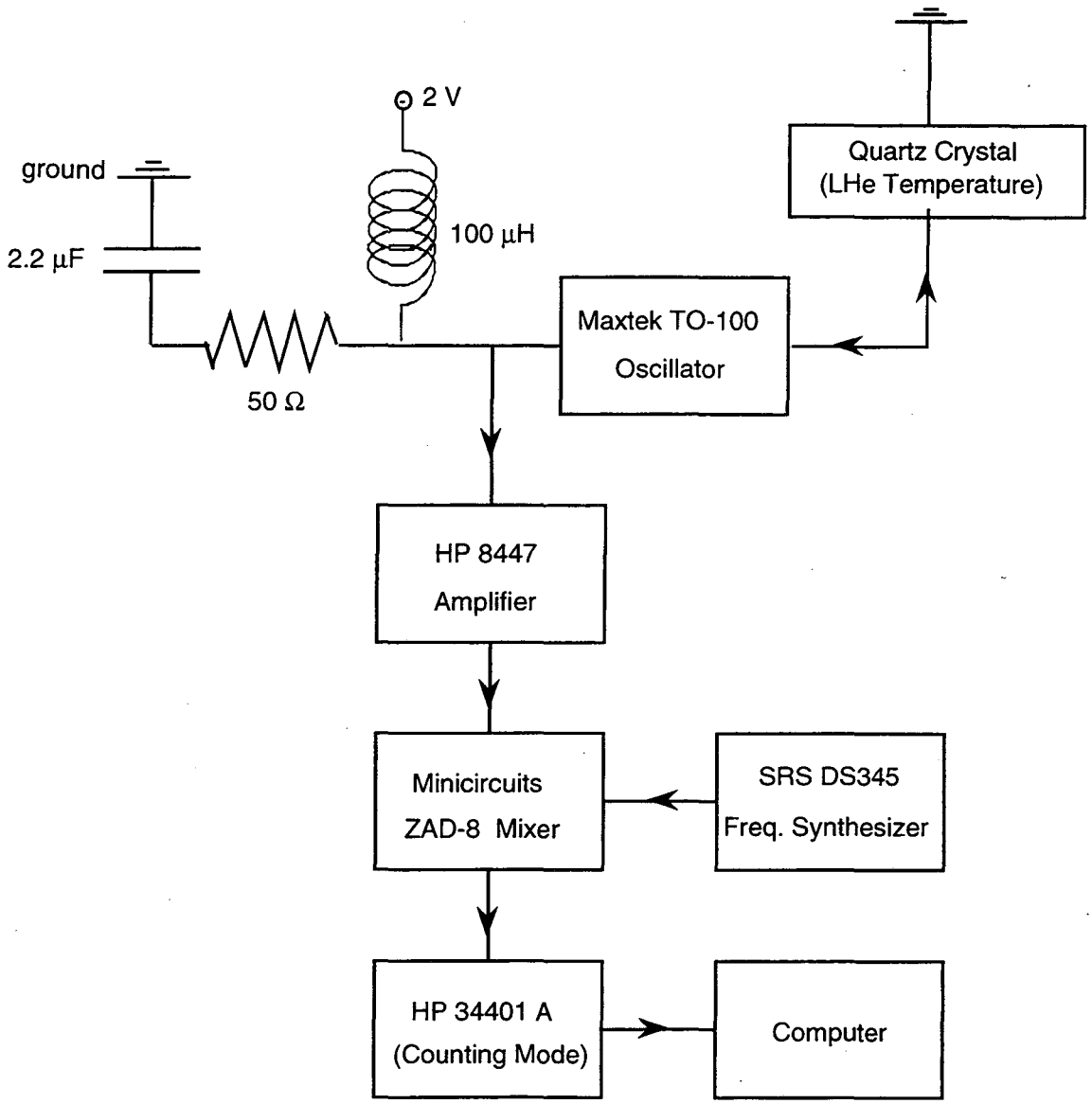

Figure 2.8 Electronics scheme for measuring microbalance resonance. The resonant frequency (MHz) of the quartz crystal circuit is mixed with a reference signal from the frequency synthesizer. The mixer output (kHz) is counted by the multimeter.

calorimetry do not significantly degrade the Q of the resonance. Typical values of Q of 5×10^4 - 10^5 are obtained when the fully assembled calorimeter is cooled in vacuum to liquid helium temperatures.

2.3 Cryogenic System

The cryogenic insert which houses the experiment was designed to fit into a helium dewar with a 4 3/4" inner diameter. The hold time of the dewar plus apparatus is approximately 36 hours for unpumped LHe (liquid ^{4}He.) During experiments the LHe was pumped to achieve a bath temperature of ~1.3 K. At the bottom of the cryostat insert is the vacuum can shown in Figure 2.9 in which the heat capacity experiments are made, supported by four 1/4" diameter (0.020" thick) stainless steel tubes. The vacuum seal is an o-ring made from 0.062" diameter indium wire squeezed between the stainless steel can and a stainless steel base plate on the insert. The vacuum chamber enclosed is cryopumped by activated charcoal and constructed primarily from UHV-compatible materials, 304 stainless steel and OFHC copper. UHV compatible epoxy[26] was used only when absolutely necessary. Copper plugs inserted through the stainless steel base plate and hard soldered in place served as heat sinks.

Temperatures down to 280 mK are achieved through use of a ^{3}He sorption refrigerator.[4] The calorimeter/microbalance is connected to the cold stage of the refrigerator through a weak thermal link, as described in Section 2.2. Operation of the refrigerator is very easy. The pump is heated to ~40 K to drive the ^{3}He out of the charcoal. The desorbed ^{3}He collides with the ~2 K condensing point and liquid falls into the still. When the pump

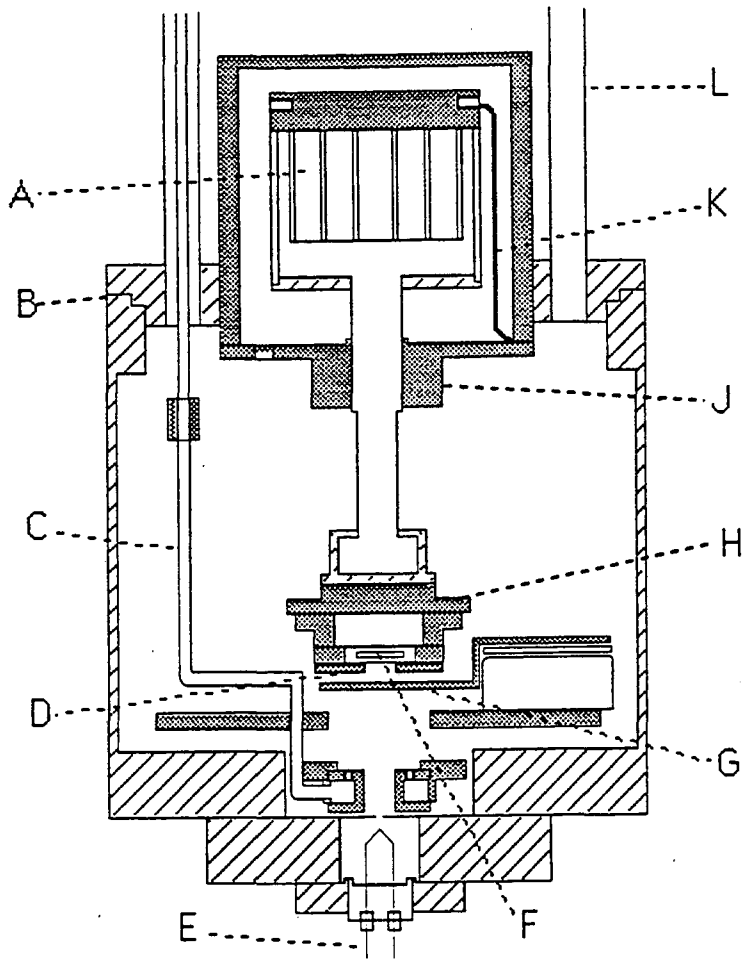

Figure 2.9 Experimental apparatus, immersed in a liquid ^{4}He bath at 1.3 K. Diagonally shaded regions are 304 stainless steel; gray shaded regions are OFHC copper. Important features include A: Charcoal pump for the ^{3}He refrigerator, B: Indium o-ring, C: Copper effusion line/cell (3 - 120 K), D: Evaporation mask, E: Gold evaporation filament, F: Calorimeter/microbalance, G: Shutter, H: 0.28 K cold stage of the ^{3}He refrigerator, J: Condensing point (2 K) for ^{3}He refrigerator, K: Tin heat switch, and L: Stainless steel support tube.

heater is turned off, the charcoal cools via a heat switch made from a piece of tin wire, 1.5 mm in diameter and ~3 cm in length. When the pump temperature falls below 6-7 K, the ^{3}He begins to adsorb to the charcoal, and the pressure above the still is reduced, cooling the cold stage. The refrigerator has a cooling capacity of about 1 Joule and a hold time of 14 hours in the absence of additional power loading.

The electrical leads for the experiment are brought from 300 K through the 1/4" diameter stainless steel support tubes and are heat sunk at both 1.5 and 0.28 K. The adsorbate to be studied is brought down through a 1/8" diameter (0.012" thick) stainless steel tube which is centered in one of the support tubes by a teflon spacer. The bottom end of the small tube is hard soldered to the copper effusion line shown in Figure 2.9. The effusion line is discussed further in Section 2.5.

2.4 Evaporation of the Gold Film

Before the adsorbate is deposited, a new gold surface is evaporated *in situ* on the bottom of the calorimeter. This gold is evaporated from a 0.020" diameter tungsten filament located directly below the calorimeter/microbalance. The filament is prepared before assembly of the dewar and the cool-down. The tungsten wire is sharply kinked to produce a high resistance "hot spot" and wrapped with clean 250 μm diameter gold wire. The gold-wrapped filament is clamped between electrodes in a bell jar which is pumped down below 10^{-7} torr. Several amps of AC current are passed through the filament to heat the filament and gold to a temperature that is just below the melting point of the gold. Both are outgassed for 30

minutes. The current is increased until the gold melts and forms a ~200 μm diameter ball centered on the tip of the filament. The filament is allowed to cool and then spot welded to a cryogenic feedthrough[27] mounted on a standard UHV Conflat flange. In order to minimize radiative heating of the chamber during gold evaporation, we replaced the copper gasket normally used with the flange by a specially machined 1/8" thick copper gasket which is directly cooled by the LHe bath. The hole drilled in the thick gasket is small enough to shield the calorimeter and vacuum chamber from much of the black body radiation from the filament. After the flange is bolted onto the vacuum can, the rig is inserted into the dewar and pumped down overnight to a pressure of 10^{-6} torr with a turbopump. The dewar is first precooled with LN_2 and then filled with LHe.

During evaporation all surfaces other than the filament and the substrate are maintained below 5 K, and so the gold surface is expected to have very little contamination. Before evaporation, the filament is heated to a temperature just below the melting temperature of gold. A solenoid-controlled copper shutter between the evaporator and the calorimeter/microbalance is closed during this outgassing so that there is no direct line of sight to the substrate. The solenoid[28] was degreased prior to apparatus assembly, both for cleaning purposes and to prevent freezing of the lubricants upon cooling. A second quartz substrate[29] used as a thickness monitor is mounted on the shutter and is used to determine the melting point of the gold and later to allow regulation of the evaporation rate. While the gold is being outgassed, the substrate itself is also outgassed by heating it to 100 °C by applying approximately 12 V to each of the two 1000 Ω heaters on the calorimeter.

After fifteen minutes, the substrate temperature is reduced to 80 K, the shutter is opened, and the evaporation is begun. Typically, 500-800 Å of gold are evaporated at a rate of 1-2 Å/sec by passing ~7 A rms of AC through the filament. The shutter is closed periodically to check and adjust the evaporation rate. The gold spot evaporated on the calorimeter/microbalance is defined by an evaporation mask located approximately 200 μm below the substrate. After evaporation, the substrate is annealed at 50 °C for fifteen minutes. Upon completing the experiments and opening the cryostat, we have examined the gold surface with an atomic force microscope (AFM). It appeared smooth and featureless on the 100 Å length scale. We suspect that the surface contains (111) crystallites that are smaller than this length scale.

2.5 Condensation of the Adsorbate

After a fresh gold film has been evaporated, the calorimeter is ready for hydrogen or helium condensation. We have designed the gas handling system to minimize the possibility of contaminating the adsorbate. The system consists of two parts: external room temperature plumbing and a cooled effusion line and cell.

2.5.1 External Room Temperature UHV Plumbing

The external plumbing is shown in Figure 2.10 and has been assembled from stainless steel tubing and metal valves, all of which can be baked for cleaning. Before dosing, valves B-F are opened and the external system is heated to 150 °C for 12 hours while being pumped by a turbopump to achieve a pressure in the line of $< 2\times10^{-7}$ torr. After the bake-out, valves B-F are closed. Valve A is opened, allowing high pressure gas into the short

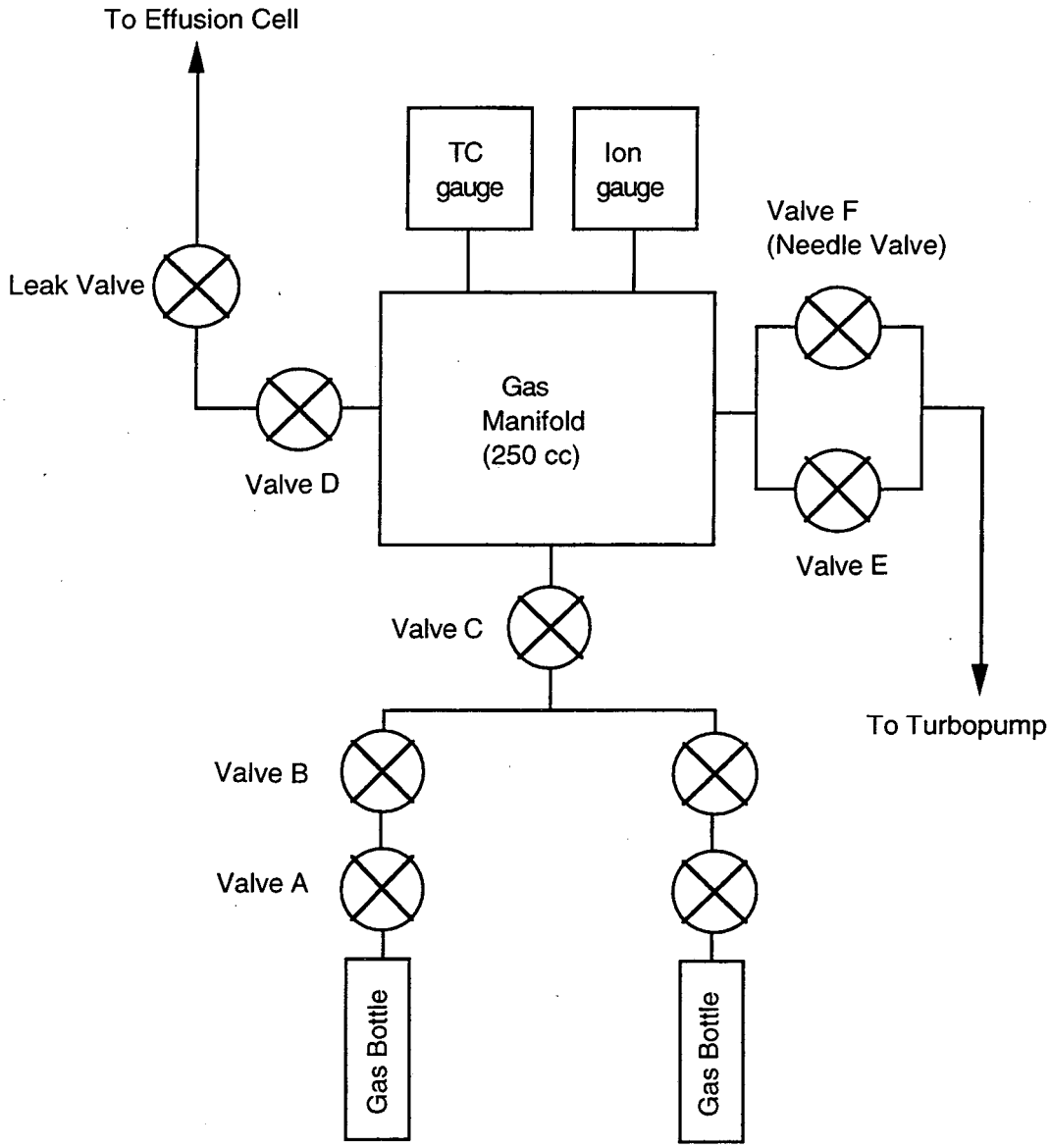

Figure 2.10 Room temperature gas handling system.

piece of tube between A and B. A is closed and B is opened; the pressure in the tube between B and C is now just above atmospheric pressure. Valve C is quickly opened and closed to allow some gas into the manifold. Valve F is opened to the turbopump and remains open until the desired pressure in the manifold is achieved, (10-200 mtorr for multilayer H_2 films, ~1 mtorr for submonolayers of helium.) The leak valve is adjusted to the appropriate flow rate, and valve D is opened to begin the adsorption.

2.5.2 Cooled Effusion Line and Cell

The room temperature tubing connects to the liquid helium-cooled copper effusion line and cell shown in Figure 2.9. The torus-shaped effusion cell is located 2 cm below the calorimeter. Two 0.025 cm diameter holes are symmetrically spaced on the torus face directed towards the calorimeter. The temperature of the copper plumbing, and hence the stainless steel tube, is adjusted via a 300 Ω heater attached to the copper line. When the heater is turned off, the line cools to approximately 3 K. In the hydrogen experiments described in Chapter 3, the effusion line was heated above 80 K to prevent the unwanted conversion of J=1 H_2 molecules in the stainless steel tube during effusion. For the helium experiment, the effusion cell was kept between 5 and 6 K, warm enough so that the helium would not stick to the walls on the way down the tube, but cold enough such that all impurity gases would be frozen out. After the leak valve is opened, the adsorbate takes a few seconds to travel down to the effusion cell, from which it is sprayed onto the calorimeter/microbalance. The condensation rate is measured using the detector's microbalance capability, and when the desired coverage is reached,

the leak valve is closed. Heat capacity measurements of the condensed film can begin.

References

1. T.W. Kenny and P.L. Richards, Phys. Rev. Lett. **64**, 2386 (1990).

2. R.B. Phelps, J.T. Birmingham and P.L. Richards, J. Low Temp. Phys. **92**, 107 (1993).

3. T.W. Kenny and P.L. Richards, Rev. Sci. Instrum. **61**, 822 (1990).

4. L. Duband, A. Lange and A. Ravex, 1991, *4th European Symposium on Space Enviornmental and Control Systems*, Florence, Italy, p. 407.

5. P.L. Richards, J. Appl. Phys. **76**, 1 (1994).

6. E.E. Haller, N.P. Palaio, M. Rodder, W.L. Hansen and E. Kreysa, in Neutron Transmutation Doping of Semiconductor Materials, edited by R. D. Larrabee (Plenum, New York, 1984), p. 21.

7. MSTF-3-S-N-1K-02, Mini-Systems, Inc., North Attleboro, MA 02761.

8. Epo-Tek H20E, Epoxy Technology, Inc., Billerica, MA 01821.

9. GR-200A-100, Lake Shore Cryotronics, Inc., Westerville, OH 43081.

10. P.F. Sullivan and G. Seidel, Phys. Rev. **173**, 679 (1968).

11. R.C. Zeller and R.O. Pohl, Phys. Rev. B **4**, 2029 (1971).

12. R.W. Fugate and C.A. Swenson, J. Appl. Phys. **40**, 3034 (1969).

13. AVS-46, RV-Elektroniikka Oy, SF-01510 Vantaa, Finland.

14. TS-530, RV-Elektroniikka Oy, SF-01510 Vantaa, Finland.

15. PAR 124, Princeton Applied Research Corp., Princeton, NJ 08543.

16. V.E. Bottom, Introduction to Quartz Crystal Unit Design, (Van Nostrand Reinhold Company, New York, 1982).

17. G. Sauerbrey, Zeit. fur Physik **155**, 206 (1959).

18. C.D. Stockbridge, Vacuum Microbalance Techniques, (Plenum Press, New York, 1966).

19. H.L. Eschback and E.W. Krudhof, Vacuum Microbalance Techniques, (Plenum Press, New York, 1966).

20. A.W. Warner, in Ultra Microweight Determination in Controlled Environments , edited by S. P. Wolsky and E. J. Zdanuk (Interscience Publishers, New York, 1969).

21. J. Krim, Thesis, Univ. of Washington (1984).

22. SO100, Maxtek, Inc., Torrance, CA 90503.

23. SRS DS345, Stanford Research Systems, Sunnyvale, CA 94089.

24. ZAD-8 Mixer, Mini-Circuits, Brooklyn, NY 11235.

25. HP 34401A, Hewlett-Packard Co., Santa Clara, CA 95052.

26. Torr Seal, Varian Vacuum Products, Lexington, MA 02173.

27. 807B9852-01-B, Ceramaseal, New Lebanon Center, NY 12126.

28. H-1151-033, Ledex Inc., Vandalia, OH 45377.

29. SC-102, Maxtek, Inc., Torrance, CA 90503.

3. Heat Capacity of Quench-Condensed Hydrogen Films

3.1 Introduction

3.1.1 Ordering in Solid Hydrogen

Molecular hydrogen, cooled to liquid helium temperatures, is a mixture of ortho-H_2 (odd angular momentum J) in its lowest state J=1, and of para-H_2 (even J) where J=0. Molecules with J=1 possess an electric quadrupole moment and have a higher rotational energy than the spherically symmetric molecules with J=0. Hydrogen crystallizes from the liquid into the hcp structure for all fractional concentrations X of the J=1 state. Throughout this chapter, we will refer to this homogenous solid as "bulk" hydrogen. The anisotropic electric quadrupole-quadrupole interactions between neighboring J=1 molecules cause orientational ordering in bulk hydrogen. For $X > 0.53$ there is a first-order transition at a temperature $T_c(X)$, where the orientational ordering drives a structural transition from hcp into a cubic lattice with a Pa3 structure. In the cubic lattice, where the J=1 molecules are aligned along body-diagonal axes in the four sublattices, the free energy of the ordered state is lower than in the hcp lattice.[1]

This phase transition has been studied for many years by various methods[1] including specific heat experiments.[2,3] X-ray diffraction,[4] pressure,[5] and ultrasonic measurements[6,7] near the transition show a temperature hysteresis of the order of 0.2 Kelvin. These experiments demonstrate the presence of a martensitic transformation, where isolated islands of one crystalline phase with well-established axial directions grow

inside the other phase. This transformation has been investigated with X-ray,[4] Raman scattering,[8] and NMR experiments.[9]

For $X > 0.53$ the transition temperature $T_c(X)$ is best defined by the sharp change in the slope of the entropy curve S(T) or of the pressure curve P(T) at constant density.[5] This choice of $T_c(X)$ corresponds to the high temperature side of the narrow C(T) peak. For $X < 0.53$ the crystal remains in the hcp phase[10] and the anisotropic interaction leads to short-range orientational ordering of the J=1 molecules. The fluctuation rate of the hindered rotational motion slows with decreasing temperature. The J=1 quadrupolar system freezes at low enough temperatures into a "quadrupolar glass" state,[11] but without a well-defined transition.[12] The specific heat resulting from the orientational ordering process is then a broad Schottky-like anomaly. For $X < 0.1$, the heat capacity can be described by a sum of Schottky terms resulting from the interactions between isolated J=1 pairs and triangles. For $X < 0.01$, the Debye contribution dominates the heat capacity at temperatures above 0.5 K.[13] A phase diagram showing the regions of orientational order and disorder is shown in References 12 and 14.

3.1.2 Ortho-Para Conversion

At room temperature, the ortho-para distribution in the hydrogen gas is essentially in the high temperature limit, with $X = 0.75$, and is called *normal-hydrogen* (n-H_2). When the H_2 is cooled to liquid helium temperatures, there is a slow conversion from J=1 to J=0 in pure bulk H_2 caused by intermolecular nuclear dipolar interactions, with a rate given by

$$dX/dt = -k X^2. \tag{3.1}$$

where k = 1.85%/hour.[1]

There is some controversy about the conversion rate of J=1 molecules on a noble metal surface. Avouris and coworkers reported an extremely rapid conversion of the approximately first four H_2 layers adsorbed on Ag(111) and evaporated silver surfaces.[14] This is much faster than the bulk rate described by Equation 3.1 and two orders of magnitude faster than that reported for H_2/Cu(100).[15] It has been proposed[15] that the fast rate on the (111) surface is due to a mechanism involving electron-hole creation, which is possible because of the prominent (111) electronic surface state which extends far from the metal surface.

3.1.3 Quench-Condensed Hydrogen

Recently, there has been renewed interest in solid hydrogen because of evidence that the molecules close to the surface remain mobile at temperatures well below 10 K, where classical diffusion in the bulk is no longer activated. Leiderer and coworkers[16-18] have quench-condensed H_2 films up to several hundred Å thick on a silver surface at 1.5 K. They have used surface-plasmon and light scattering techniques to deduce that the initially amorphous films reorganize to form isolated crystallites when the substrate is heated above 2.5 K, indicating a high surface mobility. These crystallites are thought to be resting on top of a few layers of H_2 which are more tightly bound to the substrate. This reorganization, which is irreversible, results because solid H_2 does not wet silver at these temperatures,[19] and the condensed film is initially in a non-equilibrium state. Classen and coworkers observed an irreversible change in the acoustic

properties of H_2 films condensed at 1.4 K on gold upon annealing the sample above 2.5 K.[20] From their measurements, they deduced an activation energy for surface self-diffusion of 23 K for H_2, which compares with an activation energy of 190 K in bulk H_2.[1] These annealing effects are not strongly influenced by the presence of the ortho and para molecules, since a similar effect was seen in HD.

3.1.4 Our Experiment

In this chapter we present measurements of the specific heat C(T,X) of H_2 films which have been quench-condensed with initial X = 0.75 on a gold-coated quartz substrate held at temperatures varying between 1.0 K and 3.5 K. Since the substrate serves as both an AC calorimeter and a microbalance, the heat capacity per particle is directly calculated from the simultaneous measurement of heat capacity and coverage. The experiments were performed at temperatures between 0.4 and 3.0 K, and we studied J=1 concentrations X between 0.28 and 0.75. The film coverage varied from 0.4 to 92.3 $Å^{-2}$, corresponding to the equivalent of 4 and 923 molecular layers. Our results demonstrate that heat capacity measurements are a useful probe of the ordering behavior and hence of the film structures and of their changes upon annealing.

This chapter is organized as follows: In Section 3.2, we briefly describe the experimental details which are particular to the hydrogen experiment. In Section 3.3, we present our results for thick films, which include specific heat curves C(T,X) for various condensation temperatures, a description of the effect of annealing, a calculation of the sublimation energy for the quench-condensed film, measurements of the J=1 to J=0 conversion rate, phase

transition curves $T_c(X)$ for the quench-condensed films, and a description of the search for thermal hysteresis. In Section 3.4 we propose a model for the variety of ordering behaviors observed. In Section 3.5 we show measurements for much thinner films and discuss the coverage dependence of the ordering behavior. Section 3.6 is a summary.

3.2 Experimental Procedures

The general procedure for evaporating the gold film, condensing an adsorbed film, and making heat capacity measurements has been discussed in Chapter 2. Here we mention procedures which are specific to the quench-condensed hydrogen experiment.

3.2.1 Calorimeter/Microbalance

The calorimeter/microbalance for the hydrogen experiment was constructed from an SC-cut quartz single crystal,[21] 0.65 cm in diameter and 250 μm thick, with the fundamental resonance at 7.2 MHz. The SC-cut, rather than an AT-cut, was chosen in an attempt to avoid stress-induced oscillator frequency shifts, which make the thickness measurement more difficult. This is discussed in more detail in Section 3.5. A H_2 coverage of 0.1 $Å^{-2}$, which corresponds to monolayer completion on graphite,[22] results in a frequency shift of -0.35 Hz while we can distinguish frequency shifts of ~0.03 Hz.

3.2.2 Comment on AC Technique

The AC heat capacity technique is superior to either the adiabatic or time constant method for measuring the heat capacity of solid hydrogen,

because the measurements are not affected by the slow release of thermal energy into the system which results from the conversion of the J=1 molecules. Most early solid hydrogen heat capacity experiments were made using the adiabatic method, and interpretation was complicated by the conversion issue. Phelps[23] was the first to use the AC method to study solid hydrogen.

3.2.3 Preparation of the H_2 Film

After a fresh gold film has been evaporated as described in Chapter 2, the calorimeter is ready for H_2 condensation. The temperature of the effusion line was regulated at 80 K during the dosing of the adsorbate. It was found that when the cell was held below 30 K, a significant fraction of the molecules converted from the J=1 to the J=0 state in the effusion line, as shown by the observation of a peak in C(T) at relatively low temperature immediately after condensation of the film. The conversion was evidently catalyzed by the 304 stainless steel, which is considered not to be ferromagnetic. The effusion line is sufficiently thermally isolated so that its heating did not affect the performance of the ^{3}He refrigerator or the temperatures of the rest of the vacuum chamber. Cold copper shielding minimized the heating of the calorimeter by electromagnetic radiation during effusion. Even so, the minimum temperature of the calorimeter rose to above 0.5 K during this time.

We regulated the calorimeter at the desired temperature between 1.0 and 3.5 K while we allowed H_2 gas to flow through the line and effuse onto the calorimeter. The heat capacity and coverage were monitored throughout the dose. Tests showed the heat capacity of the adsorbate not to be sensitive

to the condensation rate, which was varied between 0.02 and 0.4 $Å^{-2}sec^{-1}$. After the dose was complete, the effusion cell heater was turned off and the effusion cell cooled back to 3 K. Except where noted below, the calorimeter was allowed to cool below 0.4 K and the temperature was scanned to measure C(T).

3.3 Results for Thick Films

3.3.1 The Specific Heat C(T)

In Figure 3.1a, we plot the heat capacity per molecule as a function of temperature for n-H_2 coverages of 80.5, 82.0, 68.5, 77.0, 77.2, and 88.7 $Å^{-2}$ which were quench-condensed on the substrate held at T_{cond} = 3.5, 2.8, 2.0, 1.75, 1.5, and 1.0 K, respectively. After the condensation was completed, C(T) was measured beginning at the lowest temperature. The scans took 60 minutes each. In the T_{cond} = 3.5 K data set, there is a peak in C(T) near 1.75 K which is 0.4 K wide at half maximum. Below the peak, C(T) rises slowly with T. Above the peak, C(T) falls more sharply to a "knee" at T = 1.9 K. Above this temperature, C(T) is flat and featureless up to 3.0 K. When T_{cond} is decreased to 2.8 K, the height of the peak decreases and the temperature of the "knee" increases to 1.95 K. In the T_{cond} = 2.0 K set, the peak height is further reduced and slightly shifted to higher temperature, and a small plateau above the peak is observed. When the condensation temperature is further decreased to 1.75 K, 1.5 K, and 1.0 K, the peak near 1.7 K disappears, and the plateau becomes an increasingly larger peak with a sharp drop to a "knee" at T = 2.7 K.

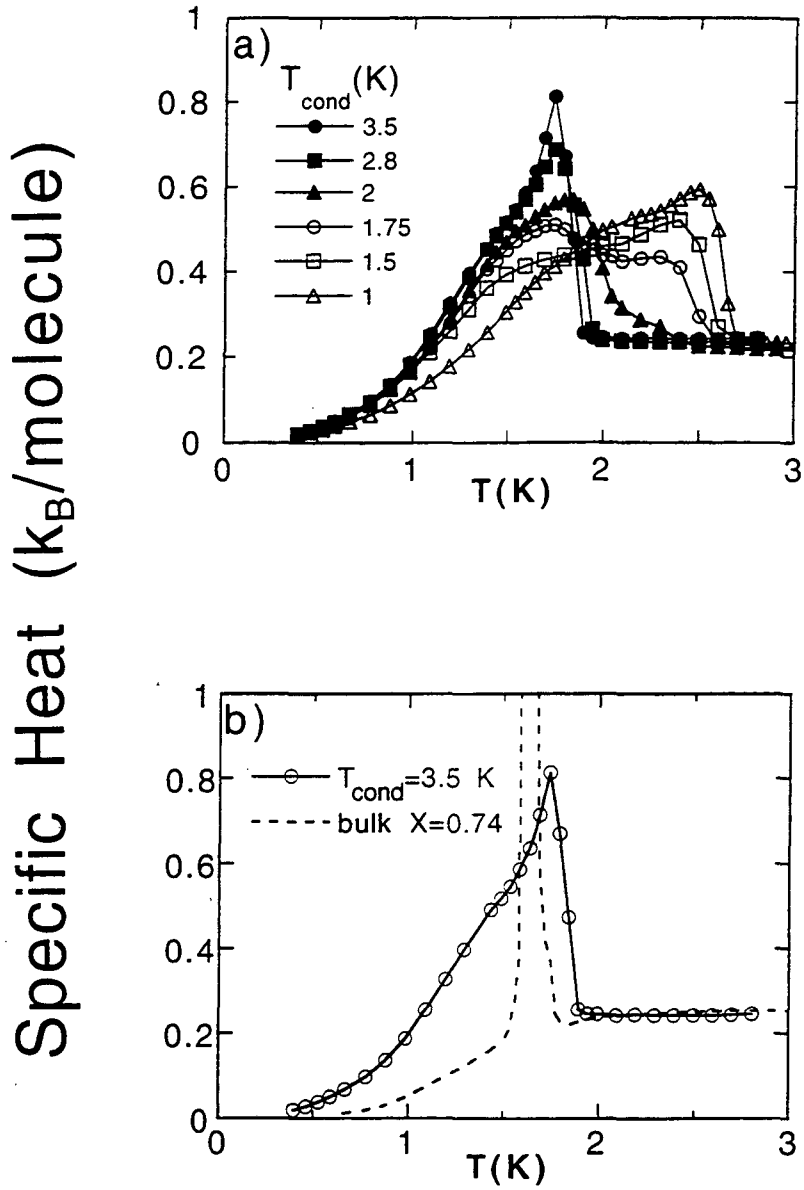

Figure 3.1 Heat capacity per molecule of n-H_2 as a function of temperature. a) Coverages of 80.5, 82.0, 68.5, 77.0, 77.2,and 88.7 Å^{-2} quench-condensed on gold at 3.5, 2.8, 2.0, 1.75, 1.5, and 1.0 K respectively. b) Open circles show the T_{cond} = 3.5 K data set from Figure 3.1a. The dashed curve combines measurements of C(T) for bulk well-annealed H_2 with X= 0.74 near the peak[3] with scaled $(\partial P/\partial T)_V$ data[5] for X=0.71 away from the peak.

It is instructive to compare the quench-condensed data with those for the bulk hydrogen solid. In Figure 3.1b, we replot the T_{cond} = 3.5 K data set from Figure 3.1a in open circles. The dashed line combines bulk data from two sources: C(T) near the peak[3] for X=0.74 from calorimetric data, and $(\partial P/\partial T)_V$ data[5] below and above the peak for X=0.71, converted to C(T) via the relation given in Reference 5 and appropriately scaled to take into account the difference in X.

The peak in the quench-condensed data set occurs at a temperature close to the peak in the bulk data; however, the quench-condensed peak is considerably broader than the bulk peak, and the temperature at which the heat capacity begins to rise with decreasing T in the quench-condensed H_2 is approximately 0.15 K higher than the bulk T_c. The proximity of the experimental peak in Figure 3.1b to the ordering temperature in the bulk data suggests that the peak is associated with bulk-like orientational ordering of the J=1 molecules in the quench-condensed H_2. Because H_2 shows triple-point wetting on gold, the equilibrium state of H_2 condensed on gold at 3.5 K should be bulk crystallites on top of one or two monolayers of adsorbate.[19] The shift in T_c has been seen in an earlier experiment[23] and cannot be described as a simple statistical broadening of the bulk peak. Below the maximum there is a much larger difference between our experimental points and the bulk: the quench-condensed H_2 films have an excess heat capacity which is similar to the contribution observed[2,5,24] in well-annealed H_2 for X < 0.53, when short-range interactions are important but long-range ordering is not possible.

For the films condensed at lower temperatures, we expect the structure to be a homogeneous, possibly amorphous, non-equilibrium

state.[17,18] The J=1 molecules in the T_{cond} = 1.5 K and 1.0 K films are also subject to orientational ordering, but it is clear from the shape of the C(T) curves in Figure 3.1a that the ordering is not bulk-like. C(T) has a maximum at 2.5 K for T_{cond} = 1.0 K. Below the maximum, C(T) decreases approximately linearly with decreasing temperature. On the high temperature side of the feature, C(T) decreases by a factor of three within 0.2 K. This feature must be a signature of a long range order-disorder transition, as it is too sharp to be expressed as a sum of Schottky terms. We note that the transition temperature for ordering in the bulk increases with density,[3] and a change from 1.7 to 2.7 K would correspond to a density increase of ~26%, which is produced by a pressure of ~1 kbar.

The double-humped structure seen in C(T) for T_{cond} = 1.75 K, and to a lesser extent for T_{cond} = 1.5 and 2.0 K, possibly reflects the coexistence of two quench-condensed phases. This two-phase model of the films is supported, but not proved, by the near intersection of all of the heat capacity curves in Figure 3.1a at a unique temperature, 1.85 K: Let $C_1(T)$ and $C_2(T)$ be the heat capacities of states 1 and 2. These could be the T_{cond} = 1.0 K and T_{cond} = 3.5 K states, but not necessarily so. If the heat capacity of the mixture of the states can be described by

$$C(T) = x\,C_1(T) + (1-x)\,C_2(T), \quad 0 < x < 1 \tag{3.2}$$

and there is a T_0 such that $C_1(T_0) = C_2(T_0)$, then clearly $C(T_0) = C_1(T_0) = C_2(T_0)$ for all values of x.

We can also compare the behavior of the quench-condensed film with bulk H_2 by examining the temperature dependence of the entropy. For

normalization purposes, we compute the *reduced entropy* s(T) = $S/(N X k_B \ln 3)$, where N is the total number of molecules. The contribution to the entropy is $k_B \ln 3$ for each J=1 molecule at high temperatures, ~20 K, when there is free rotation, but where higher rotational states have not yet become populated. The J=0 molecules contribute no entropy because they are in singlet states. We neglect the Debye contribution to the entropy, because at 3.0 K it is less than $0.002k_B$ per molecule. In Figure 3.2 we plot the reduced entropy s(T) for the films quench-condensed at 3.5 K, 1.75 K, and 1.0 K compared with s(T) for bulk H_2 with X=0.74 and X=0.65,[12] which undergo ordering transitions, and X=0.33,[25] which does not. The X=0.74 curve has been obtained from integration of the data sets[2,3,5] mentioned previously. For all values of X, s(T) for the bulk approaches unity at T > 10 K. As in the bulk X=0.74 sample, the s(T) curve for T_{cond} = 3.5 K has a kink near 1.7 K, the signature of the sharp heat capacity peak. The features seen in C(T) in the other two films result in less prominent kinks in s(T) at higher temperatures. We obtain s(3.0 K) for all three quench-condensed films to be higher by the order of 10% than in the bulk. As for the bulk X=0.33 sample, s(T) in the quench-condensed samples remains appreciable below 1.0 K, which suggests that a fraction of the molecules are subject to short-range forces at temperatures well below the ordering peaks. It has been previously observed that for samples with X<0.6 the magnitude of the short-range interactions is sensitive to the details of H_2 preparation. For H_2 grown on iron alum crystals[2] and also bulk H_2,[5] the Schottky anomaly is broad with a maximum in C(T) at approximately 1.5 K. H_2 grown on sintered copper

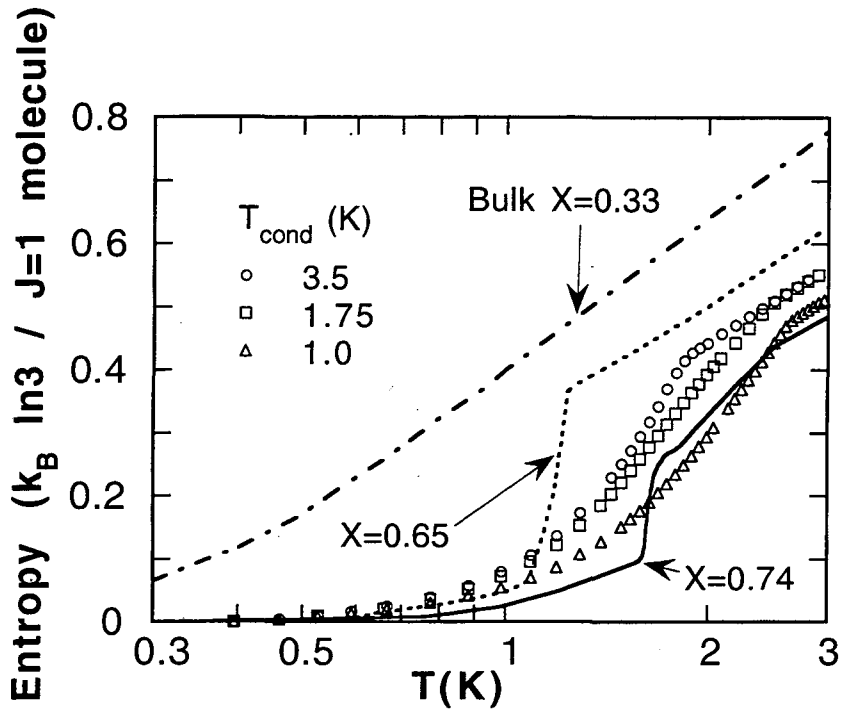

Figure 3.2 Reduced entropy (in units of $k_B$ln3) per ortho-H_2 molecule as a function of temperature for the T_{cond} = 3.5 K, 1.75 K, and 1.0 K films shown in Figure 3.1a. The curves are the reduced entropy for bulk H_2 with X=0.74[2,3,5] and 0.65,[12] which undergo ordering transitions, and X=0.33,[26] which does not.

sponge (100 μm nominal diameter) shows an additional heat capacity peak near 0.5 K.[24]

Although the differences in C(T) between the bulk and the quench-condensed films suggest that the latter exhibit different degrees of orientational disorder, there does not appear to be an additional entropy in the quench-condensed films measured at 3.0 K. We note that the lattice T^3 contribution to C(T) is negligible for our samples compared with that from orientational ordering. This contrasts with quench-condensed films of heavier elements, where the molecules behave classically and C(T) of the well-annealed crystal solid is well described by a Debye T^3 term. Steinmetz and coworkers, for example, found that the specific heat of ~1 μm thick quench-condensed Xe films was more than twice as large as that of bulk Xe for $T < 3$ K.[26] The additional heat capacity was proportional to T^2 from 1 to 4 K and was well described by surface phonon modes[27] of a solid with a packing fraction of ~64%. Upon annealing the films to 50 K and recooling, they found that the excess heat capacity disappeared. The contribution to the heat capacity for H_2 predicted by the surface phonon model[27] is much smaller than the ~k_B/molecule resulting from the lifting of the degeneracy of the J=1 molecules. Using Lennard-Jones parameters of ε=36.7 K and σ=2.96 Å,[28] we calculate a contribution to the heat capacity of ~10^{-4} k_B per molecule at 2.8 K.

3.3.2 Effect of Annealing on C(T) of T_{cond} = 1.5 K Film

As we mentioned in Section 3.1, H_2 films condensed at $T \leq 1.5$ K on silver are believed to be in a non-equilibrium state and have been observed to undergo irreversible structural changes upon annealing at temperatures

above 2.5 K. In Figure 3.3a we show a series of three scans of C(T) for a film with coverage 92.3 $Å^{-2}$ and initial X = 0.75 quench-condensed at 1.5 K. The first scan was begun five minutes after the completion of condensation. The second and third were begun two and four hours later. Each scan took roughly an hour. Between the end of the first and the beginning of the second scan, the film temperature was kept below 0.4 K. Between the second and third the film was held at 3.0 K. Comparing the three curves we see that the feature in C(T) corresponding to the bulk-like ordering transition became slightly more prominent as the time after condensation increased. However, the difference in shape between the second and third scan is no more dramatic than that between the first and second, suggesting that one hour of annealing at 3.0 K does not result in a structural reorganization that is significantly reflected in C(T). The overall shift of the curves to lower temperatures for longer time is the result of the J=1 to J=0 conversion, which will be discussed later in this section.

In Figure 3.3b we show two scans of C(T) for a film with initial coverage 71.1 $Å^{-2}$ quench-condensed at 1.5 K. The first scan was begun five minutes after the completion of condensation; the second was begun two hours later. Between the end of the first scan and the beginning of the second, the film was held at 3.4 K for one hour. This annealing resulted in two effects. First, the shape of C(T) changed dramatically between the first and second scans. The high temperature feature became smaller, and the bulk-like ordering peak emerged as the dominant feature in C(T). Second, significant desorption took place. We measured a desorption rate of 9.0 ± 0.8 $Å^{-2}$/hour at 3.4 K. The error is estimated by comparing two nominally identical measurements.

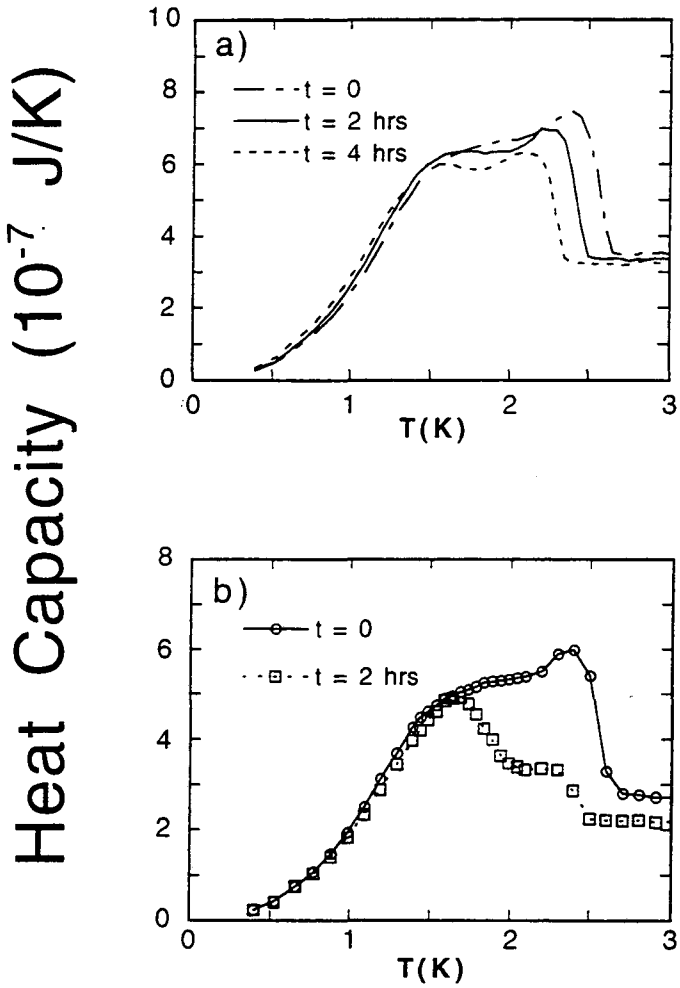

Figure 3.3 a) Three heat capacity scans of a H_2 film with coverage 92.3 $Å^{-2}$ and initial X=0.75 quench-condensed at 1.5 K. The first C(T) scan (one hour duration) was begun immediately after condensation, the second scan two hours after condensation, and the third scan four hours after condensation. During the hour between the end of the first and beginning of the second scan, the film was kept below 0.4 K. Between the end of the second and beginning of the third scan, the film was annealed for one hour at 3.0 K. b) Two heat capacity scans of a H_2 film with initial coverage 71.1 $Å^{-2}$ and initial X=0.75 quench-condensed at 1.5 K. The first scan was begun immediately after condensation; the second was begun two hours later. Between the end of the first and beginning of the second scan, the film was annealed for one hour at 3.4 K.

From the desorption rate and a measurement of the sticking coefficient, we calculate the sublimation energy for quench-condensed hydrogen. We have measured the sticking coefficient α for quench-condensed films to be roughly unity and independent of substrate temperature. The accuracy of the measurement is limited by uncertainty in the total amount of hydrogen sprayed on the substrate. The holes in the effusion cell are actually short tubes with diameters equal to their lengths, and we assume that hydrogen molecules scatter diffusely off the sides of the tubes. Govers and coworkers reported a value for α of 0.8 for hydrogen condensed at 3 K.[29] Close to equilibrium the desorption rate dn/dt can be expressed as

$$\frac{dn}{dt} = \frac{\alpha}{\sqrt{2\pi m k_B T}} (P_{film} - P_{vap}) \tag{3.3}$$

where P_{film} is the equilibrium vapor pressure of the film at temperature T and P_{vap} is the actual pressure.[30] We assume P_{vap} is zero because most surfaces in the system are at temperatures below 2 K, since they are in good thermal contact with the pumped ^{4}He bath. We calculate P_{film} from Equation 3.3 for T = 3.4 K, which we can then relate to the sublimation energy E by equating the chemical potential of the bound solid to that of an ideal gas[31] above it:

$$E = k_B T \left[\ln\left(\frac{P_{film}}{T^{2.5}}\right) - 4.03 \right] \tag{3.4}$$

where P_{film} is in units of Torr. We obtain a value of E = -98.6 ± 1.5 K, which agrees with another measurement of the sublimation energy for quench-condensed H_2 (-90 ± 10 K).[20]

3.3.3 J=1 to J=0 Conversion Rate

At pressures below 0.5 kbar, the conversion of a J=1 molecule into the J=0 state is a two-phonon process. At higher pressures, as the width of the phonon frequency spectrum increases, single phonon emission leads to a higher conversion rate.[32-34] In quench-condensed H_2 we might expect the conversion rate to be different from that in the bulk because of possible differences in density, in the number of nearest neighbors, and thus in the phonon spectrum. We have measured the rate of conversion of J=1 molecules to J=0 in the quench-condensed films by monitoring the heat released during conversion.

To measure this quantity we regulated the calorimeter at 0.34 K and observed the decrease in regulation power after H_2 condensation. This measurement required careful analysis, because the power due to conversion in our films was ~1 nW, while the total regulation power depended sensitively (~1 nW / mK) on the ^{3}He cold stage temperature, which has been observed to drift by several mK during data acquisition. For films condensed at several temperatures we measured the regulation power versus cold stage temperature before and after condensation, and finally after desorption of the H_2 condensate. All three measurements were done within an hour, and from them we computed a conversion rate for X=0.74. We could not easily measure the dependence of the conversion rate on time, and hence X, because longer experimentation times introduced systematic

errors. In Figure 3.4 we show a summary of our results by plotting the normalized power due to conversion as a function of condensation temperature. The data are shown by the solid circles, and the error bars reflect both statistical and systematic errors. Since the conversion rate appears to be independent of condensation temperature, we also plot a dashed line which shows the best fit of the points to the relation

$$W = H\,(dX/dt) \tag{3.5}$$

where H is the energy in the sample liberated by the conversion (170.5 k_B per molecule) and dX/dt is given by Equation 3.1, with X = 0.74. The fit yields a value of k = 1.8 ± 0.2%/hour. This rate is consistent with the bulk value of k = 1.85 ± 0.1%/hour, which is an average of several published values.[5,32,35]

3.3.4 Dependence of Thermal Properties and T_c on X

To demonstrate the dependence of orientational ordering on X, we show in Figures 3.5a, 3.5b, and 3.5c the time evolution of C(T) for H_2 films with initial X = 0.75 condensed at 3.5 K, 2.8 K, and 1.5 K respectively. After condensation of each H_2 film, C(T) was measured eleven times over 50+ hours. For the 2.8 K film, three additional scans were made extending the monitoring time to 114 hours. For clarity, we represent the data as alternating solid and dashed lines. The experimental scatter was comparable to that shown in Figure 3.1. The scans were always made with increasing temperature. It took five minutes to cool the sample from 2.8 K to 0.4 K between successive scans. The average sample age and the corresponding X for each scan are listed in the figure captions. Measurements were limited

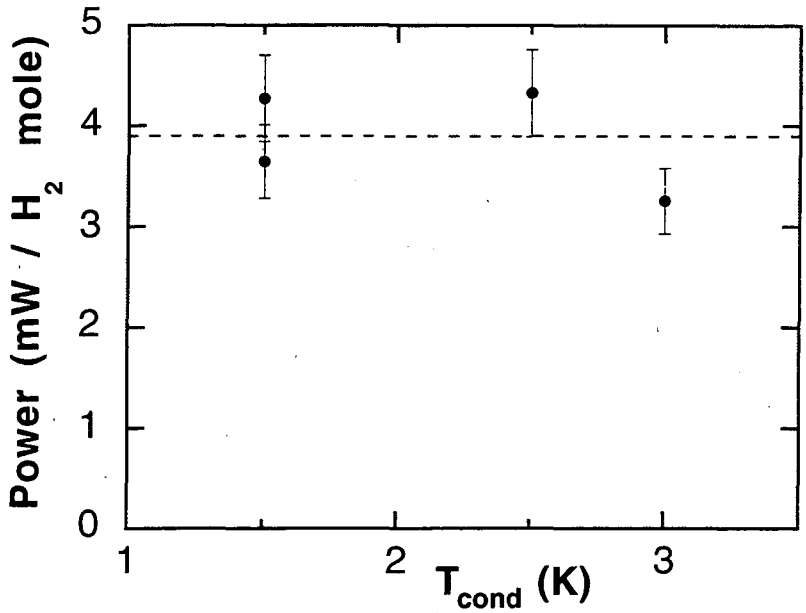

Figure 3.4 Ortho-para conversion experiment. Solid circles show normalized conversion power for film coverages of 89.4, 84.0, 91.7, and 83.2 $Å^{-2}$ condensed at 1.5, 1.5, 2.5, and 3.0 K respectively. Dashed line is best fit to data and corresponds to $k = 1.8 \pm 0.2$ %/hour.

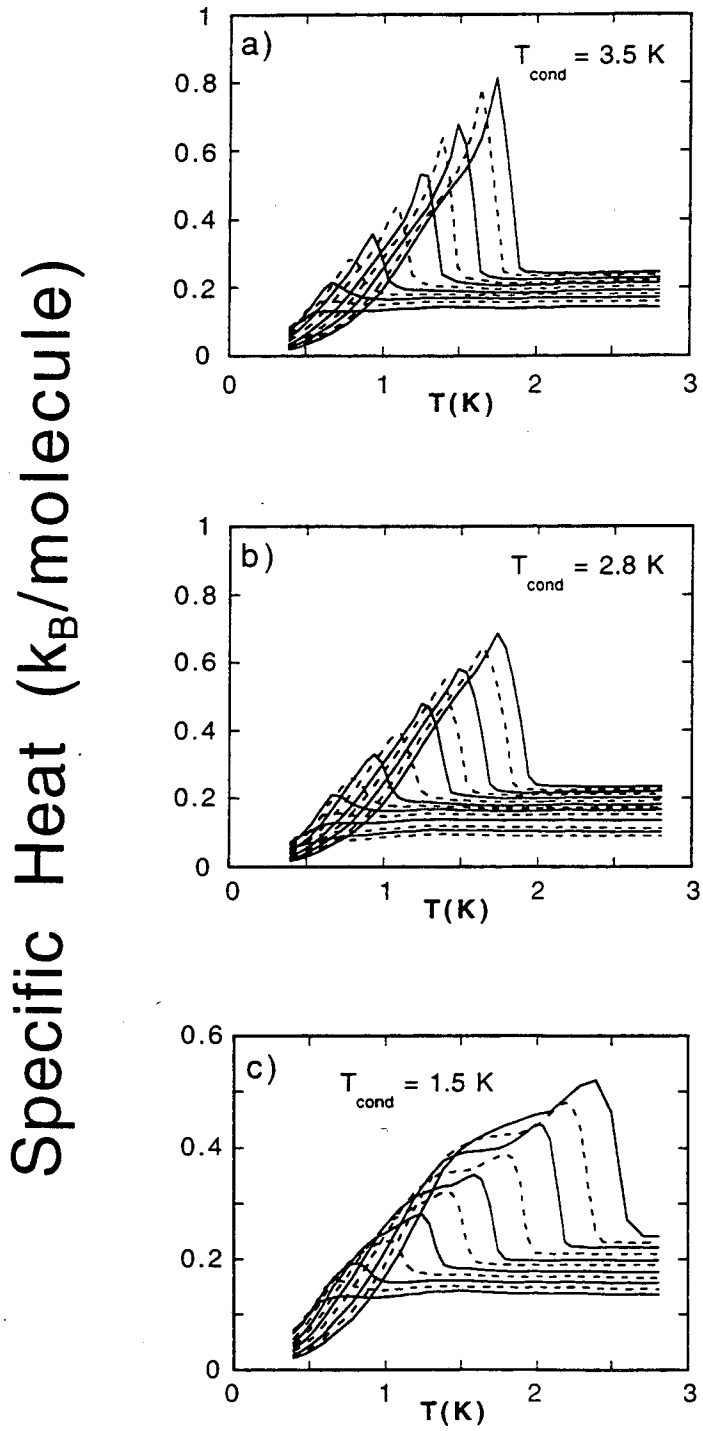
Specific Heat (k_B/molecule)
a)
T_{cond} = 3.5 K
b)
T_{cond} = 2.8 K
c)
T_{cond} = 1.5 K
T(K)
0
0.2
0.4
0.6
0.8
1
2
3

Figure 3.5 a) Heat capacity as a function of temperature measured eleven times over a fifty-three hour period for a H_2 coverage of 80.5 $Å^{-2}$ with initial X=0.75 quench-condensed at 3.5 K. The first scan, which is shown as a solid line, was made 0.5 hours after condensation. Scans two through eleven are shown as alternating dashed and solid lines and were measured 2.5, 5.5, 8.5, 11.5, 16.6, 21.5, 26.5, 32.5, 40.6, and 53.0 hours after condensation. The times correspond to X = 0.74, 0.72, 0.70, 0.67, 0.64, 0.61, 0.57, 0.54, 0.51, 0.48, 0.43 when k=1.9%/hour in Equation 3.1.

b) C(T) for a H_2 coverage of 82.0 $Å^{-2}$ with initial X=0.75 quench-condensed at 2.8 K. The scans were measured 0.5, 2.5, 5.5, 8.5, 11.6, 16.6, 21.6, 26.6, 32.5, 41.1, 52.1, 72.3, 92.1, and 114.7 hours after condensation which correspond to X = 0.74, 0.72, 0.70, 0.67, 0.64, 0.61, 0.57, 0.54, 0.51, 0.47, 0.43, 0.37, 0.32, and 0.28 when k=1.9%/hour in Equation 3.1.

c) C(T) for a H_2 coverage of 77.2 $Å^{-2}$ with initial X=0.75 quench-condensed at 1.5 K. The scans were measured 0.6, 3.6, 6.6, 10.6, 14.6, 18.6, 23.6, 29.6, 35.8, 42.8, and 50.9 hours after condensation which correspond to X = 0.74, 0.71, 0.69, 0.65, 0.62, 0.59, 0.56, 0.53, 0.50, 0.47, and 0.43 when k=1.9%/hour in Equation 3.1.

to T < 2.8 K to insure that desorption would be insignificant. The molecular coverage was monitored with the microbalance, and no evidence of desorption was seen during the runs. Since the hold time of the ^{3}He refrigerator is only 14 hours, we thermally recycled the refrigerator several times during the measurement. During this operation, the temperature of the ^{3}He refrigerator cold stage remained below 2.6 K.

The curves in Figures 3.5a and 3.5b evolved in very similar fashion: as the time after condensation increased, the bulk-like peak became smaller and moved to lower temperature, and the heat capacity in the flat region above the peak decreased. The shape of the initial 1.5 K C(T) scan shown in Figure 3.5c is very different than those shown in Figures 3.5a and 3.5b. After ~40 hours, however, all three curves evolved into very similar shapes. This time coincided with the disappearance of the bulk-like peak in Figures 3.5a and 3.5b. This is shown in Figures 3.6a and 3.6b where we replot scans nine through eleven from Figures 3.5a and 3.5c for the films quench-condensed at 3.5 and 1.5 K. For comparison, we plot scaled $(\partial P/\partial T)_V$ measurements[36] in Figure 3.6a. Since no significant annealing of any of the films took place, we believe that the structure of each of the films at t = 40 hours was very similar to the initial structure immediately after condensation. Thus we conclude that these differences in structure have little effect on C(T) for X small enough that no long-range ordering is possible. The heat capacity for these values of X is expected to reflect short-range interactions within clusters of J=1 molecules, however, and hence C(T) should be sensitive to structure on molecular length scales. Thus, we conclude that the structure of the films on short length scale is not sensitive to details of the sample preparation. In Figures 3.7a and 3.7b we plot the entropy of these same scans and see that the

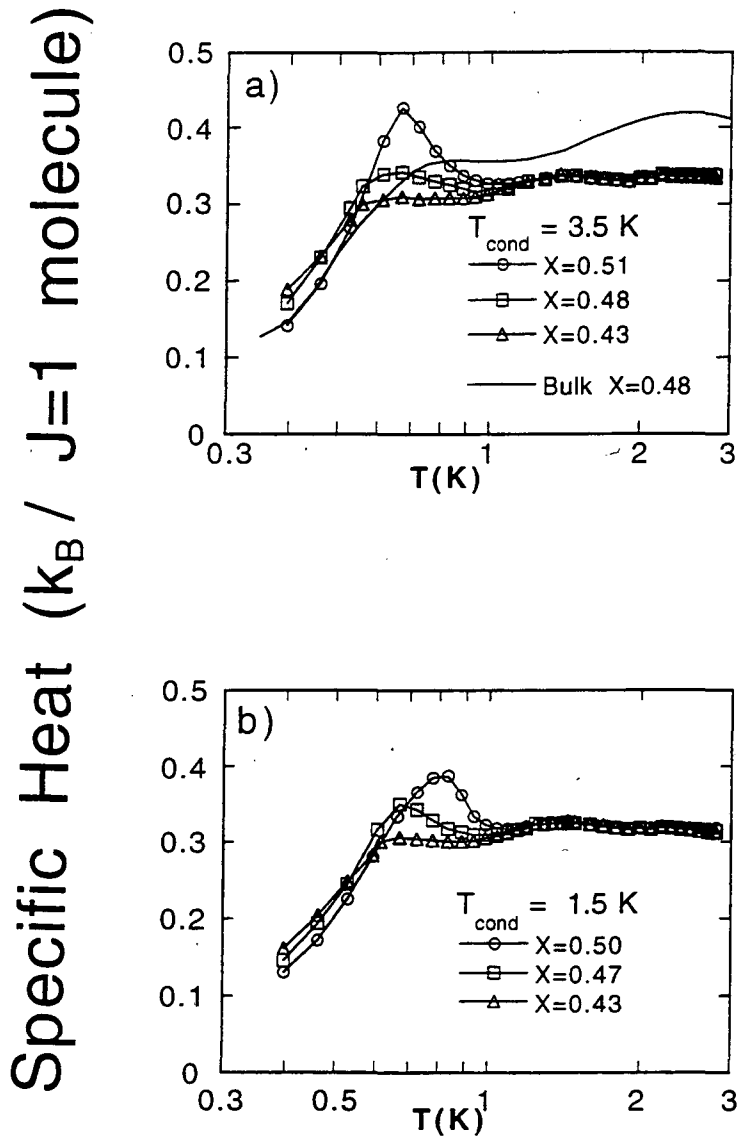

Figure 3.6 a) Expanded view of scans 9, 10, and 11 in Figure 3.5a, corresponding to T_{cond} = 3.5 K and X = 0.51, 0.48, and 0.43. Bulk C(T) for X=0.48 computed from $(\partial P/\partial T)_V$ data.[37] b) Expanded view of scans 9, 10, and 11 in Figure 3.5c, corresponding to T_{cond} = 1.5 K and X = 0.50, 0.47, and 0.43.

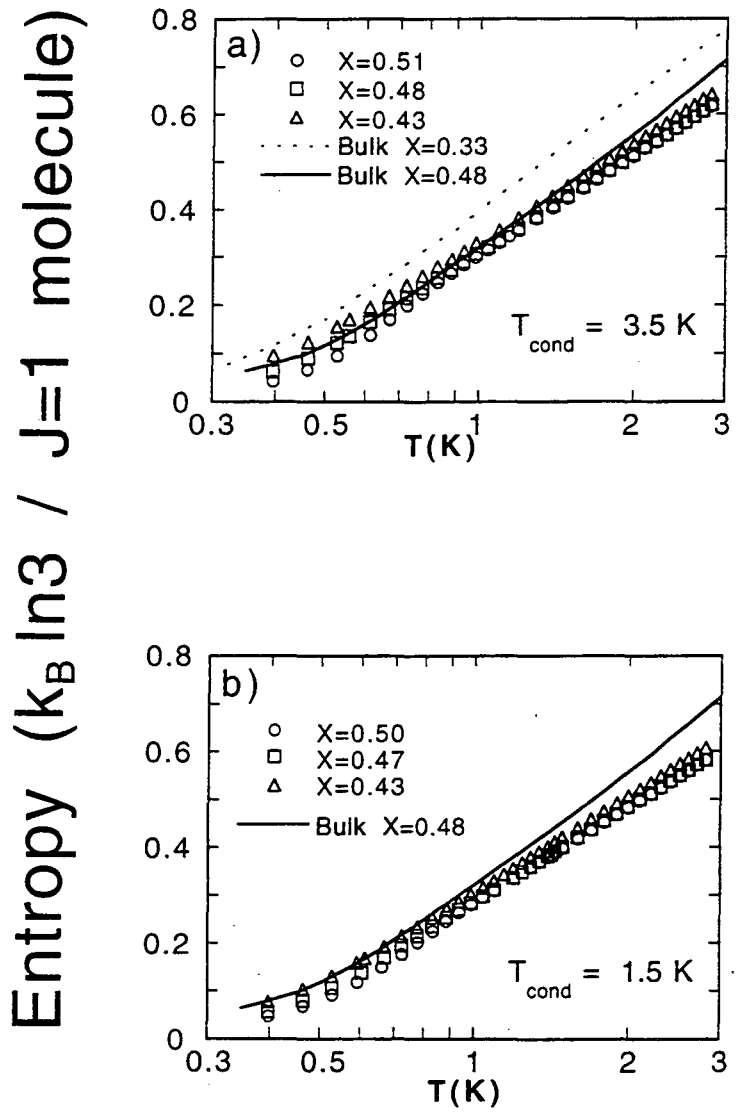

Figure 3.7 a) Reduced entropy for scans 9, 10, and 11 in Figure 3.5a, corresponding to T_{cond} = 3.5 K and X = 0.51, 0.48, and 0.43. Bulk measurements for X=0.48 and X=0.33 computed from $(\partial P/\partial T)_V$ data.[26,37] b) Reduced entropy for scans 9, 10, and 11 in Figure 3.5c, corresponding to T_{cond} = 1.5 K and X = 0.50, 0.47, and 0.43.

magnitude and temperature dependence of s(T) are in fairly good agreement with the bulk result[36] for X=0.48.

In Figure 3.8 we plot the temperature $T_c(X)$ for orientational ordering in our films quench-condensed at 3.5, 2.8, and 1.5 K and for bulk H_2.[5,7] For the 3.5 K and 2.8 K films T_c refers to a bulk-like transition. We have identified the "knee" in C(T) as T_c and have used the value of k = 1.9 ± 0.1%/hour to determine X and the corresponding error bars. We only plot T_c as determined by this method for X > 0.55. At lower values of X, we see a small peak in C(T) near 0.6 K, but we do not believe it is associated with an ordering transition, because a similar bump[36] has been seen in the bulk for X=0.49, where long-range ordering does not take place. For the 1.5 K film, T_c similarly refers to the "knee" above the ordering feature.

3.3.5 Thermal Hysteresis

In Figure 3.9 we show the results of repeated scans of C(T) near the peak for a H_2 coverage of 81.2 $Å^{-2}$ and initial X = 0.75 quench-condensed at 2.8 K. Scans with T decreasing from 2.1 K to 1.6 K, shown as solid lines, were alternated with scans with T increasing from 1.6 K to 2.1 K, shown as dashed lines. The hydrogen was condensed with the calorimeter held at 2.8 K, after which the temperature of the substrate was immediately reduced to 2.1 K. The first temperature scan began at 2.1 K and ended at 1.6 K. The following one began at 1.6 K and ended at 2.1 K. We repeated this cycle three times. Each scan took approximately nine minutes and the scans were begun ten minutes apart. As in Figure 3.5b, the peak is seen to decrease in height and move to lower temperatures. There is no evidence of the hysteresis that has

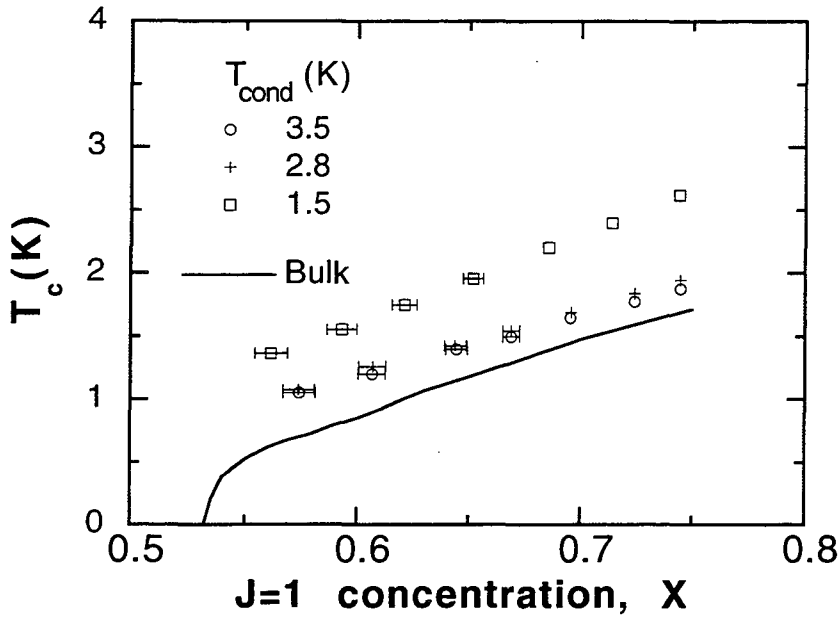

Figure 3.8 $T_c(X)$ plotted versus X for scans shown in Figure 3.5a-c and for bulk hydrogen.[5,7] The values of X and error bars for the films are obtained from Equation 3.1 with k=1.9 ± 0.1%/hour.

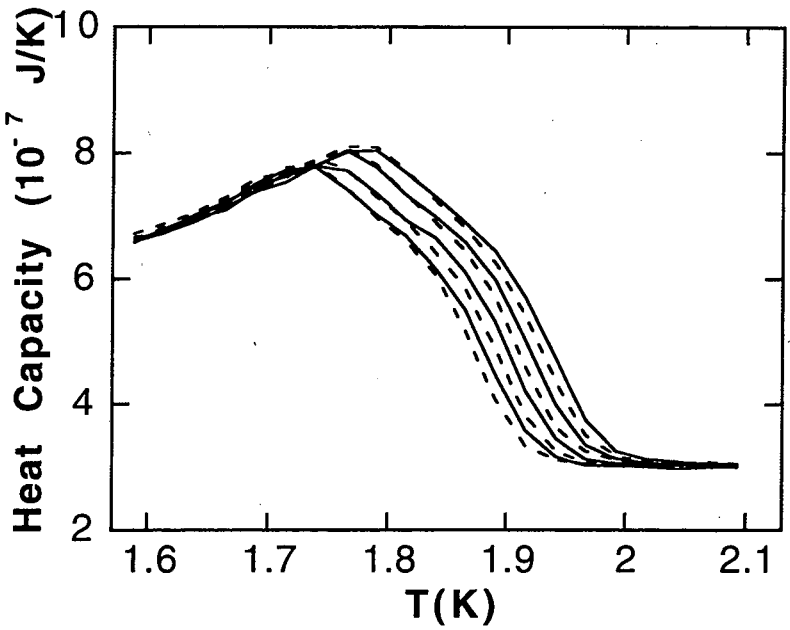

Figure 3.9 Rapid scans of heat capacity as a function of temperature in the vicinity of the peak for a n-H_2 sample with coverage of 81.2 $Å^{-2}$ quench-condensed at 2.8 K. The first scan was measured ten minutes after condensation. It began at 2.1 K and ended at 1.6 K and is shown as the rightmost solid curve. The next scan began at 1.6 K and ended at 2.1 K. This is the rightmost dashed curve. This down/up process was repeated three more times. Each scan was begun ten minutes apart.

been seen in the annealed bulk. The small difference in shape between the solid and dashed curves is the result of the continuous conversion of J=1 to J=0 molecules during each of the scans. We have made similar measurements on films condensed at 1.5 K and 3.5 K which also show no hysteresis.

In bulk H_2, the orientational ordering of the J=1 molecules for $X > 0.53$ is expected to be a first-order transition regardless of the crystalline structure above the transition,[37] and the cubic form is the stable one in the ordered phase. The absence of hysteresis in Figure 3.9 indicates that the transition in our quench-condensed H_2 for $T_{cond} = 2.8$ K is not martensitic and thus the high temperature, disordered phase of the solid is likely to be also fcc. We note that diffraction studies have shown that the disordered phase of solid hydrogen grown from vapor is fcc.[38] Solid D_2 powder grown by injecting D_2 gas into liquid helium at 4.2 K also is fcc.[39]

3.4 Model and Discussion

The observations described in Section 3.3 have led us to form the following picture of the film, which complements that obtained from experiments by other investigators: Calorimetric measurements on films quench-condensed at $T_{cond} < 2$ K show that the contribution to the entropy from the orientational disordering is spread over a larger temperature range than in bulk H_2. This indicates that the density is not uniform throughout the sample, and that there is a distribution $\Delta\rho$ around an average density $\langle\rho\rangle$ with an fairly sharp cut-off about 25% above $\langle\rho\rangle$. This is implied by the sharp drop of the specific heat anomaly near 2.7 K for X=0.74 and might qualitatively explain the observed shape of C(T) for $T_{cond} < 2$ K. As T_{cond} is

increased above ~2.5 K and surface mobility gradually becomes activated, the film tends to form an equilibrium configuration of crystallites positioned on top of a few layers of H_2. The density distribution is narrowed and the sharp peak characteristic of bulk samples appears. Because the transition peak is not as sharp as in the bulk and T_c is shifted, the characteristics of a bulk sample grown from the melt are not completely recovered, even for samples annealed at 3.0 K, or for samples with T_{cond} = 3.5 K. Finite-size effects, some structural disorder, strains, and dislocations in the small crystallites might well remain that broaden the peak and are responsible for the short-range rotational contributions to C(T) well below the transition.

It is interesting that in spite of the suggested broad density distribution in samples formed for $T_{cond} < 2$ K, the ortho-para conversion rate is the same within the experimental error as for the bulk sample at zero pressure. From measurements at elevated densities in bulk samples it has been shown that for a density ~25% higher than at zero pressure, the conversion rate is doubled, with k ~ 4%/hour.[32-34] Hence there must be some averaging of the conversion rate over the density distribution in the film or another mechanism that causes this conversion rate to be the same as in bulk samples. It is also difficult to reconcile a broad density distribution with the measurements of heat capacity for X < 0.5 shown in Figures 3.6a and 3.6b which suggest that the film structure on short length scales, and hence density, might not depend on T_{cond}.

3.5 Results for Thinner Films

In sections 3.3 and 3.4 we considered films tens of angstroms thick--thick enough that we should expect no coverage dependence in the specific

heat. We observed a rich variety of ordering behaviors in Section 3.3, but we concluded that the differences seen in the heat capacity of the various films with respect to that of the bulk crystal and to each other were the result of structural differences in the films and not due to their being thin. In this section we consider films as thin as four layers. As the film thickness is reduced, we would expect to observe significantly different ordering behavior than in the thick quench-condensed films. When a system is small enough, the finite size of the system becomes important--energy fluctuations can broaden and shift a bulk first-order phase transition.[40-44] This sort of description has been successfully used to describe the rounding of the heat capacity melting peak for oxygen physisorbed on small graphite domains.[45] For sufficiently thin films, a three dimensional description of the ordering is no longer appropriate. Two-dimensional orientational ordering has been observed in hydrogen monolayers with high o-H_2 concentration adsorbed to graphite. Graphite has a very well-defined lattice, and the hydrogen monolayer forms a $\sqrt{3}$ by $\sqrt{3}$ structure commensurate with the carbon atoms. Kubik and coworkers[46] used NMR to observe ordering of a complete monolayer into a "pinwheel" phase at 0.6 K for X=0.9. For X=0.77 the transition temperature drops to 0.33 K.

3.5.1 Experimental Complication--Stress Sensitivity

Our measurement of low (<10 layers) H_2 coverages has been complicated by the sensitivity of the microbalance to stress by the condensed layers. The spurious frequency shift limits the accuracy of the coverage measurement. This effect has previously been seen[47] in N_2 layers on silver. As discussed in Chapter 2, a shift of the quartz microbalance resonance does

not necessarily imply an adsorbed mass. In Figure 3.10 we plot the heat capacity and microbalance response for the first few condensed layers. Seconds after we open the valve to allow hydrogen gas down the effusion line, the heat capacity of the detector begins to increase, indicating that hydrogen is sticking to the calorimeter. However, the microbalance resonance initially shifts a few Hz in the wrong direction before turning around after an estimated ten layers have condensed. We believe that the initial shift does not reflect mass leaving the surface of the microbalance, but results from a tangential stress on the electrode. A derivation of this shift requires a careful treatment[48,49] of the elastic properties of the system considering second and third order terms. The resulting frequency shift is complicated, as illustrated by the fact that the sign of the frequency shift depends on the cut of the quartz. Two of the most common commerically available quartz crystals are the AT and BT-cuts, which have computed stress constants of -2.75×10^{-12} cm^2/dyne and $+2.65 \times 10^{-12}$ cm^2/dyne, respectively, for stress tangential to the crystal surface.[49] The frequency shift is equal to the stress constant times a geometrical factor. The magnitude of the stress in a Si film resulting from ^{84}Kr ion implantation has been measured using the computed stress sensitivity of quartz oscillators and has been found to be in excellent agreement with an independent measurement of the stress using a standard technique.[49]

In our experiments we have constructed detectors from both the AT and the SC (stress-compensated) cuts, the latter being an orientation which is far less sensitive to tangential stress. Even using the latter crystal, however, we have not been able to eliminate the effect seen in Figure 3.10. This leads us to conclude that either the stress caused by the adsorbed layer is not purely

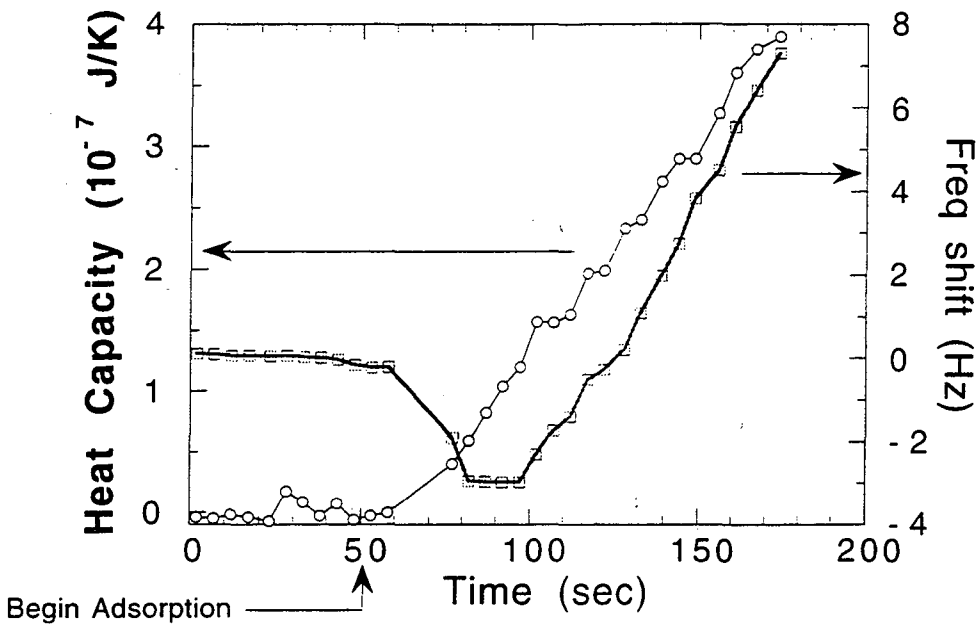

Figure 3.10: Stress effect in microbalance measurement. Immediately after condensation, the microbalance resonance shifts the "wrong" way, the result of the adsorbate's stressing of the substrate. On this plot, a positive frequency shift is defined as one consistent with additional mass coupling to the device.

tangential, but also has a component in the "thin" direction of the substrate, or that this is not the correct explanation for the effect. We also have observed that the Q of the crystal is reduced by 10-40% by the presence of the condensed hydrogen film. This large change in the resistance R in the equivalent circuit of the microbalance could be related to the shift in the resonance.

The result of this interesting, but poorly understood, effect is uncertainty in the coverage, which becomes relatively larger as the coverage is reduced. To deduce the coverages for low exposures, we assume that the sticking coefficient is independent of coverage and compare the exposure of small doses to big doses, where the stress induced shift is much smaller that that due to mass coupling and where we know the coverage with very little relative uncertainty. The assumption of constant sticking coefficient is reasonable: Govers and coworkers[29] found that the sticking coefficient for molecular hydrogen incident on a water-covered Si bolometer reached its asymptotic value of 0.8 after completing just 2.5 layers. Using our exposure comparison analysis, we expect to have an uncertainty of approximately one layer.

3.5.2 Results

In Figure 3.11 we plot the heat capacity of eight n-H_2 films condensed at 2.8 K on gold. The coverages range between approximately 0.4 and 82.0 $Å^{-2}$, the equivalent of between 4 and 820 layers. The y-axis is plotted logarithmically to facillitate comparison. There is some variation in the peak height and shape even for the thickest films, which suggests that the details of the preparation are important. This is clearer in Figure 3.12 where

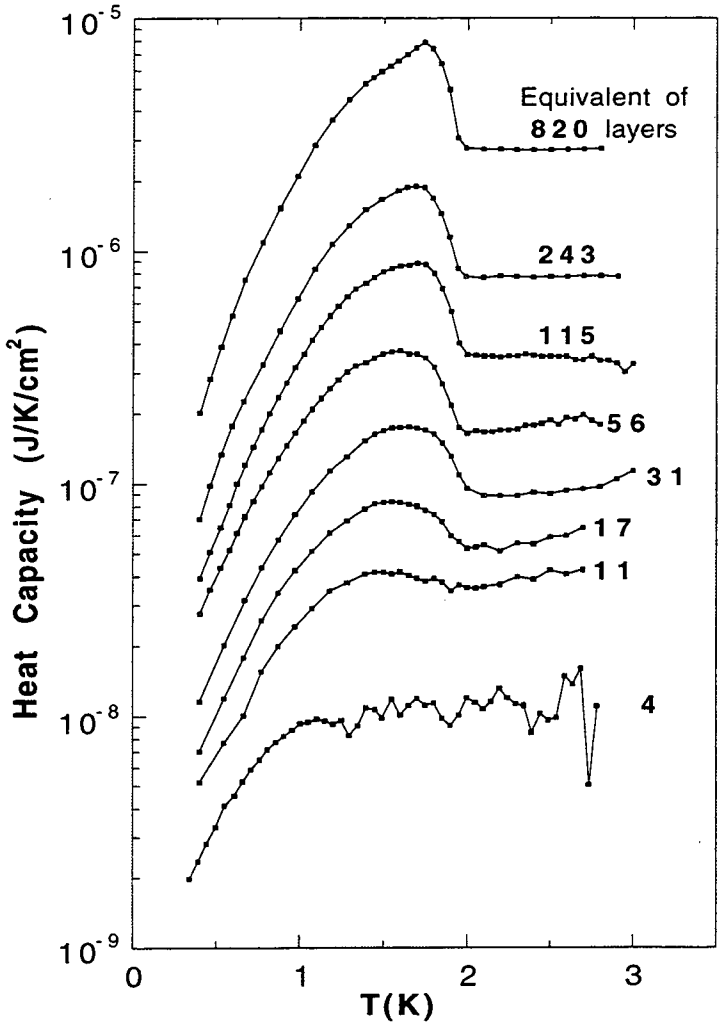

Figure 3.11: Coverage dependence of heat capacity of n-H_2. One "layer equivalent" is taken to be 0.1 $Å^{-2}$. Uncertainty in coverage of approximately one layer because of "stress effect" shown if Figure 3.10 and discussed in text.

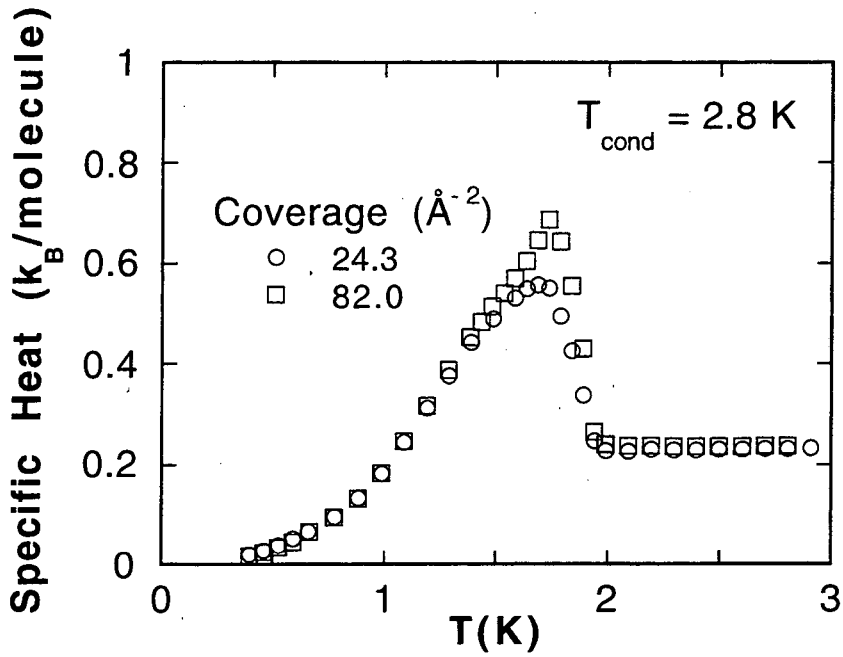

Figure 3.12 Heat capacity per molecule as a function of temperature for n-H_2 coverages of 82.0 and 24.3 Å^{-2} quench-condensed on gold at 2.8 K.

we replot the specific heat of the two largest coverages from Figure 3.11. The ordering peak in Figure 3.11 becomes noticeably smaller when the coverage is reduced to the equivalent of twenty layers and finally disappears for coverages below about four layers. No new features appear in the lowest coverage films.

3.5.3 Discussion

Phelps and coworkers have investigated the coverage dependence of the heat capacity peak in films thought to be between 3 and 25 layers thick condensed on sapphire.[23] They reported a bulk-like ordering transition which broadened with decreased coverage but which was present in even their thinnest films. Their hydrogen/gold results were not conclusive. Less bulk-like behavior was seen than on the sapphire, and reproducibility was a problem, indicating that the substrate had a major effect on the adsorbate behavior.

In our films there seem to be several sources of the coverage-dependence of the heat capacity. From computation of the entropies of the films, it appears that there is a reduced concentration of J=1 molecules in the thinnest films, probably the result of conversion catalyzed on the faces of gold (111) crystallites. In Table 3.1 we list the entropy per molecule for each of the eight films shown in Figure 3.11, as well as the thickness of the region which has been converted at the metal surface. We have computed this last quantity by comparing the entropies at 2.5 K of the thin films to the average of those of the three thickest films. We have made the assumption that the entropy per J=1 molecule above the ordering transition is independent of coverage, and attributed the missing entropy in the thin films to conversion.

Coverage (layers)	Entropy (2.5 K) (k_B/molecule)	Converted Layers
820	0.42	---
243	0.39	---
115	0.41	---
56	0.40	---
31	0.34	4.5
17	0.33	2.9
11	0.29	2.9
4	0.26	1.4

Table 3.1 Thin Film Conversion Data

We conclude that conversion is catalyzed in the first two to four molecular layers in agreement with the results[14] for H_2/Ag(111) and H_2/evaporated Ag.

A thin layer of p-H_2 close to the surface should not affect the ordering of J=1 molecules many lattice constants away and hence does not explain the coverage-dependence of the shape of the heat capacity peak seen in Figure 3.11. In Table 3.2 the change in shape of the heat capacity peak is quantified.

Film	Coverage (layers)	n-H_2 Coverage (est. layers)	T_{peak} (K)	T_{knee} (K)
1	820	817	1.74	1.96
2	243	240	1.69	1.96
3	115	112	1.70	1.96
4	56	53	1.58	1.97
5	31	27	1.65	2.02
6	17	14	1.55	2.00
7	11	8	1.5	2.00
8	4	2	----	----

Table 3.2 Coverage Dependence of Ordering Peak

The columns are as follows: the measured coverage, the estimated coverage of unconverted n-H_2, the temperature where the heat capacity is maximum, and the temperature of the "knee" above the peak. We previously identified the "knee" as best describing the temperature where the ordering transition takes place. As the coverage is reduced, the temperature of the peak is reduced, but the temperature of the "knee" remains relatively unchanged. It is difficult to say whether the peak is broadened as the coverage is reduced, because it disappears in to the much bigger background heat capacity. The disappearing peak indicates the growing importance of short-range interactions as the coverage is reduced.

The unknown microscopic structure of the crystallites makes it difficult to rigorously analyze the results of Figure 3.11 and Table 3.2. It is possible that the finite-size energy fluctuations mentioned above play a role

in the broadening of the peak, but as Phelps pointed out,[23] this effect is probably small compared to those associated with the heterogeneities of the substrate and in the adsorbed film. An imporant role also must be played by the large surface/volume ratio of the crystallites in the thinner films. In a film with nominal thickness of ten layers, one would expect to find crystallites containing approximately a thousand molecules, almost half of which would be surface atoms, containing fewer nearest neighbors than those in a bulk crystallite and perhaps having different ordering behavior.

3.6 Summary

Calorimetric measurements on H_2 films quench-condensed on gold at different temperatures T_{cond} have been reported. We have investigated how orientational ordering and the order-disorder transition in the films depend both on T_{cond} and on the annealing of the film above the onset temperature of surface diffusion. The specific heat for films as a function of ortho concentration X has been measured. We have observed how the ordering transition depends on film thickness. Our main observations and conclusions are as follows:

1) Two different types of orientational ordering for n-H_2 (X=0.74) have been observed. For films condensed at $T \geq 2.5$ K there is a peak in C(T) at 1.75 K which resembles the bulk ordering peak but is shifted to higher temperature by approximately 0.15 K. There is a large heat capacity excess compared with the bulk below the ordering peak, which may result from short-range ordering due to size effects. For films condensed at $T \leq 1.5$ K a different orientational ordering takes place. There is no peak near 1.75 K, but rather a broad maximum with a sharp drop near T = 2.7 K. For films

condensed at 1.75 K and 2.0 K there are two bumps in C(T), which is evidence that both types of ordering are taking place.

2) The entropies for all the samples with X=0.74 at T = 3.0 K, above the long-range order-disorder transition, are comparable regardless of T_{cond}. They are also comparable with that for bulk H_2. This indicates that the observed specific heat solely reflects orientational ordering of the J=1 molecules, without a contribution from structural changes or other mechanisms.

3) As X decreases through ortho-para conversion, the locations of the peaks or maxima in C(T) of the samples shift to lower temperatures, just as in bulk H_2. The order-disorder transition curves $T_c(X)$ for the various films have been obtained and run approximately parallel to that for bulk H_2.

4.) For X<0.5, when long-range ordering is excluded, C(T) is not sensitive to T_{cond} and hence to film structure.

5.) The annealing of films with T_{cond} = 1.5 K for one hour at 3.4 K has two effects. There is a change in the shape of C(T) which is consistent with the reorganization of some of the molecules into a structure similar to that obtained for higher condensation temperatures. There is also significant desorption. From the desorption rate we calculate a sublimation energy of -98.6 ± 1.5 K, which is consistent with measurements by others.

6.) For the films with thickness equivalent to hundreds of layers, the J=1 to J=0 conversion rate is comparable to that in bulk H_2 independent of condensation temperature. There is evidence of fast conversion of the first two or three layers of J=1 molecules at the gold surface.

7.) Because there is no thermal hysteresis in the heat capacity, the high temperature disordered phase of the hydrogen is likely to be fcc, but

only direct determination by X-ray diffraction will be able to confirm this assertion.

The different shapes of C(T) that are determined by T_{cond} have led to the speculation that for the thick non-equilibrium films formed at $T_{cond} < 2$ K, the density of the sample is not uniform, but varies by about 20% about the average density. When the equilibrium crystallites are formed with $T_{cond} > 2.5$ K or by annealing at $T > 3$ K, the density distribution is considerably narrowed, and the final density is close to that of bulk H_2 formed at zero pressure. In spite of this speculated density distribution, the ortho-para conversion rate is the same for all the thick samples and comparable to that of bulk H_2 at zero pressure. As the coverage is reduced, the ordering peak becomes smaller relative to the background heat capacity, indicating that short-range interactions become increasingly more important.

References

1. I.F. Silvera, Rev. Mod. Phys. **52**, 393 (1980).

2. R.W. Hill and B.W.A. Ricketson, Philos. Mag. **45**, 277 (1954).

3. G. Ahlers and W.M. Orttung, Phys. Rev. **133**, 1642 (1964).

4. A.F. Schuch, R.L. Mills and D.A. Depatie, Phys. Rev. **165**, 1032 (1968).

5. J.F. Jarvis, H. Meyer and D. Ramm, Phys. Rev. **178**, 1461 (1969).

6. R. Wanner, H. Meyer and R.L. Mills, J. Low Temp. Phys. **13**, 337 (1973).

7. R. Banke, M. Calkins and H. Meyer, J. Low Temp. Phys. **61**, 193 (1985).

8. W.N. Hardy, I.F. Silvera and J.P. McTague, Phys. Rev. **B12**, 753 (1975).

9. A.B. Harris, S. Washburn and H. Meyer, J. Low Temp. Phys. **50**, 151 (1983).

10. J.V. Gates, P.R. Ganfors, B.A. Fraas and R.O. Simmons, Phys. Rev. **B19**, 3667 (1974).

11. N.S. Sullivan, M. Devoret, B.P. Cowan and C. Urbina, Phys. Rev. B **17**, 5016 (1978).

12. A.B. Harris and H. Meyer, Can. J. Phys. **63**, 3 (1985).

13. R.J. Roberts and J.G. Daunt, Phys. Lett. **33A**, 353 (1970).

14. P. Avouris, D. Schmeisser and J.E. Demuth, Phys. Rev. Lett. **48**, 199 (1982).

15. E. Ilisca, Phys. Rev. Lett. **66**, 667 (1991).

16. P. Leiderer and U. Albrecht, J. Low. Temp. Phys. **89**, 229 (1992).

17. U. Albrecht, P. Evers and P. Leiderer, Surface Science **283**, 419 (1993).

18. R.N.J. Conradt, U. Albrecht, S. Herminghaus and P. Leiderer, Physica B **194-196**, 679 (1994).

19. A.D. Migone, A. Hofmann, J.G. Dash and O.E. Vilches, Phys. Rev. B **37**, 5440 (1988).

20. J. Classen, K. Eschenröder and G. Weiss, Annalen der Physik **4**, 1 (1995).

21. Quartzdyne, Inc., Salt Lake City, UT 84123.

22. G.J. Kellogg, P.E. Sokol, S.K. Sinha and D.L. Price, Phys. Rev. B **42**, 7725 (1990).

23. R.B. Phelps, J.T. Birmingham and P.L. Richards, J. Low Temp. Phys. **92**, 107 (1993).

24. D. Haase, L.R. Perrell and A.M. Saleh, J. Low Temp. Phys. **55**, 283 (1984).

25. H. Meyer and S. Washburn, J. Low. Temp. Phys. **57**, 31 (1984).

26. N. Steinmetz, H. Menges, J. Dutzi, H.V. Lohneysen and W. Goldacker, Phys. Rev. B **39**, 2838 (1989).

27. R.E. Allen and F.W. De Wette, Phys. Rev. **179**, 873 (1969).

28. J. Van Krankendonk, Solid Hydrogen, (Plenum Press, New York, 1983) p. 45.

29. T.R. Govers, L. Mattera and G. Scoles, J. Chem. Phys. **72**, 5446 (1980).

30. M. Weimer and D.L. Goodstein, Phys. Rev. Lett. **50**, 193 (1983).

31. C. Kittel and H. Kroemer, Thermal Physics , (W. H. Freeman and Co., New York, 1980) p. 162.

32. G. Ahlers, J. Chem. Phys. **40**, 3123 (1964).

33. P. Pedroni, H. Meyer, F. Weinhaus and D. Haase, Solid State Commun. **14**, 279 (1974).

34. A.J. Berlinsky, Phys. Rev. B **12**, 1482 (1975).

35. F. Schmidt, Phys. Rev. B. **10**, 4480 (1974).

36. D. Ramm, H. Meyer and R.L. Mills, Phys. Rev. B **1**, 2763 (1970).

37. J.R. Cullen, D. Mukamel, S. Shtrikman, L.C. Levitt and E. Callen, Solid State Commun. **10**, 195 (1972).

38. A.E. Curzon and A.J. Mascall, Brit. J. Appl. Phys. **16**, 1301 (1965).

39. R.L. Mills, J.L. Yarnell and A.F. Schuch, 1972, *Low Temperature Physics Conference 13*, (Plenum, New York), II, p. 202.

40. Y. Imry, Phys. Rev. B **21**, 2042 (1980).

41. M.S.S. Challa, D.P. Landau and K. Binder, Phys. Rev. B **34**, 1841 (1986).

42. M.E. Fisher and A.N. Berker, Phys. Rev. B **26**, 2507 (1982).

43. H. Shechter, J. Suzanne and J.G. Dash, Phys. Rev. Lett. **37**, 706 (1976).

44. P. Sheng, R.W. Cohen and J.R. Schrieffer, J. Phys. C: Solid State Phys. **14**, L565 (1981).

45. R. Marx, Phys. Rev. B **40**, 2585 (1989).

46. P.R. Kubik, W.N. Hardy and H. Glattli, Can. J. Phys. **63**, 605 (1985).

47. V. Panella and J. Krim, Phys. Rev. E **49**, 4179 (1994).

48. R.N. Thurston and K. Brugger, Phys. Rev. **133**, A1604 (1963).

49. E.P. Eernisse, J. Appl. Phys. **43**, 1330 (1972).

4. Heat Capacity of Helium Monolayers Adsorbed on Evaporated Gold

4.1 Introduction

Interest in two-dimensional thermodynamics and critical behavior has motivated many studies of the heat capacity of physisorbed helium monolayers. As discussed in Chapter 1, the adsorbate-substrate interaction can play an important role in determining the adsorbate phase diagram. For both ^{3}He and ^{4}He adsorbed on very heterogeneous surfaces, including sintered copper sponge,[1-3] noble gas-plated copper,[4,5] and porous Vycor glass,[6] the adsorbate forms two-dimensional islands in the most tightly binding regions and cannot be described in terms of homogenous two-dimensional (2D) phases. In this case, the heat capacity consists of a pseudo-Debye T^2 contribution from the heat capacity of the islands and a contribution which is associated with excitations of single ^{4}He atoms out of the islands.

4.1.1 ^{4}He/Graphite and ^{3}He/Graphite

On smoother surfaces, the adsorbate-substrate interaction can be ignored, at least at low coverages. Fractions of a monolayer of ^{4}He adsorbed on graphite have been studied[7] for many years; a recently proposed[8] phase diagram is shown in Figure 4.1. Monolayer completion on graphite occurs at a coverage of approximately 0.12 Å^{-2}, when atoms are observed to be promoted to the second layer. For coverages below ~0.04 Å^{-2} the film exists as a classical 2D gas at temperatures above a few Kelvin, with heat capacity k_B/molecule.[9,10] This is part of the "fluid" region in Figure 4.1. As the

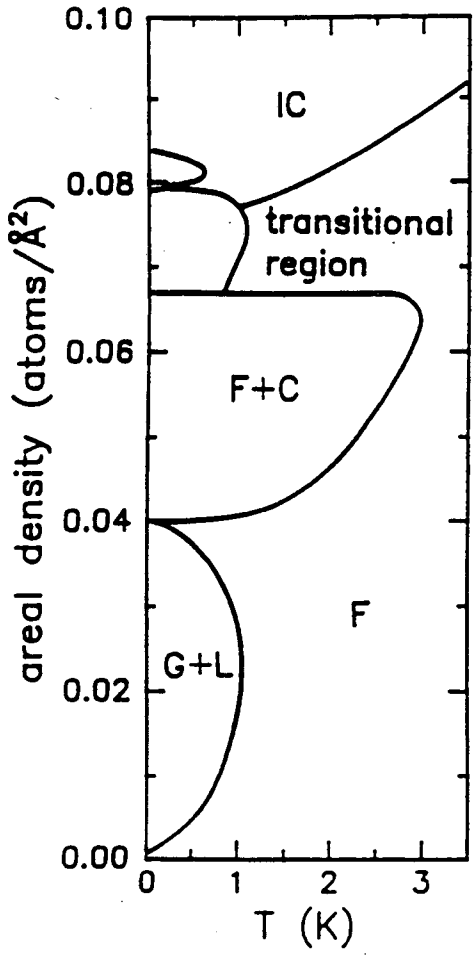

Figure 4.1 Proposed[8] phase diagram for ^{4}He adsorbed on graphite. G: Gas. L: Liquid. F: Fluid. C: Commensurate solid. IC: Incommensurate Solid.

temperature is reduced the heat capacity rises to a small peak near 1 K and falls as T^2 below the bump. Originally this rounded maximum was described by a quantum mechanical second virial coefficient expansion to the ideal gas law appropriate for bosons.[11] However, this treatment predicted a continued upturn in the heat capacity for lower temperatures, which was not seen experimentally.

More recently the bump has been interpreted as a signature of a phase transition from a region of gas and liquid coexistence below the peak to a gas above, and as an indication of a Kosterlitz-Thouless superfluid transition.[8] The first interpretation is supported by the observation that the peak position changes very little with coverage and by calculations[12,13] that the 2D liquid phase is self-bound with a density of about 0.04 $Å^{-2}$. The second interpretation is prompted by good agreement between experiment and a computation of the heat capacity for a density of 0.0432 $Å^{-2}$ which shows a KT peak.[14] This picture is not completely satisfactory, mainly because at the highest coverages in the G-L region the KT transition should occur at higher temperatures than the phase separation.

At very low coverages below 0.01 $Å^{-2}$, however, the heterogeneity of the substrate is important, when the ^4He is preferentially adsorbed at anomalously tight binding regions of the substrate.[9,10] These might be sites where two basal plane surfaces make contact at a small angle, and the atom is simultaneously adsorbed on both surfaces. The heat capacity in this case has the form of a 2D solid all the way up to 15 K.[10]

At low temperatures and coverages between 0.04 and 0.063 $Å^{-2}$, the ^4He is thought to coexist as a liquid and a $\sqrt{3} \times \sqrt{3}$ solid, commensurate with the underlying lattice and with 1/3 of the graphite adsorption sites covered.

The melting transition of the solid is continuous and consistent with calculations of three-state Potts models, where the melting occurs by motion of the atoms to the adsorption sites not usually occupied by the solid. Below the sharp melting peak the heat capacity can be described as a sum of a constant term(classical gas), a term proportional to T^2 (fluid), and a term proportional to $T^{-2}e^{-\Delta/T}$ term (energy gap.) Between 0.063 $Å^{-2}$, the density where perfect $\sqrt{3} \times \sqrt{3}$ registry occurs, and about 0.08 $Å^{-2}$, the low temperature phase is thought to include a commensurate solid where 2/5 of the adsorption sites are covered by ^{4}He atoms and which melts via a first-order transition, and a commensurate solid where 3/7 of the sites are covered.[15] At higher densities, close to monolayer completion, the adsorbate forms an incommensurate solid which floats on the graphite lattice.[9]

The phase diagram for ^{3}He/graphite is very similar to ^{4}He/graphite for coverages above 0.04 $Å^{-2}$. At low coverages, however, the film is well described as a Fermi fluid at temperatures down to a few mK. Just as for ^{4}He, the heat capacity of the ^{3}He film above a few Kelvin is independent of temperature and has magnitude ~k_B/molecule.[9,16] As the temperature is reduced, the Fermi gas enters the degenerate regime, and the heat capacity becomes proportional to temperature.[17] Below 50 mK, the heat capacity shows anomalous behavior which is attributed to nuclear magnetic interactions. Near 3 mK there may be a phase transition into a new state.[17,18]

4.1.2 ^{4}He/Evaporated Silver

As discussed in the introduction, the weak binding of a metal substrate is predicted to reduce the ^{4}He-^{4}He interaction and thus might be a

promising setting for an investigation of noninteracting bosons at very low temperatures. Kenny and Richards investigated the behavior of ^{4}He monolayers adsorbed on evaporated silver films and saw behavior that was qualitatively different from the low coverage graphite results. They measured the heat capacity between 1.8 and 3.2 K for coverages that were deduced to be between 0.02 and 0.2 Å^{-2}. The results of the investigation are shown in Figure 4.2; the open symbols are the experimental data points. They saw no evidence of tightly binding sites which would localize the adatoms and concluded that the entire ^{4}He coverage was mobile at all temperatures within the accessible range, $1.8 < T < 3.2$ K. For the lower coverages the heat capacity was independent of temperature over the entire range. For the larger coverages, the heat capacity eventually decreased as the temperature decreased. However, there was no evidence of a peak that would be expected for either condensation into a liquid or onto the substrate in a commensurate solid. Since it appeared that neither adsorbate-adsorbate nor adsorbate-substrate interactions were important in this temperature range, they compared their results to the prediction for a 2D noninteracting Bose gas, which is discussed below. The coverage was not directly measurable in this experiment but was deduced from fits of the data to the model.

4.1.3 2D Noninteracting Bose Gas

The energy of the ^{4}He system can be written

$$U(T) = \int_{-\infty}^{\infty} \frac{E\,D(E)\,dE}{e^{\beta(E-\mu)}-1} \quad , \tag{4.1}$$

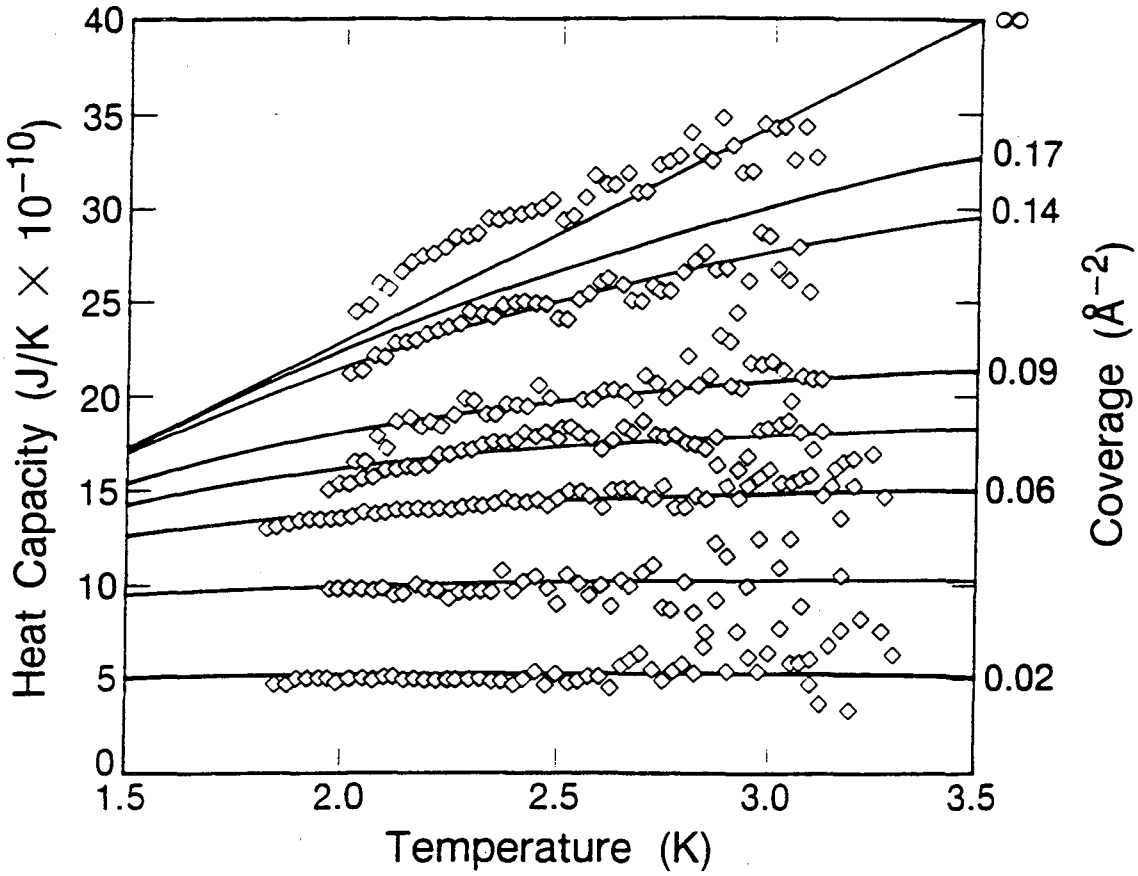

Figure 4.2 Measurements[22] of the temperature dependence of the heat capacity for a series of coverages of ^{4}He adsorbed on an evaporated Ag surface. The solid curves are fits to the heat capacity of a two-dimensional noninteracting Bose gas.

where D(E) is the density of states, μ is the chemical potential, and $\beta = (k_B T)^{-1}$. For noninteracting particles confined to a surface with area A by a potential with bound states E_i normal to the surface, D(E) is given by

$$D(E) = \sum_{i}^{\text{all bound states}} \frac{2\pi m A}{h^2} \Theta(E-E_i) \quad , \tag{4.2}$$

where $\Theta(E-E_i)$ is zero for $E < E_i$ and 1 for $E \geq E_i$. The first excited state for ^4He on Au is calculated[19] to be 2.92 meV, which means that the state should not becomes populated until T > 5 K. Thus only the ground state needs to be considered and Equation 4.1 becomes [20]

$$U(T) = \frac{2\pi m A}{h^2} \int_0^\infty \frac{E\, dE}{e^{\beta(E-\mu)}-1} \quad . \tag{4.3}$$

The chemical potential for a two-dimensional film of bosons bound to a surface is

$$\mu(T) = \mu_{bose}(T) + E_b \quad , \tag{4.4}$$

where $$\mu_{bose}(T) = k_B \ln\left(1-\exp\left(\frac{-Nh^2}{2\pi m A k_B T}\right)\right) \quad . \tag{4.5}$$

The unknown binding energy E_b shifts U(T) by a constant and does not affect the heat capacity. At low temperatures, $\mu_{bose}(T)$ approaches zero, and Equation 4.1 can be evaluated exactly and differentiated to obtain

$$C(T) = \frac{2\pi^3 k_B^2 \, m \, A}{3 \, h^2} T \quad . \tag{4.6}$$

The heat capacity falls below the classical value at low T as more of the particles occupy the ground state. This should not be confused with the Bose condensation that takes place in three dimensions where the ground state is occupied by a significant fraction of the particles upon cooling below the Bose-Einstein condensation temperature. For intermediate temperatures Equation 4.1 can be integrated numerically to determine the heat capacity. The resulting curves were seen to fit the experimental data in Figure 4.2 extremely well at all coverages except the largest.

The results shown in Figure 4.2 were very exciting; however, it was clear that lower temperatures were needed to test the Bose gas assignment, which predicted that the heat capacity of all of the coverages would collapse onto one curve as the temperature was reduced. Moreover, an independent measurement of the coverage was required to confirm that at the highest temperatures, the constant value of the specific heat was in fact k_B/atom, and not some other value.

In Section 4.2 we discuss the experimental procedures which are specific to the helium film experiments. We present heat capacity measurements as a function of coverage for ^{4}He films condensed at 3.0 and 2.4 K in Section 4.3. The heat capacity is compared to the calculation for the noninteracting Bose gas, and binding energies for the first layer are deduced from desorption rates. We also show the heat capacity as a function of temperature for coverages between 0.007 and 0.096 Å^{-2} at temperatures between 0.42 and 2.4 K. In Section 4.4 we compare our data for ^{4}He/gold to

the ^{4}He/graphite and ^{4}He/silver results and construct some pieces of the ^{4}He/gold phase diagram. Section 4.5 summarizes our findings.

4.2 Experimental Procedures

The general procedure for evaporating the gold film, depositing an adsorbed film, and making heat capacity measurements has been discussed in Chapter 2. Here we mention procedures which are specific to the helium monolayer experiment.

4.2.1 Calorimeter/Microbalance

The calorimeter/microbalance for the helium experiment was constructed from an AT-cut quartz single crystal,[21] 1.37 cm in diameter and 275 μm thick, with the fundamental resonance at 6 MHz. A ^{4}He coverage of 0.12 Å^{-2}, which corresponds to monolayer completion on graphite,[8] results in a frequency shift of -0.65 Hz while we can distinguish frequency shifts of ~0.03 Hz.

4.2.2 Preparation of the Substrate and Helium Film

Kenny reported problems with migration of the ^{4}He atoms off the calorimeter when a metallic path existed to the heat sinks.[22] The quartz substrates we use for our detectors were purchased with preexisting gold electrodes evaporated on each side which extend to the edge of the crystal, as shown in Figure 2.1. To prevent the possibility of migration along a metallic path, we evaporated a 0.5" diameter 2000 Å thick SiO film over the preexisting electrode on the side of the device where the adsorbate is condensed. The SiO overlayer was evaporated in a bell jar evacuated below 10^{-7} torr at a rate of 10 Å/sec and appeared transparent and yellowish as

expected.[23] Heat capacity measurements of ^{4}He adsorbed on the SiO-covered calorimeter are shown in Figure 4.3 and confirmed that the ^{4}He was not mobile at temperatures of 3 K or below. Although, the heat capacity was of order ~k_B/atom at 3 K, C(T) was not constant, as expected for a gas, but had a strong temperature dependence, indicating that the adsorbate was in a less mobile state.

For the ^{4}He/gold investigation, we evaporated a fresh gold film *in situ* on top of the SiO disk while the detector was at LHe temperature as described in Chapter 2. The gold film was 2000 Å thick with a diameter of 0.86 cm; thus there was a ~1 mm wide ring of SiO around the gold spot to stop any mobile ^{4}He atoms from leaving the gold surface. During dosing of the adsorbate, we regulated the temperature of the effusion line at 5 K, and films were condensed with the calorimeter held at both 3.0 and 2.4 K. We did not see evidence of migration and concluded that the ^{4}He was confined to the gold-covered area defined by the evaporation mask, which also defined the area exposed during gas adsorption.

4.3 Heat Capacity Measurements of ^{4}He Monolayers

4.3.1 Films Condensed at 3.0 K

In Section 4.1, we saw that the ^{4}He behaves like an ideal 2D gas at 3 K on both graphite and evaporated silver, and so we intially deposited ^{4}He films at this temperature to see if the behavior of the adsorbate on an evaporated gold substrate was similar. In Figure 4.4a we show a measurement of the heat capacity and microbalance frequency shift during deposition of a ^{4}He film at 3.0 K. The room temperature valve was opened at the time indicated by the arrow. The adsorbate took a few seconds to pass

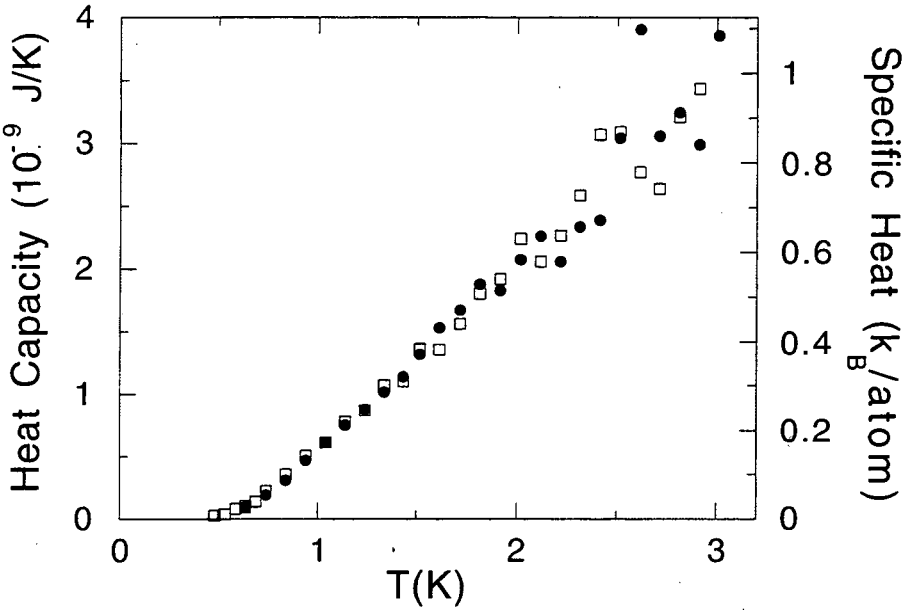

Figure 4.3 Measurements of the temperature dependence of the heat capacity of two nominally identical ^{4}He films with coverage 0.44 Å^{-2} adsorbed on an evaporated SiO surface.

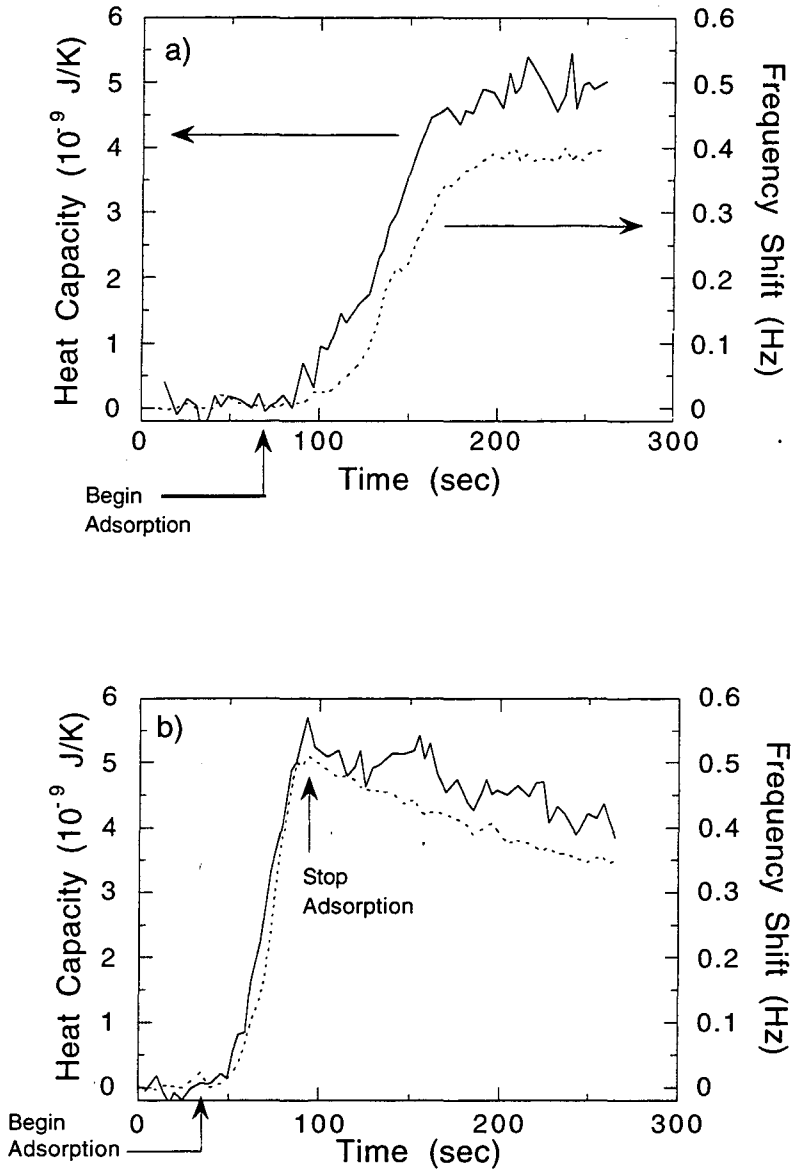

Figure 4.4 Heat capacity (solid curve) and microbalance measurement (dashed curve) of ^{4}He films condensed on an evaporated gold film at 3.0 K. A coverage of 0.1 Å^{-2} corresponds to a frequency shift of 0.54 Hz. a) Gas dosing rate of approximately 0.01 Å^{-2} sec^{-1} begun as indicated by arrow. Valve left open during entire experiment. b) Gas dosing rate twice as large as in a). Valve opened and closed as indicated.

through the room temperature plumbing and cold effusion line, and at t~100 seconds, the heat capacity began to rise and the microbalance resonance shifted downward. The valve was left open so that effusion continued for the duration of the experiment. At this exposure rate, which was of order 10^{14} atoms $cm^{-2}\,sec^{-1}$ incident on the calorimeter, the maximum frequency shift observed was approximately 0.4 Hz corresponding to a coverage of 0.074 $Å^{-2}$, or roughly 60% of the layer completion coverage on graphite. The sticking coefficient was measured to be approximately 10%, with uncertainty due to the factors described in Chapter 3. In comparison, Kenny deduced a temperature-independent sticking coefficient of ~4% for the first half layer of ^4He on silver.[22] When we increased the dosing rate by roughly a factor of two, by changing the flow impedance of the leak valve and the gas pressure in the manifold, we obtained the curve shown in Figure 4.4b. During the dose, we stopped the deposition as indicated by the second arrow. At this higher dose rate, a maximum frequency shift of approximately 0.52 Hz, corresponding to 0.096 $Å^{-2}$, was obtained. Immediately after closing the valve to stop the effusion, the heat capacity and coverage begin to fall, indicating desorption of the ^4He film. The average desorption rate over the next two minutes was 2×10^{-4} $Å^{-2}sec^{-1}$.

We can deduce a binding energy for the adsorbed ^4He to the gold from the desorption rate, as we did for the quench-condensed H_2 in Chapter 3. From Equation 3.3, we compute P_{film}. We calculate the binding energy E_b by equating the chemical potential of a 2D Bose gas with that of a 3D classical vapor above it:

$$E_b + \mu_{bose}(T) = k_B T\left[\ln\left(\frac{P_{film}}{T^{2.5}}\right) - 5.07\right] \quad . \tag{4.7}$$

Equation 4.7 differs from Equation 3.4 in two ways. There is a small negative contribution to the chemical potential of the film, which results from the statistical interaction between the bosons. The different constant on the right side of Equation 4.7 is due to differences in the H_2 and ^4He mass. For a coverage of 0.09 $Å^{-2}$, $\mu_{bose}(3.0\ K) = -3.3$ K, and $E_b = -86 \pm 7$ K. The error in E_b is dominated by the uncertainty in the sticking coefficient α. We very conservatively assume that α can be no more than unity or less than 0.01. These bounds correspond to the minus and plus sign respectively.

In Figure 4.5 we plot the heat capacity of a ^4He film condensed at 3.0 K for an hour after adsorption. The initial fast desorption that had been seen in Figure 4.4b only lasted for a few hundred seconds. Once the coverage had fallen to about 0.065 $Å^{-2}$, the desorption slowed to an approximately constant rate. The entire ^4He film eventually desorbed after 3.5 hours. This second desorption rate corresponds to a binding energy of -95 ± 7 K.

Thus, there appear to be at least two types of binding site on the evaporated gold film, and the physisorption potential is not as smooth as we had hoped. From desorption measurements we cannot determine whether this variation in binding energy corresponds to different types of site on the surface, such as grain boundaries or step edges, or rather to corrugation on atomic length scales. In comparison, Elgin and Goodstein[10] found that 95% of the surface of exfoliated graphite has a binding energy between 143 and 149 K. The amplitude corrugation of the ^4He/graphite potential due to the fixed positions of the carbon atoms is calculated[24] to be 3.25 K. Our measured binding energies on gold are relatively consistent with predictions. Two similar calculations of the ^4He/Au binding energy using a

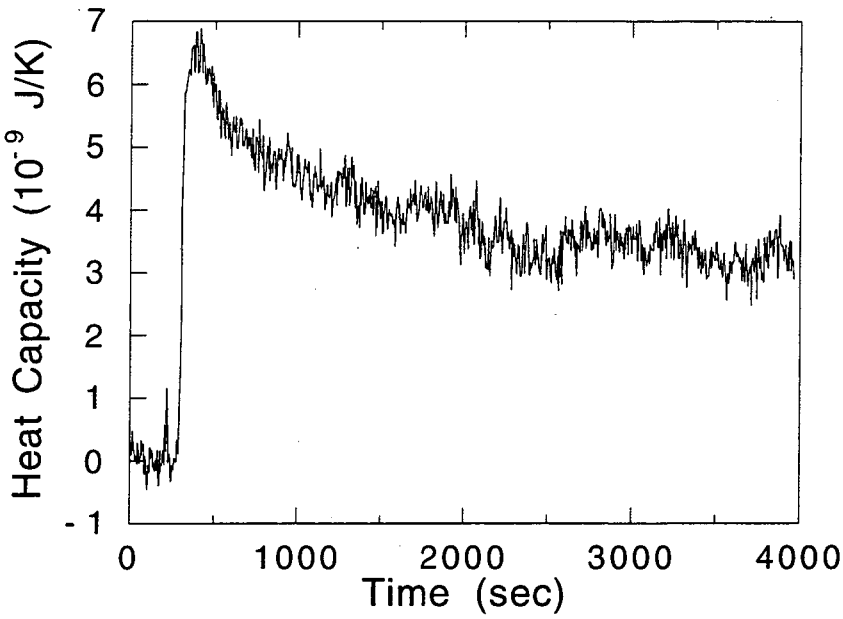

Figure 4.5 Heat capacity of a ^{4}He film condensed on gold measured as a function of time. After 3.5 hours the film had completely desorbed.

jellium model for the metal have yielded values[19,25] of -69 K and -93 K. The well depth for ^{4}He/Au(111) has been calculated to be -89 K.[26] The only experimental investigation of the ^{4}He/Au system, a scattering experiment,[27] yielded a value of the well depth for ^{4}He/Au(110) of -82 K. We note that our deduced binding energies for ^{4}He/evaporated gold are smaller than those observed[22] on evaporated silver, where approximately two layers could be condensed on the substrate at 3.0 K and where desorption of the film only became significant above 3.3 K. This suggests that our evaporated gold surface is less contaminated by tight-binding impurities.

The desorption rate at 3.0 K is slow compared to the time taken to condense a film. Thus the film is in quasi-equilibrium during condensation, and so in Figure 4.6 we plot the heat capacity versus frequency shift and coverage for five condensations at 3.0 K, each shown as a different symbol. Each symbol corresponds to an experiment like that shown in Figure 4.4a, and each individual data point in Figure 4.6 represents three seconds of integration time. The solid curve is the calculation of C(T) for a noninteracting two-dimensional Bose gas and was computed by numerically differentiating Equation 4.3 at 3.0 K. Even at coverages as low as 0.04 Å^{-2}, one third of a layer, the Bose gas result deviates appreciably from the classical result, which is the dashed line in Figure 4.6 with slope k_B/atom. We emphasize that the solid curve is a zero-parameter model. The area of the 2D region, which is required to determine the total number of particles, is taken to be that defined by the evaporation mask. For coverages below 0.06 Å^{-2}, the agreement between the Bose gas result and the experimental data is very good. At higher coverages the experimental points fall below the curve. We note that the coverage where deviation from the Bose gas

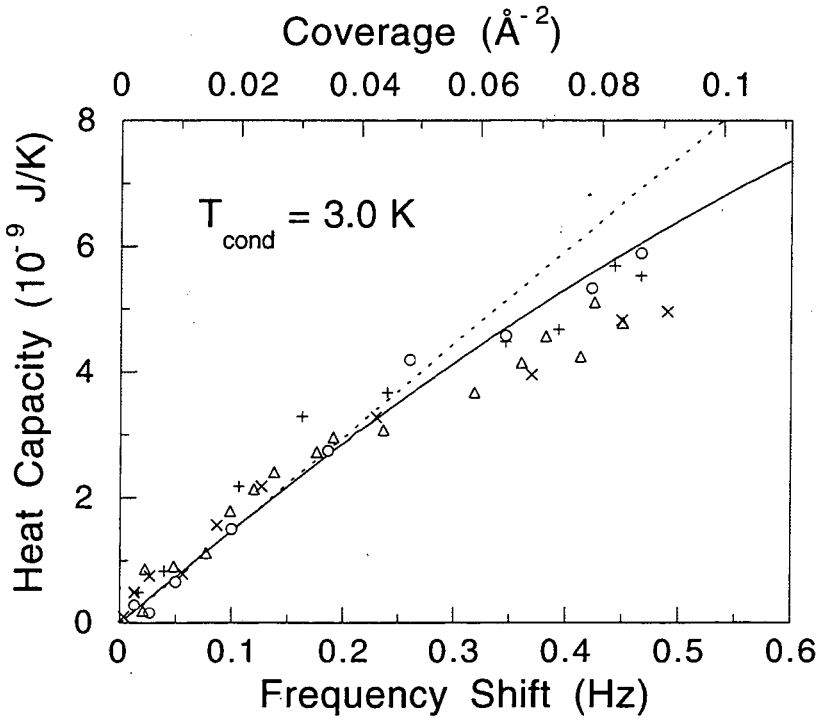

Figure 4.6 Heat capacity versus microblance shift and coverage of ^{4}He films condensed on gold at 3.0 K. The solid curve is the heat capacity of a two-dimensional noninteracting Bose gas. The dashed line is the classical 2D result, k_B/atom.

prediction occurs is comparable to the coverage above which the binding energy decreases by ~9 K.

4.3.2 Films Condensed at 2.4 K

To avoid desorption of the ^{4}He film during measurements, we restricted further investigations to temperatures below 2.4 K. During the thirty minutes required to scan the heat capacity C(T) between 0.4 and 2.4 K, we expected no measurable desorption, given the binding energies deduced in the previous section.

In Figure 4.7 we plot the measured heat capacity versus coverage for five films condensed at 2.4 K and one film condensed at 2.5 K. The procedure for this series of measurements was identical to that for the films condensed at 3.0 K shown in Figure 4.4-4.6. The maximum coverage which could be condensed was about 0.1 Å^{-2}, which is larger than at 3.0 K. For coverages below 0.06 Å^{-2}, there is again good agreement between the experimental data and the 2D noninteracting Bose gas result. At higher coverages there is significant deviation from gas-like behavior. The scans which are shown as open triangles, open circles, and solid circles all show small peaks in the heat capacity versus coverage curve at coverages between 0.078 and 0.095 Å^{-2}. Although these peaks are not much larger than the noise level, we believe they are real because of the coverages at which they occur. A decrease in the heat capacity as the particle density increases suggests the transition of the film into a less mobile state. At 2.4 K on graphite, ^{4}He forms an incommensurate solid for coverages greater than 0.085 Å^{-2}. However, the crossing of this phase boundary on graphite results in a much more prominent peak in the heat capacity versus coverage curve

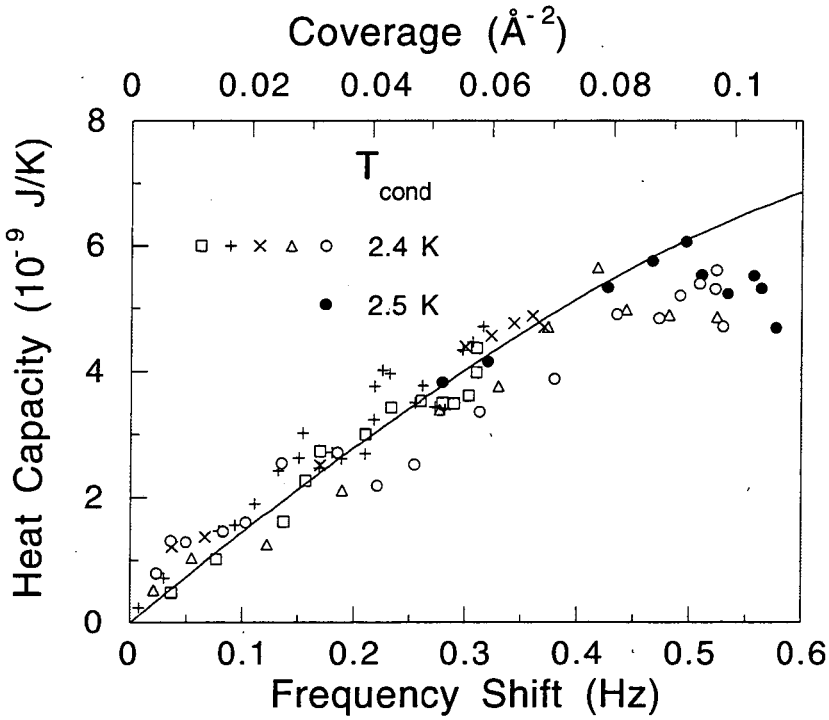

Figure 4.7 Heat capacity versus microblance shift and coverage of five ^{4}He films condensed on gold at 2.4 K and a film condensed at 2.5 K. The solid curve is the heat capacity of a two-dimensional noninteracting Bose gas.

than that seen in Figure 4.7, and at higher coverages the heat capacity of the adsorbate on graphite drops rapidly towards zero as monolayer completion is approached.

4.3.3 C(T) of Films with T_{cond} = 2.4 K

We have measured the heat capacity versus temperature C(T) of several films with coverages between 0.007 and 0.096 $Å^{-2}$. Our preliminary investigations indicated that there were no features in the heat capacity with width greater than 0.05 K large enough to be observed with our calorimeter, so we measured C(T) at relatively large temperature intervals--every 0.1 K between 0.4 and 0.6 K and every 0.2 K up to 2.4 K--to decrease the required measurement time and minimize the effect of 1/f drift. The drift is most problematic for measurements at high temperatures, when the heat capacity of the adsorbate is smallest compared to that of the bare calorimeter. To minimize the effects of the drift, we measured C(T) of the bare calorimeter with T increasing from 0.4 to 2.4 K followed by a scan of C(T) of the dosed calorimeter with T decreasing from 2.4 to 0.4 K. Each scan took about half an hour, with 30 seconds of integration for each of the lowest temperature points and up to 2 minutes at each at the highest temperatures. The dosing of the calorimeter with the ^{4}He took roughly five minutes.

Heat capacity scans C(T) for coverages of 0.007, 0.022, 0.041, 0.050, 0.067 and 0.096 $Å^{-2}$ are shown in Figure 4.8. The coverage was measured with 0.005 $Å^{-2}$ uncertainty--corresponding to microbalance precision of 0.03 Hz--and was limited by microbalance drift. The coverage of the film shown as open circles was not directly measured but was deduced from a comparison of the heat capacity at 2.4 K to the Bose gas result. The error in the heat

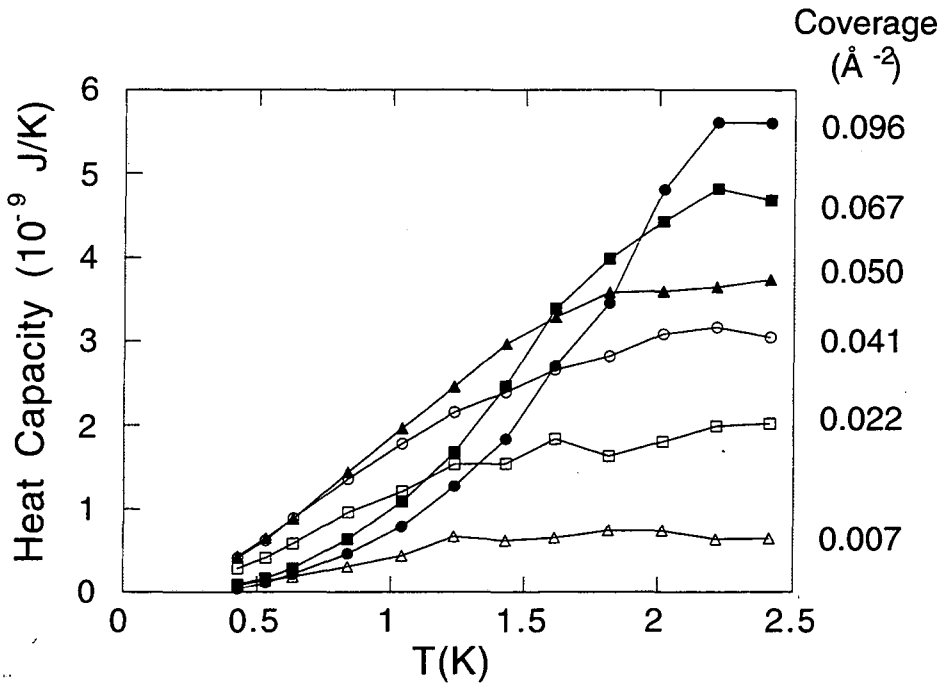

Figure 4.8 Heat capacity as a function of temperature for six coverages of ^{4}He adsorbed on an evaporated Au surface.

capacity depended on temperature and was relatively largest at the high temperatures, because the calorimeter heat capacity increased as T^3, whereas the adsorbate heat capacity was nearly constant. The small bumps in the "flat" region of each curve are comparable to the uncertainty and hence we do not place significance on them.

For all except the largest coverage, the heat capacity at 2.4 K is consistent with the 2D Bose gas result, confirming the results of Figure 4.7. The heat capacity C(T) for all coverages decreases as T is reduced, but no sign of a peak indicating the crossing of a phase boundary is seen for any coverage. There is a clear crossover in the low temperature behavior at a coverage between 0.050 and 0.067 $Å^{-2}$; the heat capacity of the two densest films drops much more rapidly than the others.

In Figure 4.9 we compare three of the lower coverage data sets to calculations for the 2D noninteracting Bose gas. There is good agreement at high temperatures, and the small discrepancies between experiment and theory are consistent with the uncertainties in the coverage and heat capacity measurements. As the temperaure is decreased, however, the experimental data eventually fall below the Bose gas prediction. The disagreement occurs at a temperature which increases from 1.1 K for the 0.007 $Å^{-2}$ film up to 1.7 K for the 0.050 $Å^{-2}$ film.

At coverages up to ~0.04 $Å^{-2}$ on graphite, the heat capacity is proportional to T^2 at low temperatures. In Figure 4.10 we plot C(T) vs. T^2 for our four lowest coverages below 1.3 K to check for a similar temperature dependence. At the lowest temperatures, C(T) for all four coverages is well described by a T^2 dependence, although the range of validity shrinks as coverage is increased. The lines are T^2 fits to the data for $T < 1.3$ K for the

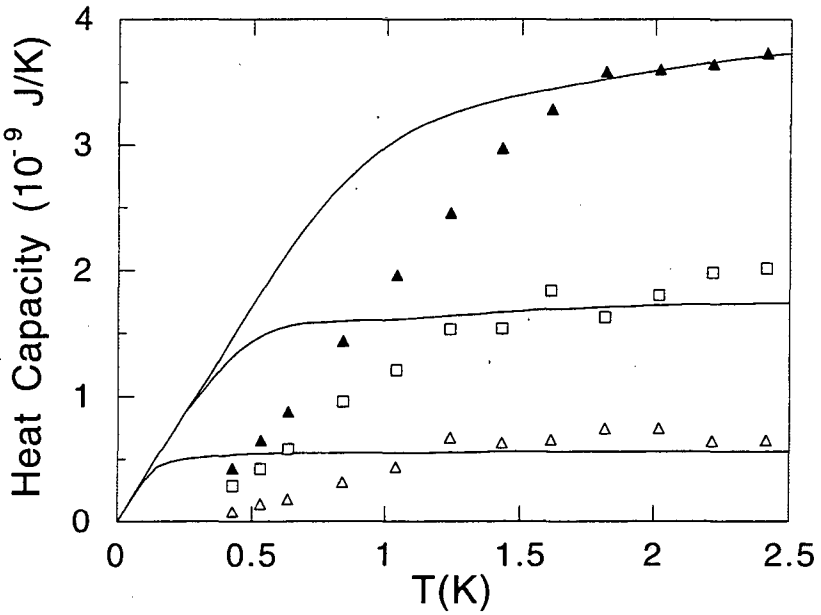

Figure 4.9 Heat capacity of three of the films shown in Figure 4.8, with coverages (in $Å^{-2}$) of 0.050 (solid triangles), 0.022 (open squares), and 0.007 (open triangles). Solid curves are the calculated 2D noninteracting Bose gas heat capacities for coverages of 0.050, 0.022, and 0.007.

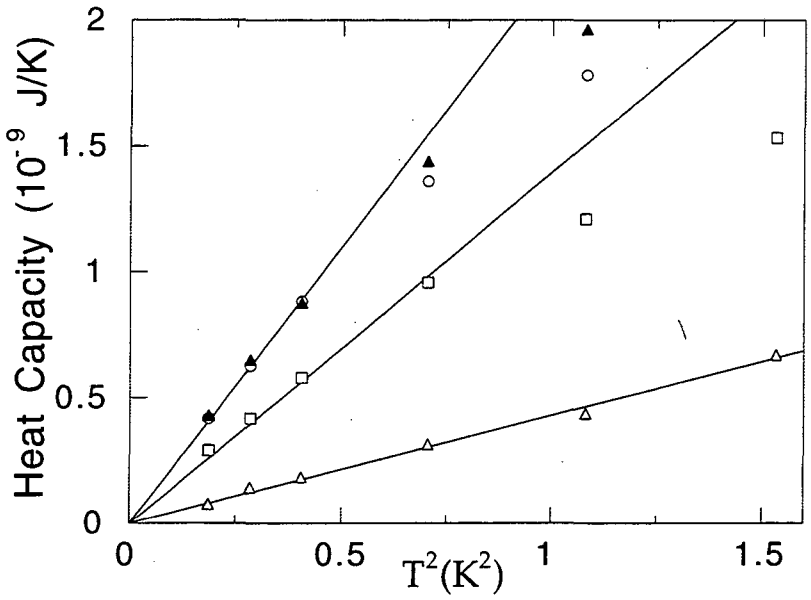

Figure 4.10 Heat capacity of four of the films shown in Figure 4.7, with coverages (in $Å^{-2}$) of 0.050 (solid triangles), 0.041 (open circles), 0.022 (open squares), and 0.007 (open triangles) plotted vs. T^2. Solid lines are fits to the lowest temperature data points.

0.007 Å^{-2} film, T < 0.85 K for the 0.022 Å^{-2} film, and T < 0.65 K for the 0.041 and 0.050 Å^{-2} films. For the 0.007 Å^{-2} film, C(T) switches from a T^2 dependence to the classical k_B/atom over a narrow temperature range near 1.1 K. As the coverage is increased there is a "crossover" temperature region of increasing width where the heat capacity is not well described by either model.

In the previous discussion we assumed that the gold surface was sufficiently smooth for the behavior of dilute adsorbed films of ^{4}He to be similar to that for ^{4}He/graphite. The identification of at least two binding energies suggests that perhaps the evaporated metal surface is disordered and more similar to a surface like Vycor glass. On such a surface, variations of the adsorption potential over large length scales (100 Å) might result in isolated islands of ^{4}He, with a barrier of energy Δ for excitation of the least strongly bound adatom out of the island and into the lowest free-particle state.[6,28] A model density of states[6] for the system is shown in Figure 4.11. The heat capacity of the system consists of two parts: (i) the contribution of the islands themselves and (ii) the contribution associated with single particles excited out of the islands. The contribution from (i) is Debye-like and proportional to T^2. The contribution from (ii) is proportional to T for k_BT comparable or larger than Δ, because the states in the shaded region of Figure 4.11 are either singly occupied or not, and hence subject to Fermi statistics. Thus for temperatures comparable or large compared to the gap, the heat capacity can be expressed[6] as

$$\frac{C(T)}{N\,k_B} = aT + b\,T^2 \quad . \tag{4.8}$$

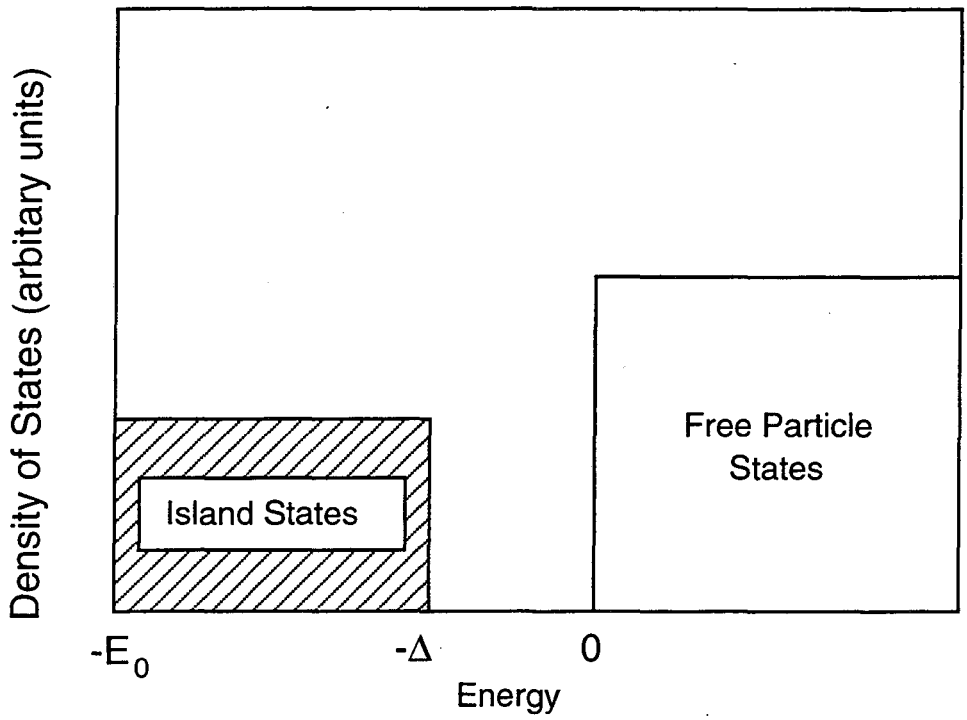

Figure 4.11 Model[6] density of states for ^{4}He/disordered surface.

On Vycor glass, Δ was found[6] to be between 1 and 2 K, and Equation 4.8 was found to be valid above 0.5 K for coverages between approximately 0.3 and 1.5 layers. In Figure 4.12 we plot best fits of Equation 4.8 to the four lowest coverages for $T < 1.3$ K. Over the entire range there is fair agreement. The best fit coefficients are listed in the following table:

coverage (Å^{-2})	a (K^{-1})	b (K^{-2})
0.007	0.05 ± 0.06	0.72 ± 0.06
0.022	0.27 ± 0.05	0.37 ± 0.06
0.040	0.23 ± 0.05	0.26 ± 0.05
0.051	0.15 ± 0.04	0.29 ± 0.04

Table 4.1 Fit Coefficients for Equation 4.8

The temperature dependence of C(T) for the films with coverage 0.067 and 0.096 Å^{-2} is stronger than T^2. On graphite at coverages above ~0.04 Å^{-2}, the phase diagram for ^{4}He includes solids commensurate with the lattice, as well as fluids. The adatom-adatom interactions are small, and hence the adsorbate can be described as a collection of noninteracting Einstein oscillators. There is a gap in the density of states, and the contribution to the heat capacity from the solid is $k_B(\Delta/T)^2 \exp(-\Delta/T)$ per atom. Near 0.0663 Å^{-2}, (the coverage corresponding to perfect registry of the $\sqrt{3} \times \sqrt{3}$ structure,) the best fit to the heat capacity on graphite yields[15] $\Delta = 10.5 \pm 0.1$. Fluids contribute a term to C(T) proportional to T^2. The fluid specific heat for ^{4}He was measured[15] to be 0.56 T^2 at a coverage of 0.0367 Å^{-2} on graphite, and so we use this value as an estimate for the fluid specific heat on gold. In Figure

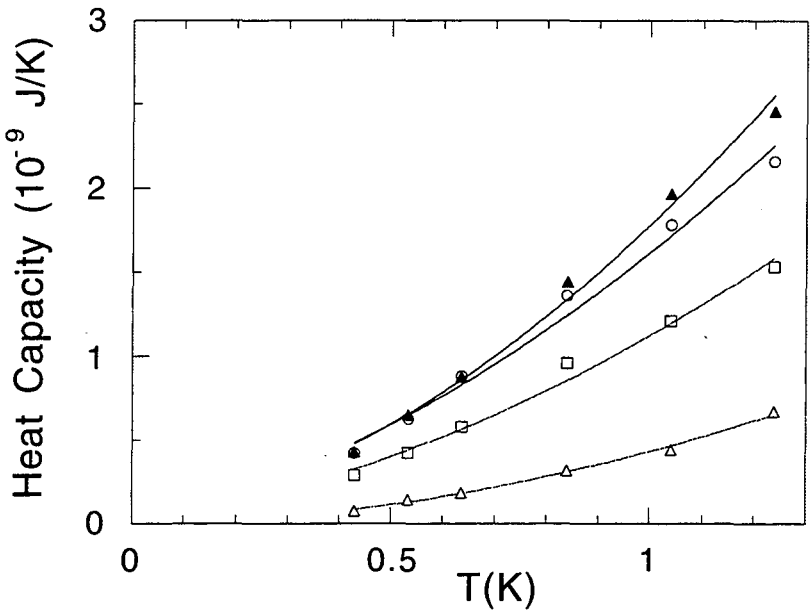

Figure 4.12 Heat capacity of four of the films shown in Figure 4.7, with coverages (in $Å^{-2}$) of 0.050 (solid triangles), 0.041 (open circles), 0.022 (open squares), and 0.007 (open triangles). Solid lines are fits to Equation 4.8 for $T < 1.3$ K.

4.13 we show fits of the heat capacity of the two coverages on gold to the function

$$\frac{C(T)}{N\,k_B} = a(0.56)T^2 + b\left(\frac{\Delta}{T}\right)^2 \exp(-\Delta/T) \quad . \tag{4.9}$$

The coefficients a and b represent the fraction of the film in the fluidlike and solid state, respectively, and should sum to unity. For the 0.067 Å^{-2} film, the fit for $0.4 < T < 1.5$ K is shown as a solid curve in Figure 4.13a and yields values of a = 0.23, b = 1.0, and Δ = 6.8 K. Thus we might interpret this fit as indicating that roughly 20-25% of the atoms make a fluidlike contribution to the heat capacity. A fit to the same coverage between $0.4 < T < 1.3$ K is shown in Figure 4.13a as a dashed curve, and the fitting values obtained are listed in Table 4.2. This fit yields a smaller value for the gap, 5.4 K. The fits of Equation 4.9 to the 0.096 Å^{-2} film are shown in Figure 4.13b. Similar values of Δ but smaller values of a and b are obtained, indicating that ~50% of the atoms are in a state which contributes essentially no heat capacity. This state could be a stiff incommensurate solid.

coverage (Å^{-2})	Fit Range	a	b	Δ (K)
0.067	$0.4 < T < 1.5$ K	0.23 ± 0.04	1.0 ± 0.1	6.8 ± 0.6
0.067	$0.4 < T < 1.3$ K	0.20 ± 0.02	0.60 ± 0.03	5.4 ± 0.3
0.096	$0.4 < T < 1.5$ K	0.11 ± 0.02	0.54 ± 0.05	6.6 ± 0.6
0.096	$0.4 < T < 1.3$ K	0.09 ± 0.02	0.38 ± 0.02	5.6 ± 0.6

Table 4.2 Fit Coefficients for Equation 4.9

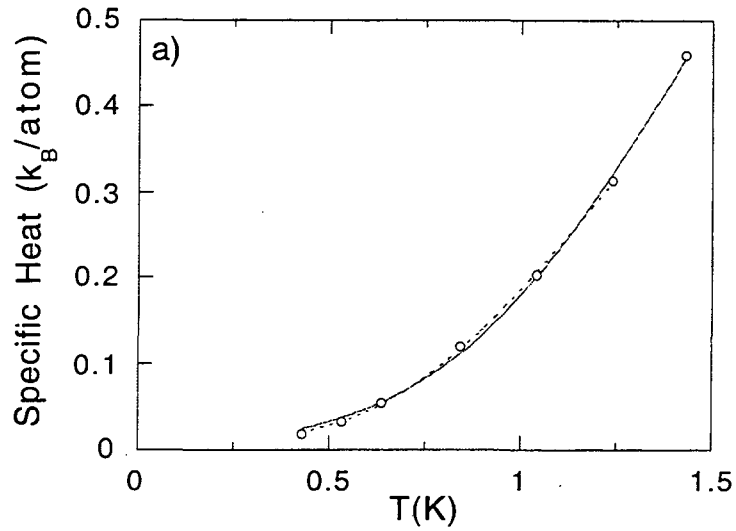

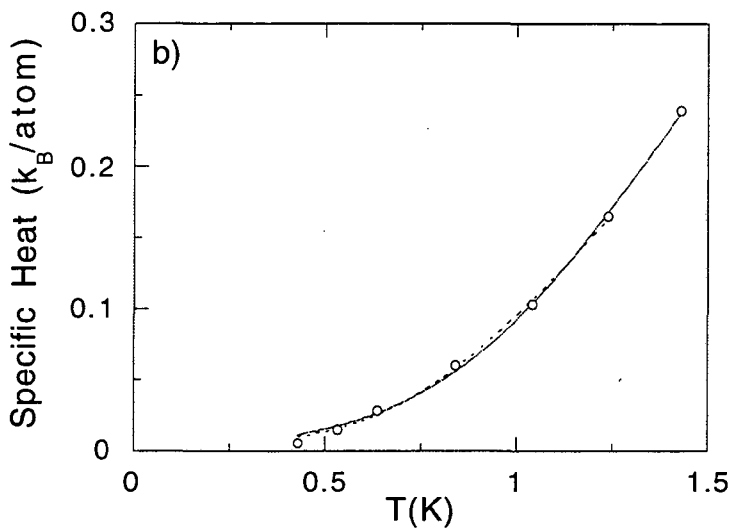

Figure 4.13 a) Specific heat of the 0.067 Å^{-2} ^{4}He film. b) Specific heat of 0.096 Å^{-2} ^{4}He film. The solid curves are best fits of Equation 4.9 to the data between 0.4 and 1.5 K. The dashed curves are fits between 0.4 and 1.3 K.

4.4 Discussion

The heat capacity measurements of ^{4}He submonolayers adsorbed on an evaporated gold surface described in Section 4.3 have led us to construct the phase diagram shown in Figure 4.14. Our results are consistent with the those for the first layer of ^{4}He on silver[22] made at higher temperatures and can be interpreted with an eye to the ^{4}He/graphite phase diagram.[8] The ^{4}He/gold system shows evidence of some, but not all, of the phases seen in the ^{4}He/graphite system. The differences are due to both the differences in the substrate lattice spacings and to the less periodic nature of the evaporated gold substrate.

For coverages of 0.06 Å^{-2} and below, ^{4}He/evaporated gold is a fluid at sufficiently high temperatures. The heat capacity is well described by the calculation for a 2D noninteracting Bose gas until T is reduced below some coverage-dependent temperature. Below this temperature the heat capacity drops more quickly than the Bose gas prediction and eventually becomes proportional to T^2. We have considered two descriptions of the adsorbate in this part of the phase diagram. One possibility is that the ^{4}He behavior is very similar to that on graphite. As in the graphite system, we assign the T^2 region to a coexistence of gas and liquid. For the lowest measured coverage, 0.007 Å^{-2}, the heat capacity smoothly changes from T^2 to gaseous behavior at ~1.1 K. At coverages between 0.022 and 0.050 Å^{-2}, there is a "crossover" temperature range where neither the T^2 nor the Bose gas description is appropriate. However, unlike on graphite, there is no obvious peak denoting the crossing of the phase boundary. We believe that the peak might be broadened because of density variations across the surface resulting from small variations in the binding energy. On graphite, the temperature

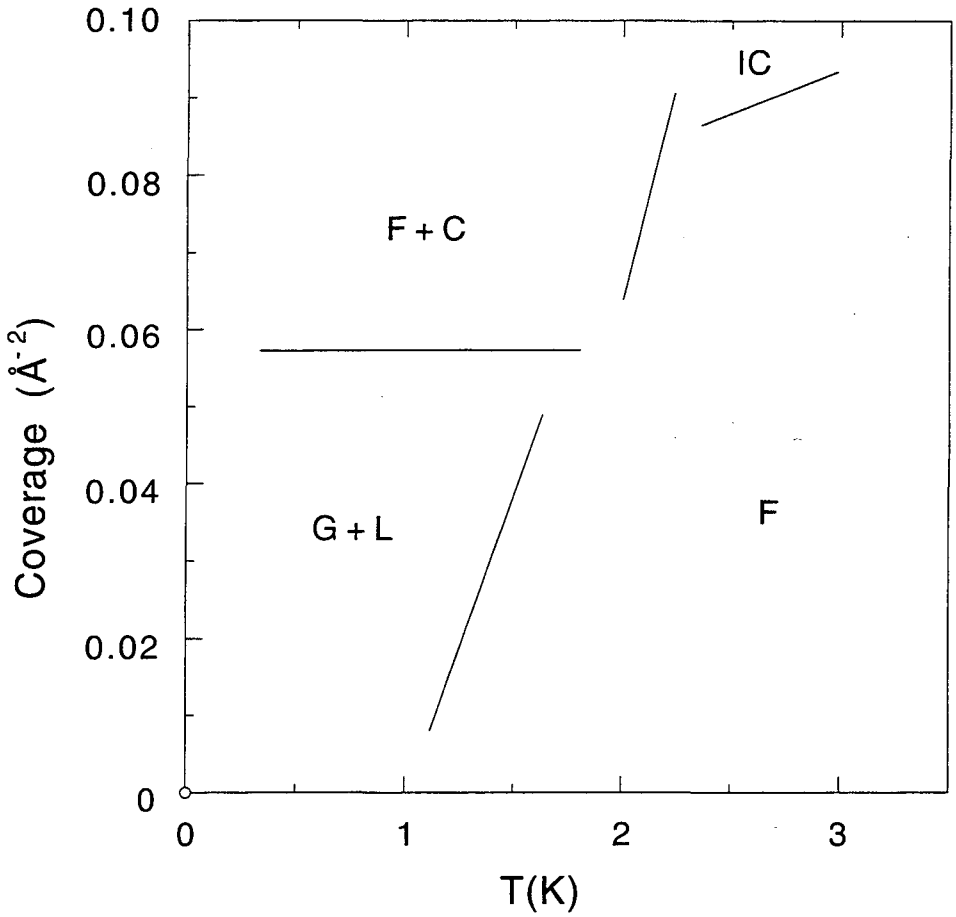

Figure 4.14 Proposed phase diagram for ^{4}He adsorbed on evaporated gold. G: Gas. L: Liquid. F: Fluid. C: Commensurate solid. IC: Incommensurate Solid. Phase boundaries are not well defined; lines shows approximate locations.

where the heat capacity is a maximum varies from ~0.9 K for a coverage of 0.015 $Å^{-2}$ to ~1.5 K for 0.04 $Å^{-2}$. This more or less coincides with the "crossover" temperature range we observe.

Alternatively, the evaporated gold film might be sufficiently disordered that the ^4He forms disconnected islands. The shape of C(T) predicted by this model is consistent with what is observed between 0.4 and 1.3 K. However, the substrates which have been successfully described by this model (sintered copper, noble gas-plated copper, and Vycor glass) are significantly rougher than our evaporated gold. We determined that the binding energy of ^4He to the gold surface varied by approximately 9 K by monitoring the desorption rate of an adsorbed film. On sintered copper, in contrast, measurements[2] of the isoteric heat show that the binding energy decreases by approximately 70 K as the coverage is increased from 0.2 to 1.2 layers. On the evaporated gold we saw clear evidence of a 2D gas at temperatures below 1.5 K; on Ar-plated copper, in contrast, the adatoms are still confined to the islands at temperatures in excess of 4 K.[28] The Debye temperature[28] Θ_D associated with the islands measured on Ar-plated copper is ~30 K, wheras we compute Θ_D to be ~10 K from the data in Table 4.1 and the expression for the Debye contribution to the heat capacity in two dimensions:

$$\frac{C(T)}{N\,k_B} = 28.8\left(\frac{T}{\Theta_D}\right)^2. \tag{4.10}$$

The T^2 specific heat is much closer in magnitude to the liquidlike contribution on graphite. For this reason, and because we have measured the variation in the physisorption potential on gold to be comparable to that

on graphite, we currently favor the first description, where the low temperature phase is a gas/liquid coexistence, in spite of the absence of prominent ordering peaks. The phase boundary drawn in Figure 4.14 is schematic and only indicates where C(T) begins to deviate from the 2D noninteracting Bose gas result.

At coverages of 0.067 and 0.096 $Å^{-2}$, the heat capacity of ^4He/gold is dominated by a gap-like exponential term, which suggests the existence of a commensurate solid at low temperatures. The gap energy is smaller than on graphite, which would be expected because the size of the gap depends strongly on the corrugation amplitude of the holding potential.[29] The solid commensurate with the gold lattice, which we suggest is a $\sqrt{3} \times \sqrt{3}$ stucture, occurs at higher coverages on gold than on graphite. This is consistent with the larger lattice spacing of the Au(111) surface. The nearest neighbor distance[30] on the gold surface is 2.88 Å, which corresponds to perfect registry of the $\sqrt{3} \times \sqrt{3}$ solid at 0.093 $Å^{-2}$. At coverages near 0.085 $Å^{-2}$, we see evidence that part of the film forms a solid incommensurate with the lattice, just as on graphite. However, unlike on graphite, the heat capacity remains relatively large at these coverages indicating that a significant fraction of the film remains in a relatively mobile state, perhaps as a gas or liquid.

4.5 Summary

Calorimetric measurements on ^4He submonolayers deposited on evaporated gold films have been reported. We have measured the coverage dependence of the heat capacity at 3.0 K and 2.4 K and the temperature dependence of the heat capacity at coverages between 0.007 and 0.096 $Å^{-2}$. Our main observations and conclusions are as follows:

1.) There are at least two types of ^{4}He physisorption site on evaporated gold films, with binding energies of -86 ± 7 and -95 ± 7 K. We do not know if the difference in these two energies corresponds to large regions with different physisorption characteristics or to corrugation on atomic length scales. These energies are consistent with calculations and smaller than what has been observed[22] for ^{4}He/evaporated silver.

2.) In spite of this variation in binding energy, the ^{4}He is a noninteracting Bose gas at coverages below 0.06 Å^{-2} at sufficiently high temperatures.

3.) At lower temperatures and higher coverages, the ^{4}He forms condensed phases, including liquids, solids commensurate with the gold lattice, and incommensurate solids.

4.) The phase diagram of ^{4}He/evaporated gold is similar to that for ^{4}He/graphite, but the phase boundaries are shifted and not as well defined, nor is the diagram as rich in structure. No peaks signifying the crossing of phase boundaries are seen at any coverages. This is probably due to density variations of the adsorbate on the surface, which result from variations in the binding energy.

References

1. W.D. McCormick, D.L. Goodstein and J.G. Dash, Phys. Rev. **168**, 249 (1968).

2. D.W. Princehouse, J. Low Temp. Phys. **8**, 287 (1972).

3. J.G. Daunt and P. Mahadev, Physica **69**, 104 (1973).

4. G.A. Stewart and J.G. Dash, Phys. Rev. **A2**, 918 (1970).

5. P. Mahadev, M.F. Panczyk, R.A. Scribner and J.G. Daunt, Phys. Lett. **41A**, 221 (1972).

6. R.H. Tait and J.D. Reppy, Phys. Rev. B. **203**, 997 (1979).

7. J.G. Dash, Films on Solid Surfaces, (Academic Press, New York, 1975) and references therein.

8. D.S. Greywall and P.A. Busch, Phys. Rev. Lett. **67**, 3535 (1991).

9. M. Bretz, J.G. Dash, D.C. Bickernell, E.O. McLean and O.E. Vilches, Phys. Rev. A **8**, 1589 (1973).

10. R.L. Elgin and D.L. Goodstein, Phys. Rev. **A9**, 2657 (1974).

11. R.L. Siddon and M. Schick, Phys. Rev. A **9**, 907 (1974).

12. A.D. Novaco and C.E. Campbell, J. Low Temp. Phys. **11**, 2525 (1975).

13. P.A. Whitlock, G.V. Chester and M.H. Kalos, Phys. Rev. B **38**, 2418 (1988).

14. D.M. Ceperley and E.L. Pollock, Phys. Rev. B **39**, 2084 (1989).

15. D.S. Greywall, Phys. Rev. B. **47**, 309 (1993).

16. M. Bretz, J.G. Dash, D.C. Hickernell, E.O. McLean and O.E. Vilches, Phys. Rev. A **9**, 2814 (1974).

17. D.S. Greywall, Phys. Rev. B **41**, 1842 (1990).

18. D.S. Greywall and P.A. Busch, Phys. Rev. Lett. **65**, 64 (1990).

19. E. Zaremba and W. Kohn, Phys. Rev. B **15**, 1769 (1977).

20. J.P. McKelvey and E.F. Pulver, Am. J. Phys. **32**, 749 (1964).

21. International Crystal Manufacturing Co., Oklahoma City, OK.

22. T.W. Kenny and P.L. Richards, Phys. Rev. Lett. **64**, 2386 (1990).

23. L. Holland, Vacuum Deposition of Thin Films , (John Wiley & Sons Inc., New York, 1956) p. 486-487.

24. M.W. Cole, D.R. Frankl and D.L. Goodstein, Rev. Mod. Phys. **53**, 199 (1981).

25. P. Nordlander and J. Harris, J. Phys. C **17**, 1141 (1984).

26. G. Vidali and M.W. Cole, Surf. Sci. **110**, 10 (1981).

27. K.M. Rieder, T. Engel and N. Garcia, in: Proc. ICSS-4 and ECOSS-3, Cannes, 1980 (Le Vide, les Couches Minces, Suppl. II ,1980) p. 861.

28. N.N. Roy and G.D. Halsey, J. Low Temp. Phys. **4**, 231 (1971).

29. J.M. Gottlieb and L.W. Bruch, Phys. Rev. B **41**, 7195 (1990).

30. G.A. Somorjai, Chemistry in Two Dimensions, (Cornell University Press, Ithaca, 1981) p. 200.

Appendix: Measurement of Optical Absorptivity of $La_{1.87}Sr_{0.13}CuO_4$ Below the Superconducting Plasma Edge

A.1 Introduction

The far-infrared response of materials in the $La_{2-x}Sr_xCuO_4$ family has generated much interest since the discovery of superconductivity in these compounds. However, the mechanism for conductivity perpendicular to the CuO_2 planes (**E**||c) is not completely understood. Two pictures are being considered. In one scenario the material is a bad but fairly conventional metal, with an extremely anisotropic mass and scattering rate for the free carriers.[1] Another very different scenario postulates the absence of any coherent transport along the c-axis in the normal state.[2] Only in the superconducting state is coherent transport restored. This mechanism may drive the formation of the superconducting carriers.

Initially, polycrystalline films of $La_{2-x}Sr_xCuO_4$ were studied and a reflectivity edge was observed near 50 cm^{-1} for temperatures below the superconducting critical temperature T_c.[3-7] More recently, large single crystals have become available and the c-axis optical response has been measured separately from the in-plane optical response. Above T_c the far-infrared reflectance along the c-axis is typical of a doped insulator. Below T_c, however, the response is dominated by the reflectance edge which had been seen in the polycrystalline films, and which arises from the plasma oscillation of the carriers in the superconducting state. The c-axis absorptivity in these materials is much larger than the in-plane absorptivity and hence dominated the loss in the polycrystalline films.

Single-crystal reflectance results above the plasma edge from several groups are in agreement.[1,8,9] At frequencies below the edge, reflectance measurements are difficult because the absorptivity becomes smaller than the ~1% accuracy of the reflectance measurements. In addition, far-infrared measurements in general become increasingly challenging as the frequency is reduced. These experimental difficulties have hindered efforts to observe the low frequency behavior which could provide insight into the nature of the superconductivity in $La_{2-x}Sr_xCuO_4$. At frequencies below the edge, direct absorptivity measurements are superior to reflectance measurements and can reveal information not easily obtained by any other method.

The $La_{1.87}Sr_{0.13}CuO_4$ single crystal was grown by the traveling-solvent floating-zone method.[10] The measurements were made on a mechanically polished (100) surface. The orientation of the axes was determined[9] by Raman scattering and x-ray diffraction in Laue geometry. The face of the sample had a semicircular shape with a diameter of 7 mm. The thickness of the sample was about 1 mm.

Absorptivity measurements are particularly powerful when combined with ellipsometric measurements made at higher frequencies. The complex dielectric function or conductivity can then be computed accurately down to the lowest measured frequency using the Kramers-Kronig relations. We have directly measured the absorptivity of a $La_{1.87}Sr_{0.13}CuO_4$ crystal ($T_C = 31$ K) along the c-axis between 6 and 520 cm^{-1} at 1.5 K. These measurements complement ellipsometric reflectance measurements[9] made on the same sample between 35 and 700 cm^{-1} at 10 K.

A.2 Experimental Technique

To directly measure the optical absorptivity of the $La_{1.87}Sr_{0.13}CuO_4$ crystal, we have used it as the absorbing element in a composite bolometric far-infrared detector used in conjunction with a step-scan Michelson Fourier spectrometer. The crystal is suspended in vacuum by nylon threads. A small neutron-transmutation-doped (NTD) Ge thermistor[11] and a NiCr heater are glued to the back side of the crystal. The time constant $\tau=C/G$ of the bolometer is determined by the heat capacity C of the crystal and the attachments to it and by the thermal conductance G of the electrical leads which connect the ~2 K thermistor to the heat sink at ~1.5 K.

A schematic of the cryogenic portion of the apparatus[12] is shown in Figure A.1. Chopped infrared radiation from the spectrometer passes through a light pipe and both warm and cold low pass filters and is split approximately symmetrically by a roof mirror into two beams. The cold filter is chosen to minimize background optical loading which reduces detector sensitivity. A 15 μm thick black polypropylene filter is used for the high frequency measurements; a 50 μm thick MIR-X filter[13] is used for frequencies between 20 and 50 cm^{-1}, and a 1 mm thick Fluorogold[14] filter is used for frequencies below 20 cm^{-1}. One beam passes through a grid polarizer[15] with a 3.6 μm grid period to the superconducting sample bolometer; the other beam is directed to a reference bolometer with a well-characterized sputtered gold film on sapphire as the absorbing element.

We measure the responses of the $La_{1.87}Sr_{0.13}CuO_4$ and gold reference bolometers with a lock-in amplifier. The measured output spectrum from the sample detector can be expressed as $F_s(\omega) = L_s(\omega)T(\omega)A_s(\omega)R_s(f)$, where $L_s(\omega)$ is the light spectrum incident on the sample bolometer, $T(\omega)$ is the

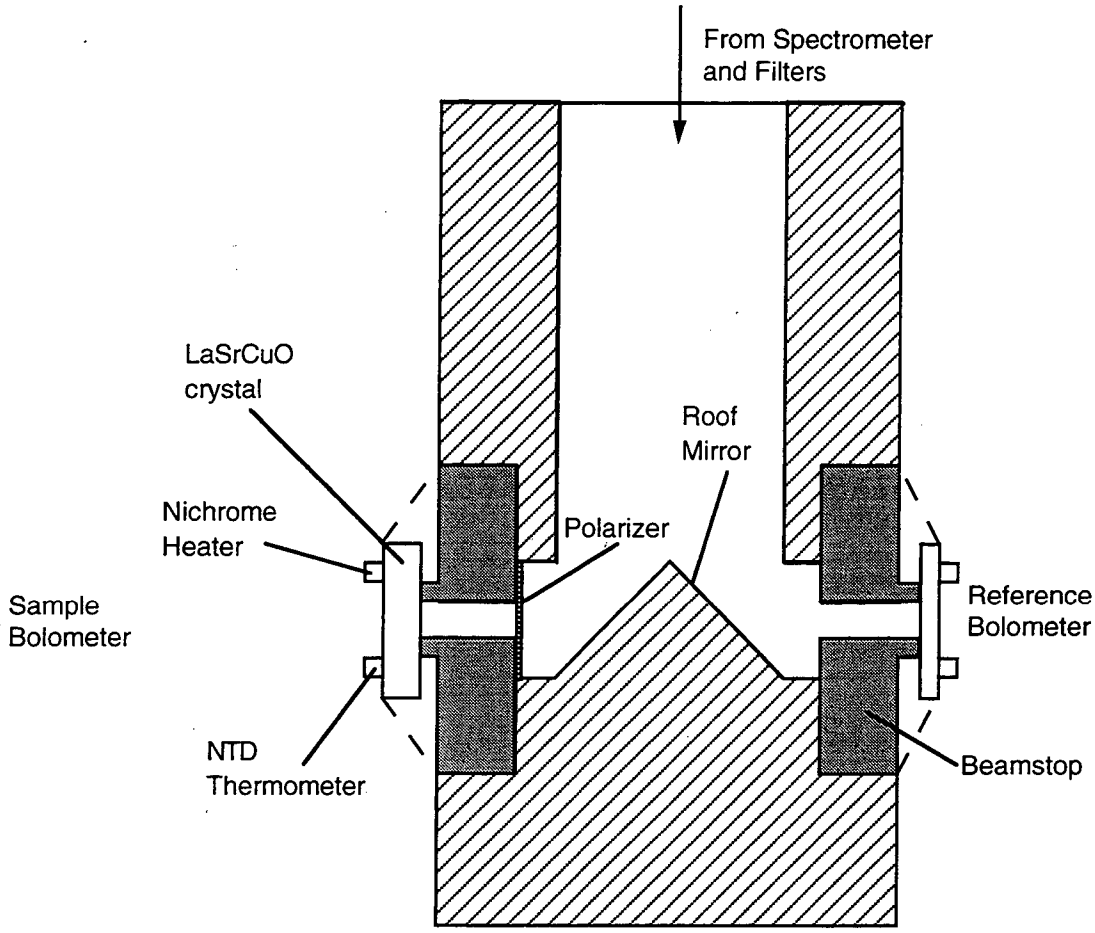

Figure A.1: Cryogenic portion of experimental apparatus. Chopped radiation from the spectrometer is split symmetrically by the roof mirror and directed through beamstops toward the sample and reference bolometers.

transmittance of the polarizer, $A_s(\omega)$ is the absorptivity of the sample, and $R_s(f)$ is the responsivity of the sample detector to absorbed optical power chopped at frequency f. The output spectrum from the reference detector is given by a similar expression, $F_r(\omega) = L_r(\omega)A_r(\omega)R_r(f)$, where the polarizer transmittance $T(\omega)$ has been replaced by unity. Since the spectrum reflected off each side of the roof mirror is approximately the same, the absorptivity of the superconducting sample can therefore be determined from the measured output spectra and the responsivities of the two bolometers:

$$A_s(\omega) = \frac{F_s(\omega)\, R_r(f)\, A_r(\omega)}{F_r(\omega)\, R_s(f)\, T(\omega)} \quad . \tag{A.1}$$

The absorptivity $A_r(\omega)$ of the gold reference absorber is well described by the classical skin effect with $n = 3.6 \times 10^{22}$ cm^{-3} and $\rho = 5.9\ \mu\Omega$.[12] The polarizer transmittance $T(\omega)$ is shown in Figure 2 of Reference 15. At 50 cm^{-1}, the transmittance is close to the ideal value of 0.5 but falls to 0.35 at higher frequencies, primarily because of reflection and absorption by the mylar substrate. The transmittance of crossed polarizers varies from 2 to 6 percent over the frequency range of our measurement. We have measured the a-axis absorptivity to be an order of magnitude smaller than the c-axis absorptivity at frequencies above the plasma edge. These results will also be shown in the next section. At these frequencies the polarizer leakage does not significantly affect our c-axis results.

The responsivities of the two bolometers to absorbed optical power were obtained from a combination of electrical and optical measurements. We dissipated electrical power at 7 Hz in NiCr heaters attached to the bolometers and measured the responses of the Ge thermistors to determine

the electrical responsitivities at this frequency. We then measured the frequency dependence of the response of each bolometer to chopped optical and electrical power and confirmed that they were identical. Thus, the same simple thermal circuits could be used to model the devices for both optical and electrical loading, and the responsitivities to absorbed optical power could be equated with the electrical responsitivities.

Our measurement is subject to the following errors: We have measured $L(\omega)$ to be the same for each bolometer within 5%, differing only by a frequency-independent multiplicative factor which arises from asymmetry in the two optical paths. The responsivities $R_r(f)$ and $R_s(f)$ are also independent of ω and have been measured to better than 10% accuracy. The polarizer transmittance $T(\omega)$ introduces a frequency-dependent error of less than 3%. Since the signal-to-noise ratios of the output spectra $F_r(\omega)$ and $F_s(\omega)$ are about 100 for all but the lowest frequencies measured, the absorptivity is known to within a scaling factor of approximately 15%, while the shape is known to a few percent. The uncertainty becomes significantly larger for frequencies below 15 cm^{-1}.

A.3 Absorptivity Measurements

In Figures A.2 and A.3 we plot the measured c-axis absorptivity of the $La_{1.87}Sr_{0.13}CuO_4$ crystal and compare with reflectance spectra calculated from ellipsometric measurements[9] made on the same sample at 10 K. Figure A.2 shows the data between 120 and 520 cm^{-1}. The agreement is excellent over the entire frequency range, and the optical phonons at 312 and 352 cm^{-1} are apparent.[9] Between 420 and 480 cm^{-1}, we were not able to obtain accurate absorptivity measurements because of two strong absorption lines from the

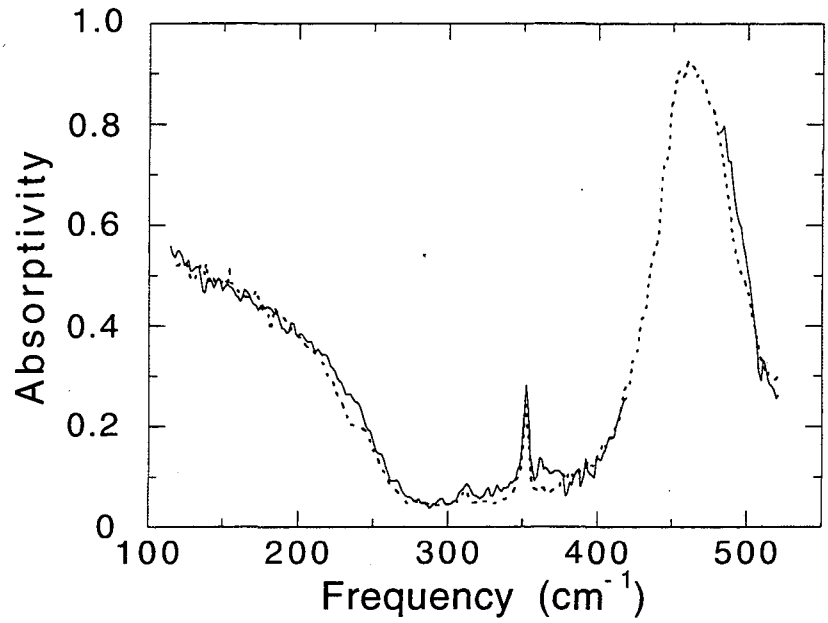

Figure A.2: Absorptivity along c-axis of $La_{1.87}Sr_{0.13}CuO_4$ crystal measured directly at 1.5 K at 1.5 cm^{-1} resolution (solid curve) and deduced from reflectance measurements[9] at 10 K (dashed curve).

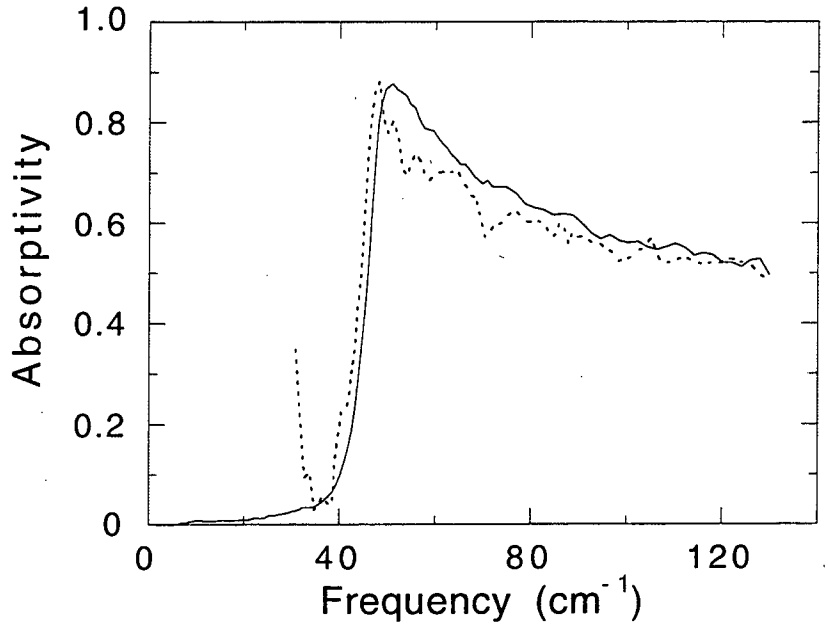

Figure A.3: Absorptivity along c-axis of $La_{1.87}Sr_{0.13}CuO_4$ crystal measured directly at 1.5 K at 0.8 cm^{-1} resolution (solid curve) and deduced from reflectance measurements[9] at 10 K (dashed curve).

mylar substrate of the polarizer and beam splitter. In Figure A.3, data from the same two measurements are plotted between 6 and 120 cm^{-1}. There is a steep rise of absorptivity at approximately 41 cm^{-1}, which we identify as the screened plasma frequency. The rise occurs 1-2 cm^{-1} higher than seen in reflectance[9] at 10 K, which indicates that additional carriers are added to the condensate upon cooling the material from 10 K to 1.5 K. The peak absorptivity measured is comparable to that measured by reflectance. The shapes of the curves above the peaks are slightly different but consistent within the uncertainty of the measurements. Below the plasma edge, the absorptivity remains non-zero, falling from 9% at 40 cm^{-1} to less than 1% at 15 cm^{-1}. The ellipsometric measurements do not yield useful information below 35 cm^{-1}.

The absorptivity below 40 cm^{-1} is replotted in Figure A.4. It drops rapidly with decreasing frequency until approximately 12 cm^{-1}, where it rises to a small peak at 10 cm^{-1}, and then falls close to zero at lower frequencies. Although this peak is small, it appears to be a real feature in the optical response of $La_{1.87}Sr_{0.13}CuO_4$ since it was reproduced in different experimental runs, involving different optical path geometries and filtering. Additional small peaks are seen at 26 and 33 cm^{-1}. Between 12 cm^{-1} and 35 cm^{-1}, the absorptivity is well described by a square-law frequency dependence.

In Figures A.5 we plot the measured a-axis absorptivity of the $La_{1.87}Sr_{0.13}CuO_4$ crystal between 6 and 100 cm^{-1} to compare with the c-axis data shown in the previous figures. At frequencies below the plasma edge, the measured absorptivity along the two directions is essentially identical. There is a peak in the a-axis absorptivity at very nearly the same frequency as

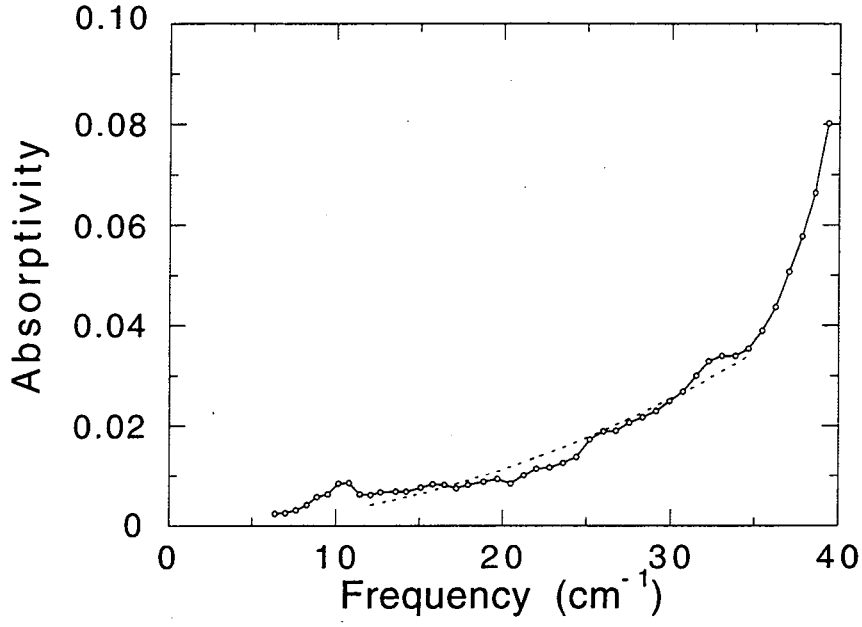

Figure A.4: Absorptivity along c-axis of $La_{1.87}Sr_{0.13}CuO_4$ crystal for frequencies below 40 cm^{-1} (open symbols and solid curve) and square-law fit to data between 12 and 35 cm^{-1} (dashed curve).

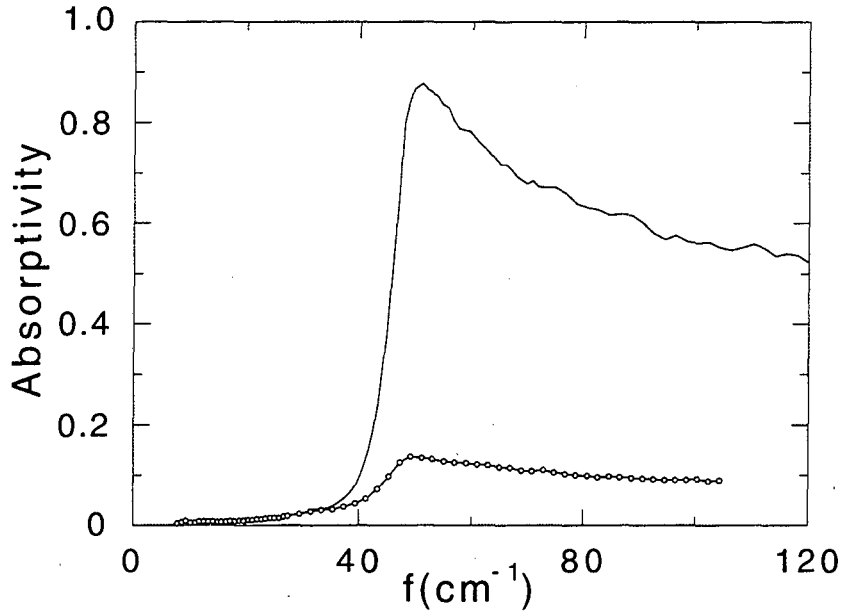

Figure A.5: Measured absorptivity along a-axis of $La_{1.87}Sr_{0.13}CuO_4$ crystal (open symbols) and along c-axis (solid curve).

the c-axis peak absorptivity, which we again identify as the screened plasma frequency for conduction along the c-axis, because the plasma frequency for conduction within the CuO_2 planes has been measured[1] to be ~6000 cm^{-1}. In Figure A.6 we plot the ratio of the a-axis absorptivity to the c-axis absorptivity. The peak a-axis absorptivity is about 16% as large as the peak c-axis absorptivity, but if we subtract a contribution from both absorptivity measurements equal to the absorptivity at the base of the plasma edge, we find that a-axis absorptivity above the peak is very similar in shape to the c-axis absorptivity and about 12% as large. We believe this is due to c-axis leakage. We expect some c-axis response to corrupt the a-axis measurement. The polarizer allows 4-5% of the wrong polarization to be transmitted at these frequencies. The crystal axes are oriented with respect to the polarizer grid by eye with an uncertainty of about 5°. A 12% c-axis leakage would be consistent with these sources of error. To the best of our knowledge, there has been only one measurement[16] of the in-plane reflectance of $La_{2-x}Sr_xCuO_4$ in the superconducting state in our frequency range. The reflectance of an 820 nm thick $La_{2-x}Sr_xCuO_4$ film was measured to be approximately 99% at 100 cm^{-1}. At lower frequencies, the deviation from unity was smaller than the experimental error. We note that in that investigation the wave vector **q** of the light was parallel to the c-axis, while in our a-axis measurement $\mathbf{q} \perp c$. The two situations could result in different electron-phonon interactions.[17]

A.4 Kramers-Kronig Analysis

We utilize the Kramers-Kronig relations in conjunction with our absorptivity data, ellipsometric reflectance measurements made on the same

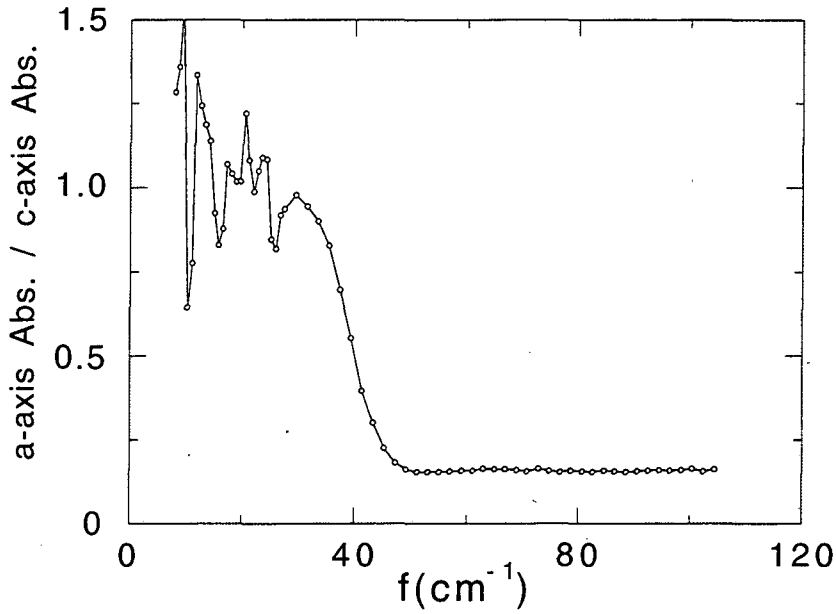

Figure A.6: Ratio of aborptivity measured along a-axis of $La_{1.87}Sr_{0.13}CuO_4$ crystal to that measured along c-axis.

sample, other high frequency reflectance data, and a low frequency extrapolation to determine the complex dielectric function $\tilde{\varepsilon}(\omega)$ or equivalently the complex conductivity $\tilde{\sigma}(\omega)$ of $La_{1.87}Sr_{0.13}CuO_4$. We compute the phase function $\theta(\omega)$ using the Kramers-Kronig relation

$$\theta(\omega) = \frac{\omega}{\pi}\int_0^\infty \frac{ln R(\omega') - ln R(\omega)}{\omega^2 - \omega'^2}\, d\omega' \qquad (A.2)$$

and compare it to the phase measured directly using ellipsometry. From the difference over the frequency range of overlap, we compute an error function which we extrapolate to low frequencies to correct the phase at those frequencies. From $R(\omega)$ and $\theta(\omega)$, we then compute $\tilde{\varepsilon}(\omega)$ or $\tilde{\sigma}(\omega)$. In this manner we recover the phase information that is necessarily lost in the absorptivity measurement. The combination of low frequency absorptivity measurements and ellipsometry is particularly powerful for deducing the complex behavior at frequencies below the edge, since no modeling of $R(\omega)$ is required.

Since we have absorptivity and reflectance data for overlapping frequency ranges, we must choose where to connect the data sets to generate the $R(\omega)$ to be used in Equation A.2. From Figure A.3, we conclude that for frequencies below 100 cm^{-1}, the signal-to-noise ratio is larger for the absorptivity measurement than the reflectance measurement. However, the noisier reflectance measurement might be more accurate in magnitude and shape because of the uncertainties in the absorptivity technique discussed in the previous section.

We have done KK analyses of two different data sets $R(\omega)$ assembled from the absorptivity and reflectance measurements. Features common to both transformed data sets can be accepted with a high level of confidence. For data set A, we combine absorptivity data for frequencies below 36 cm^{-1} with reflectance measurements made on the same sample between 36 and 650 cm^{-1}. For higher frequencies between 700 and 10,000 cm^{-1}, we use reflectance data[8] for $La_{1.85}Sr_{0.15}CuO_4$ whose response above the plasma edge is quite similar to that of $La_{1.87}Sr_{0.13}CuO_4$.

For data set B, we have used absorptivity measurements for frequencies below 420 cm^{-1}, reflectance measurements made on the same sample between 420 and 650 cm^{-1}, and the same high frequency reflectance data for frequencies up to 10000 cm^{-1}. If the dominant error in the absorptivity measurement is a frequency-independent multiplicative factor, this should be a good choice for calculating the low frequency phase, because the mulitiplicative factors will cancel in Equation A.2 over the range of integration which most contributes to the phase.

For both data sets, we have tried three different low frequency extrapolations: $R(\omega)$ constant and equal to $R(6\ cm^{-1})$, $R(\omega) = A\omega^2$ to match $R(6\ cm^{-1})$, and $R(\omega)$ equal to unity below 6 cm^{-1}. The $\theta(\omega)$ computed from Equation A.2 using the three low frequency extrapolations were nearly indistinguishable, even below 10 cm^{-1}. We have chosen to use the physically reasonable square law extrapolation in the data analysis, which is also suggested by our data. Below 10 cm^{-1} where $R(\omega)$ is above 0.99, the uncertainty in $R(\omega)$ rather than the extrapolation dominates the uncertainty in $\theta(\omega)$ and hence in $\tilde{\varepsilon}(\omega)$ and $\tilde{\sigma}(\omega)$.

We compared the phase calculated from Equation A.2 for data set A to the phase directly measured[9] between 36 cm^{-1} and 425 cm^{-1}, and we used the difference to create[18] a correction function which we extrapolated to low frequencies to generate $\theta_{cor}(\omega)$ over the frequency range of the absorptivity measurements. From $R(\omega)$ and $\theta_{cor}(\omega)$ we computed $n(\omega)$ and $k(\omega)$, from which we calculated the complex dielectric function $\tilde{\varepsilon}(\omega)$ and complex conductivity $\tilde{\sigma}(\omega)$. For data set B, we did not correct the phase calculated from Equation A.2. In Figure A.7 we plot $\varepsilon_1(\omega)$ calculated from both data sets for frequencies between 6 and 100 cm^{-1}. The $\varepsilon_1(\omega)$ measured with ellipsometry is indistinguishable from the calculated values for frequencies between 35 and 100 cm^{-1}. In Figure A.8 we plot the real part of the conductivity $\sigma_1(\omega)$ for $6 < \omega < 150$ cm^{-1} calculated from both KK analyses to compare with the direct measurement[9] of $\sigma_1(\omega)$ from ellipsometry. For comparison, we also plot $\sigma_1(\omega)$ for a $La_{1.84}Sr_{0.16}CuO_4$ crystal ($T_c = 34$ K) calculated from KK analysis of reflectivity data[1] above 25 cm^{-1}. In this data set and our data set B a small bump is seen in $\sigma_1(\omega)$ near 50 cm^{-1}. This resonance has been discussed but not explained by Basov and coworkers.[19]

A.5 Discussion

It is clearly shown in Figure A.4 that the absorptivity along the c-axis of $La_{1.87}Sr_{0.13}CuO_4$ is non-zero down to 6 cm^{-1}. The ω^2 dependence of $A(\omega)$ below 35 cm^{-1} suggests that a fraction of the carriers remain unpaired and can be described as a normal Drude liquid, even below 2 K. This loss may result from pair-breaking or may suggest an asymmetric superconducting gap with nodes, such as the d-wave gap which has been proposed and

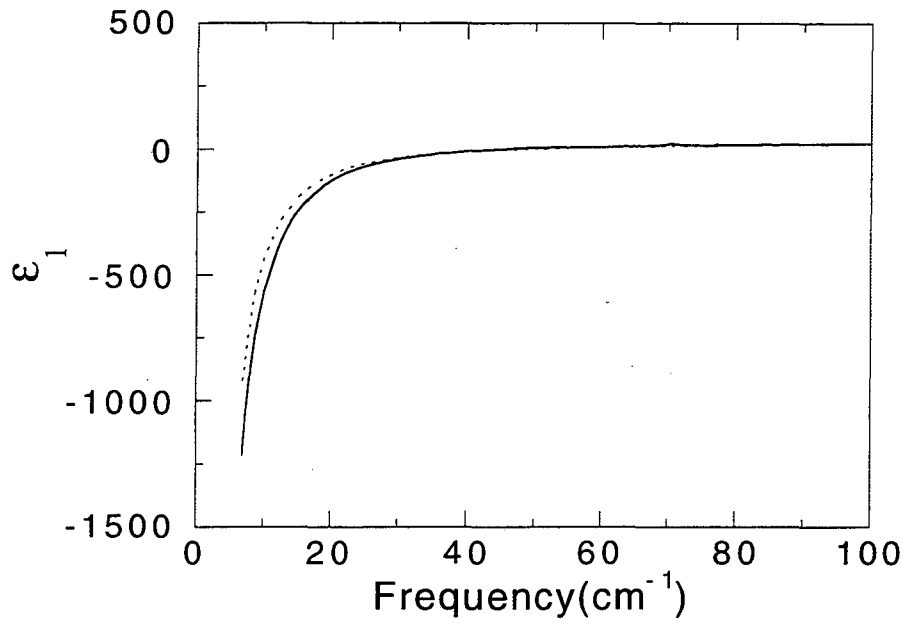

Figure A.7: ε_1 computed from Kramers-Kronig analysis of two data sets. The solid curve corresponds to data set A, which combines direct absorptivity measurements at 1.5 K for frequencies below 36 cm^{-1} with reflectance measurements at 10 K above 36 cm^{-1}. The dashed curve corresponds to data set B, which combines absorptivity and reflectance measurements below and above 420 cm^{-1}, respectively. ε_1 measured directly with ellipsometry above 36 cm^{-1} is indistinguishable from either curve.

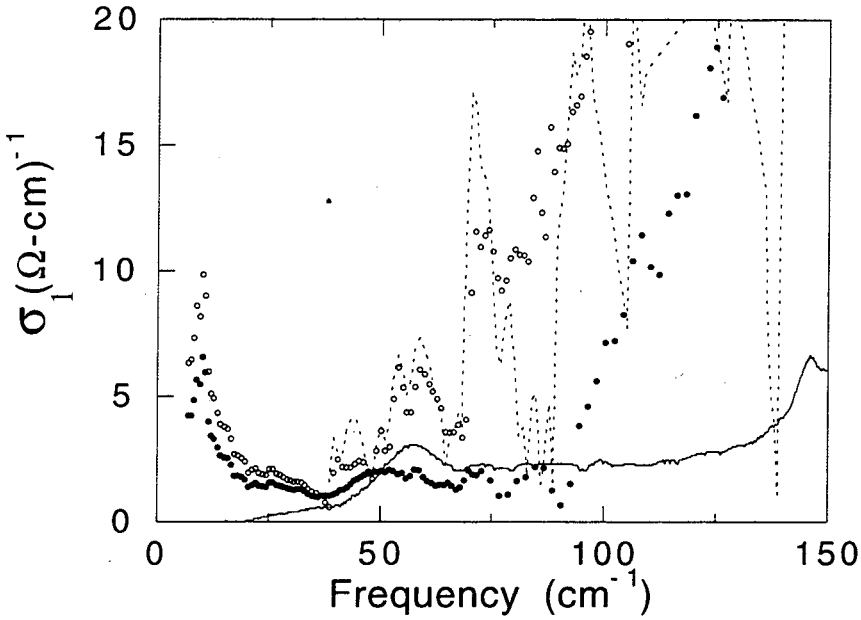

Figure A.8: σ_1 for $La_{1.87}Sr_{0.13}CuO_4$ computed from Kramers-Kronig analysis of data set A (open circles,) computed from Kramers-Kronig analysis of data set B (solid circles,) and measured directly with ellipsometry (dashed curve), and σ_1 computed from Kramers-Kronig analysis of c-axis reflectivity data[1] at 8 K for $La_{1.84}Sr_{0.16}CuO_4$ (solid curve.)

supported by evidence from experiments including microwave, NMR, magnetic, and photoemission measurements.[20]

Following the two-fluid Gorter-Casimir model,[21] we write $\tilde{\varepsilon}(\omega)$ as a sum of contributions from phonons, a superconducting London liquid, and a normal Drude liquid with scattering rate Γ:

$$\tilde{\varepsilon}(\omega) = \varepsilon_\infty - \frac{\omega_{ps}^2}{\omega^2} + \frac{\omega_{p0}^2 - \omega_{ps}^2}{\omega(\omega + i\Gamma)}, \tag{A.3}$$

where ω_{ps}^2 is proportional to the number of superconducting carriers and $\omega_{p0}^2 - \omega_{ps}^2$ is proportional to the number of unpaired carriers. There is disagreement over the description of the normal state. It has been proposed both that the superconductivity is "clean"[9] with $\omega_{ps} \approx \omega_{p0}$ and "dirty"[8] with $\omega_{ps} \ll \omega_{p0}$. In Figure A.9 we plot $\omega_{ps}(\omega)$ calculated for data sets A and B from Equation A.3 for both a relatively clean parameterization ($e_\infty = 20$, $\omega_{p0} = 260$ cm^{-1} and $\Gamma = 120$ cm^{-1})[9] and a dirty parameterization($e_\infty = 25$, $\omega_{p0} = 1320$ cm^{-1} and $\Gamma = 4670$ cm^{-1}.)[8] We also plot $\omega_{ps}(\omega)$ computed from an algebraic treatment of the data[9]

$$\omega_{ps}^2 = \omega^2 \left(\varepsilon_\infty' - \varepsilon_1(\omega) + \frac{\varepsilon_2^2(\omega)\, \omega^2}{\omega^2 \left(\varepsilon_\infty - \varepsilon_1(\omega)\right) - \omega_{p0}^2} \right) \tag{A.4}$$

for both the clean and dirty normal fluid descriptions. The extrapolation of $\omega_{ps}(\omega)$ for $\omega \rightarrow 0$ depends only weakly on the parameterization used and yields a value of ω_{ps} of about 250 cm^{-1} for data set A and 220 cm^{-1} for data set B. This measurement is consistent with the observed reflectivity edge which occurs at the screened plasma frequency $\omega_p = \omega_{ps}/(\varepsilon_\infty)^{1/2}$. An extrapolation of

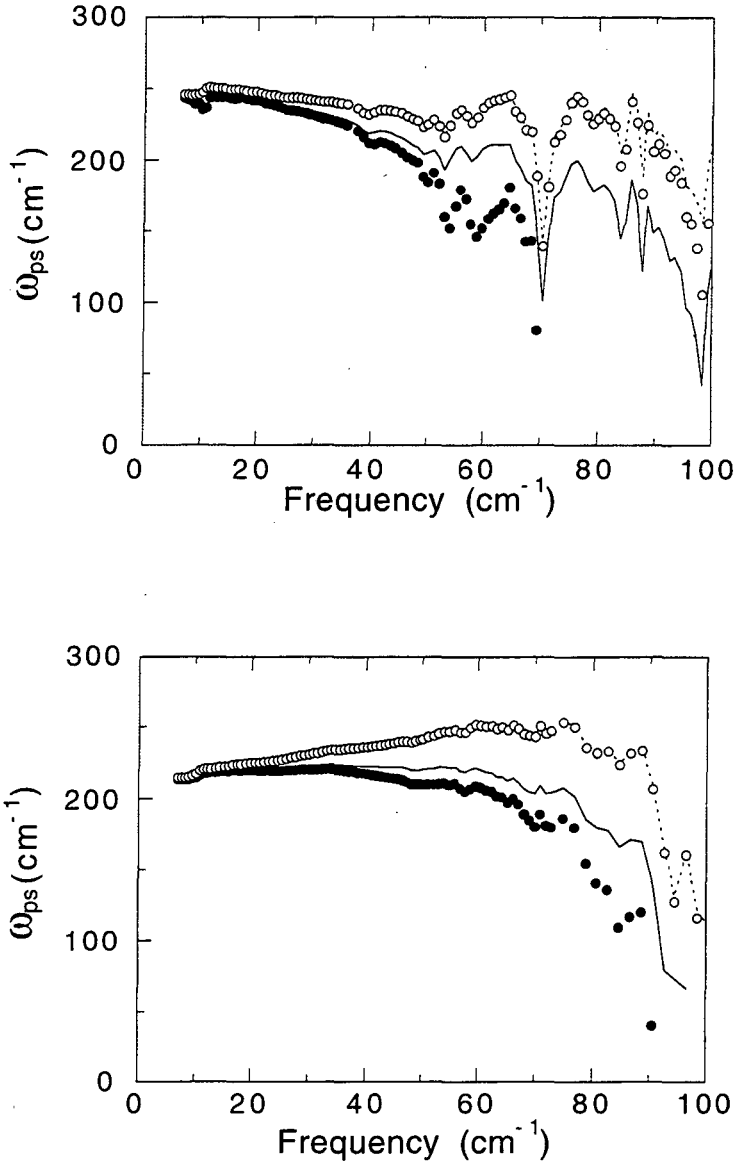

Figure A.9: a) $\omega_{ps}(\omega)$ computed from $\tilde{\varepsilon}(\omega)$ calculated for data set A from Equation A.3 assuming a clean parameterization of the normal fluid from Reference 9 (solid curve) and a dirty parameterization from reference 8 (dashed curve) and from Equation A.4 from parameters of Reference 9 (solid circles) and Reference 8 (open circles.) b) $\omega_{ps}(\omega)$ computed from $\tilde{\varepsilon}(\omega)$ calculated for data set B from Equations A.3 and A.4. Symbols as in a).

the algebraic treatment (Equation A.4) of the ellipsometric measurements on the same sample yielded a value of 220 ± 25 cm^{-1}.[9] The slope of ω_{ps} vs. frequency should be flat in the absence of a frequency-dependent mass. We do see small slopes in Figures A.9a and A.9b, but since they occur with both positive and negative signs, we place little significance on them.

The predictions for the conductivity from an isotropic s-wave or d-wave gap parameter are qualitatively different. In Figure A.10a, we reproduce calculations by Carbotte and coworkers for a clean 50 K superconductor with both types of symmetry.[22] In the s-wave case, the conductivity drops much more rapidly towards zero with decreasing frequency. The absorptivity of the carriers with zero or near zero gap in the d-wave case is responsible a relatively larger absorptivity as $\omega \rightarrow 0$. The addition of impurity scattering increases the low frequency absorptivity for both cases, but the fundamental differences between the two types of symmetry seen in Figure A.10a remain. Carbotte and coworkers have argued that the in-plane conductivity in YBCO is more consistent with the d-wave prediction.[22]

Analysis of the $La_{2-x}Sr_xCuO_4$ conductivity is more difficult than YBCO because the dominant contribution to the conductivity between 150 and 300 cm^{-1} is from phonons. These must be removed from σ_1 to compare with predictions. Above 150 cm^{-1}, we expect neglible contribution to the conductivity from the normal Drude liquid or the superconducting London liquid, and so we have fit the complex dielectric function derived from data sets A and B between 150 and 280 cm^{-1} to a sum of three Lorentizian modes, each having contribution to the dielectric functions

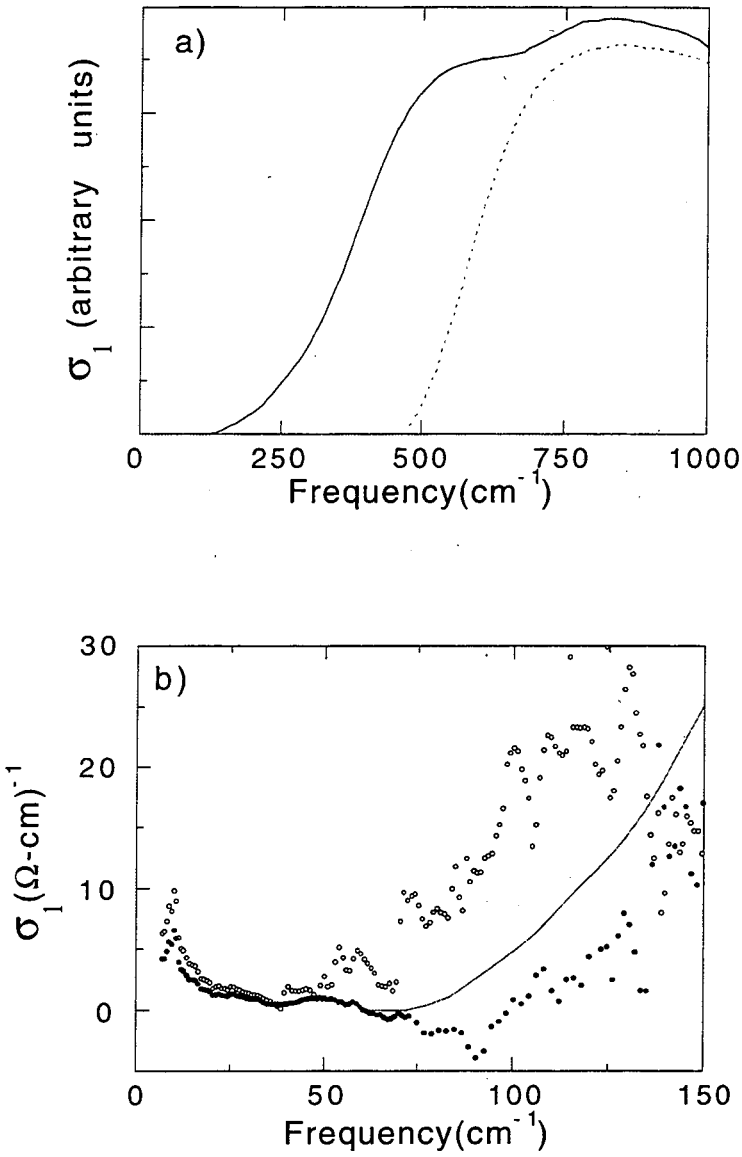

Figure A.10: a) Calculations from reference 22 of σ_1 for 50 K clean s-wave (dashed curve) and clean d-wave superconductor (solid curve.) b) σ_1 for data set A (open circles) and B (solid circles) after removal of Lorentizan contributions listed in Table A.1, and σ_1 calculated[22] for 31 K clean d-wave superconductor (solid curve) and scaled to compare with experimental data.

$$\tilde{\varepsilon}(\omega) = \frac{S_i\,\omega_i^2}{\omega_i^2 - \omega^2 - i\omega\gamma_i} \quad . \tag{A.5}$$

The obtained Drude-Lorentz fitting parameters are listed in the following table:

Data Set A	i	1	2	3
	$\omega_i(cm^{-1})$	193	233	251
	$\gamma_i(cm^{-1})$	80.9	25.9	15.1
	S_i	4.8	13.3	2.7
Data Set B	i	1	2	3
	$\omega_i(cm^{-1})$	197	225	242
	$\gamma_i(cm^{-1})$	65.6	29.4	12.7
	S_i	11.4	4.2	0.74

Table A.1 Drude-Lorentz Fitting Parameters.

The two higher frequency modes in data set A are phonons, and the deduced energies are consistent with those derived from the ellipsometric measurements.[9] We do not currently have a physical interpretation of the broad low frequency mode, which is required to account for the large conductivity below the lower energy phonon peak. The fits to data set B have much larger relative error and the energies obtained do not agree well with those for data set A. However, this is not surprising because the absorptivity measurement in this frequency range were made at much lower frequency resolution.

When we remove the contributions of the Lorentzians from $\sigma_1(\omega)$, we are left with the curves in Figure A.10b shown as open circles (data set A) and solid circles (data set B.) We have also included the prediction for a 31 K d-wave superconductor, which has been calculated[22] in arbitrary units and scaled for comparison to the data. The residual $\sigma_1(\omega)$ of our data is not consistent with predictions for an isotropic s-wave superconductor. It is not inconsistent with a d-wave prediction, but it is difficult to draw any definitive conclusions about the symmetry of the order parameter based on our results.

A.6 Summary

We have directly measured the absorptivity of a $La_{1.87}Sr_{0.13}CuO_4$ crystal between 6 and 520 cm^{-1}. These measurements complement ellipsometric reflectance data on the same sample for $\omega > 35$ cm^{-1}. We have used Kramers-Kronig analysis to extend measurements of the complex dielectric function $\tilde{\varepsilon}(\omega)$ or complex conductivity $\tilde{\sigma}(\omega)$ down to 6 cm^{-1}. Our main observations and conclusions are as follows:

1.) Below the plasma edge at 41 cm^{-1}, there is significant loss; the c-axis absorptivity varies from 0.2% at 6 cm^{-1} to 9% at 40 cm^{-1}. Between 12 and 35 cm^{-1}, $A(\omega)$ varies as ω^2, suggesting that a fraction of the carriers remain unpaired and can be described as a Drude liquid. The plasma edge occurs 1-2 cm^{-1} higher than seen in reflectance measurements made at 10 K on the same sample, indicating that more carriers participate in the superconducting condensate at 1.5 K than at 10 K.

2.) At 10, 26, and 33 cm^{-1} there are small peaks in the absorptivity. The interpretation of these peaks is not yet clear, but they may be related to

the intrinsic superconducting mechanism. Measurements on other samples with nominally identical stoichiometries will allow us to determine if the features are sample-dependent.

3.) The a-axis absorptivity below the plasma edge is nearly identical in magnitude and frequency dependence to the c-axis absorptivity.

4.) We have done Kramers-Kronig analysis of two data sets: one is comprised of absorptivity data below the plasma edge and reflectance data above, while the other consists predominantly of aborptivity data. From comparison of the two analyses we calculate the superconducting plasma frequency to be 235 ± 15 cm^{-1}.

References

1. K. Tamasaku, Y. Nakamura and S. Uchida, Phys. Rev. Lett. **69**, 1455 (1992).

2. D.G. Clarke, S.P. Strong and P.W. Anderson, Phys. Rev. Lett. **74**, 4499 (1995).

3. U. Walter, M.S. Sherwin, A. Stacy and P.L. Richards, Phys. Rev. B **35**, 5327 (1987).

4. P.E. Sulewski, A.J. Sievers, S.E. Russek, H.D. Hallen, D.K. Lathrop and R.A. Buhrman, Phys. Rev. B **35**, 5330 (1987).

5. Z. Schlesinger, R.L. Greene, J.G. Bednorz and K.A. Müller, Phys. Rev. B **35**, 5334 (1987).

6. D.A. Bonn, J.E. Greedan, C.V. Stager, T. Timusk, M.G. Doss, S.L. Herr, K. Kamarás, C.D. Porter, D.B. Tanner, J.M. Tarascon, W.R. McKinnon and L.H. Greeene, Phys. Rev. B **35**, 8843 (1987).

7. Z. Schlesinger, R.T. Collins, M.W. Shafer and E.M. Engler, Phys. Rev. B **36**, 5275 (1987).

8. J.H. Kim, H.S. Somal, M.T. Czyzyk, D. van der Marel, A. Wittlin, A.M. Gerrits, V.H.M. Duijn, N.T. Hien and A.A. Menovsky, Physica C **247**, 297 (1995).

9. R. Henn, J. Kircher, M. Cardona, A. Wittlin, V.H.M. Duijn and A.A. Menovsky, Phys. Rev. B. **53**, 9353 (1996).

10. W.H. Weber, C.R. Peters and E.M. Logothetis, J. Opt. Am. B **6**, 455 (1989).

11. E.E. Haller, N.P. Palaio, M. Rodder, W.L. Hansen and E. Kreysa, in Neutron Transmutation Doping of Semiconductor Materials, edited by R. D. Larrabee (Plenum, New York, 1984), p. 21.

12. D. Miller, P.L. Richards, S. Etemad, A. Inam, T. Venkatesan, B. Dutta and X.D. Wu, Phys. Rev. B **47**, 8076 (1993).

13. J. Bock, Thesis, U.C. Berkeley (1994).

14. E.I DuPont de Nemours & Co., Wilmington, Delaware.

15. W.A. Challener, P.L. Richards, S.C. Zilio and H.L. Garvin, Infrared Physics **20**, 215 (1980).

16. F. Gao, D.B. Romero, D.B. Tanner, J. Talvacchio and M.G. Forrester, Phys. Rev. B **47**, 1036 (1993).

17. M. Reedyk and T. Timusk, Phys. Rev. Lett. **69**, 2705 (1992).

18. I. Bozovic, Phys. Rev. B **42**, 1969 (1990).

19. D.N. Basov, H.A. Mook, B. Dabrowski and T. Timusk, Phys. Rev. B **52**, 13141 (1995).

20. D.J. Scalapino, Phys. Reports **250**, 331 (1995).

21. D. van der Marel, H.U. Habermeier, D. Heitmann, W. König and A. Wittlin, Phys. Rev. Lett. **176**, 1 (1991).

22. J.P. Carbotte, C. Jiang, D.N. Basov and T. Timusk, Phys. Rev. B **51**, 11798 (1995).

Ernest Orlando Lawrence Berkeley National Laboratory
One Cyclotron Road | Berkeley, California 94720

Prepared for the U.S. Department of Energy under Contract No. DE-AC03-76SF00098